Investigation of Mobile Phone SAR Reduction

Von der Fakultät für Ingenieurwissenschaften,
Abteilung Elektrotechnik und Informationstechnik
der Universität Duisburg-Essen

zur Erlangung des akademischen Grades

Doktor der Ingenieurwissenschaften (Dr.-Ing.)

genehmigte Dissertation

von

Manar Bakro
aus
Dair Atiyyah/Syrien

Gutachter: Prof. Dr.-Ing. Klaus Solbach
Gutachter: Prof. Dr.-Ing. Dirk Manteuffel
Tag der mündlichen Prüfung:
26.07.2016

Acknowledgements:

Firstly, I would like to express my gratefully and sincere gratitude to my advisor Prof. Dr.-Ing. Klaus Solbach for the continuous support of my Ph.D study and related research, for his patience, motivation, and immense knowledge. His guidance helped me in all the time of research and writing of this thesis.

I would like to thank my parents for supporting me, and finally my wife Lina for her support, encouragement, quiet patience and unwavering love were undeniably the bedrock upon which the past six years of my life have been built.

Table of Contents

Abstract

The increased amount of electromagnetic emission into the environment has increased the public concern over the possible health risks of wireless devices. However, to minimize the amount of energy absorbed by the user (measured by the Specific Absorption Rate, SAR) not only reduces any possible health hazards but is advantageous from the technical point of view, as well.

The purpose of this thesis is to investigate techniques for the reduction of the interaction between the mobile phone's antenna and the user's head by using different SAR control mechanisms while taking into account possible degradations of the electrical and mechanical antenna properties.

The thesis starts with fundamental theory of mobile terminal antennas and SAR and the numerical and measurement technologies are reviewed. The boundary conditions on electromagnetic fields are shown to effect EM wave propagation inside dielectric bodies, in particular, the permittivity of the material strongly affects the E&H field distributions. This is followed by an introduction of some of the recently suggested solutions for reduced SAR from internal handset antennas such as parasitic elements, directive control antenna, wave traps and slots in the PCB ground plane. These methods aim to control the current distribution and the direction of radiation in the near field, while ferrite, conductors and AMC shields are used to disperse or attenuate the EM fields radiated against the human body. As a superior solution, this thesis proposes a High-Impedance Surface Electromagnetic Band Gap (EBG) planar structure integrated below the antenna as SAR reduction solution.

With this method, for the case of a monopole antenna for GSM 1900 with backing by an EBG the SAR values inside a phantom are well reduced with only slight impact on the antenna radiation efficiency. On the other hand, the possible performance degradation of a Loop antenna for low-band (GSM 900) by the influence of the EBG (which is designed for GSM 1900) is checked and found to be acceptably small.

List of Abbreviations

AMC	Artificial Magnetic Conductor
CST	Computer Simulation Technology
DNG	Double NeGative
EM	Electromagnetic
EBG	Electromagnetic Band Gap
FDTD	Finite Difference Time Domain
FEM	Finite Element Method
FR4	Flame Retardant 4 (composed of fiberglass and an epoxy resin)
FSS	Frequency Selective Surface
GSM	Global System for Mobile Communication
HIS	High Impedance Surface
ICNIRP	International Commission on Non-Ionizing Radiation Protection
MRI	Magnetic Resonance Imaging
MEMS	Micro-Electro-Mechanical System
NRI	Negative Refractive Index
PEC	Perfect Electric Conductor
PIFA	Planar Inverted F Antenna
PMC	Perfect Magnetic Conductor
PBC	Periodic Boundary Condition
PBG	Photonic Band Gap
PDEBG	Polarization-Dependent Electromagnetic Band Gap
PCB	Printed Circuit Board
RF	Radio Frequency
SNR	Signal to Noise Ratio
SAR	Specific Absorption Rate
TE	Transverse Electric
TEM	Transverse ElectroMagnetic
TM	Transverse Magnetic
UMTS	Universal Mobile Telecommunications System

Chapter 1

1. Introduction and Overview

With the development of mobile communication and the popularization of mobile phones during the past ten years, since handsets have to meet tough technical requirements (Voice and Data), the transmitting power has increased. Therefore, the absorption of electromagnetic energy in the human head generated by the mobile phones has become an essential topic in the scientific research due to possible health risks. The Specific Absorption Rate (SAR) is a well-defined Figure of merit to evaluate the power absorbed by biological tissue, and the standards organizations have set exposure limits in terms of SAR.

Moreover, because of the bandwidth limitation of the Patch Inverted F Antenna (PIFA), the antenna types presently used mostly such as monopole and loop have been suggested as remedy for 4G handsets. However, most of monopole type radiation suffers from excessive SAR values; therefore, this radiator is placed near the bottom of the phone, which is naturally farther away from the head in talk position, but this tends to be not enough to satisfy SAR limits.

The purpose of this thesis is to investigate possible reduction of the interaction between the mobile phone's antenna and the user's head by using different SAR control mechanisms without redesigning the antenna. In addition, any solution must keep within the applicable terminal antenna design specifications. The specifications are concerned with electrical properties such as efficiency, bandwidth etc., and mechanical properties such as size, placement, mechanical shock impact etc. This thesis studies and analyses different published SAR reduction solutions, and proposes a High impedance surface-Electromagnetic Band Gap (EBG) structure as SAR reduction solution.

The EBG structure is proposed as RF shielding when it is inserted between the monopole antenna and the user's head at the frequency band GSM1900 which is most critical due to peak SAR values.

This thesis includes eight chapters. The concept of the mobile communication technique is introduced in the second chapter. This includes an overview about the interrelation between the most important antenna performance parameters such as the

reflection coefficient, bandwidth, and radiation efficiency. In addition, the fundamentals of the interaction between the user and the antenna are presented. The antenna and SAR measurement technologies are reviewed, which are later used in next chapters.

Chapter 3 reviews the interaction mechanisms between RF Fields and the Body, the radiation regions of an antenna are introduced to define the RF interaction region with the user's body. The effect of the boundary conditions on electromagnetic fields is presented and numerical results are generated to describe the EM fields distribution at the body boundary and inside the human's body. An overview of Antenna parameters in free space and in the vicinity of a user is presented to describe the RF antenna radiation losses inside the head.

These first three chapters provide the necessary background for the reader to be able to understand the concepts discussed in the later parts of this work.

In chapter 4, a quick view of different numerical simulation technologies (FDTD, MOM...) to simulate the 3D electromagnetic fields is presented; for the investigation in this thesis two commercial software packages: Computer Simulation Technology (CST) and High Frequency Structural Simulator (HFSS) are used.

In chapter 5, the near field distribution of the widely used monopole antenna close to a dielectric material interface at 900 GHz, and 1900 GHz are investigated. The relation between peak SAR location and surface currents distribution on the chassis is presented and compared between the two frequencies. In particular, the effect of the chassis size on the maximum SAR values and antenna efficiency is studied.

In chapter 6, state-of-the-art SAR control mechanisms, some recently published solutions for reducing SAR of internal antennas are investigated. The purpose of this investigation is to evaluate the possibility of using these solutions inside the mobile phone without negative impact on the mobile antenna performance at all frequency bands. In addition, numerical and experimental studies for some proposed solutions are presented. Including a simulation study on shield made of a Perfect Magnetic Conductor (PMC), which leads to the concept of a "metamaterial" used as a shield behind the antenna. This concept is investigated in detail using a specially designed multilayer offset stacked EBG structure in the next chapter.

In Chapter 7, interference and diffraction of EM waves on the EBG structure and peak SAR are investigated and compared for the case when no EBG is applied. The specific absorption rate values inside the phantom and antenna radiation efficiency are investigated for the case of a monopole antenna for GSM 1900 with and without backing by an EBG. Placement of the small EBG structure inside the phone is presented, moreover, SAR and antenna performance are investigated in free space and beside the user's head. Finally, the performance degradation of a Loop antenna for

low-band (GSM 900) is investigated to study the influence of the EBG (designed for GSM 1900), on the loop antenna operating at GSM 900.

In Chapter 8, the conclusions of this thesis are summarized and some suggestions for future work are presented.

Chapter 2

2. Mobile Communication Systems

In today's environment of almost constant connectivity, wireless devices are ubiquitous, as the Radio Frequency (RF) electronics technology for these wireless devices continues to decrease in size, there is a corresponding demand for a similar decrease in size for the antenna element. Unfortunately, the performance requirements for the antenna are rarely relaxed with the demand for smaller size. In fact, the performance requirements generally become more complex and more difficult to achieve as the wireless communications infrastructure evolves.

In the early organisation of cellular, Digital Cellular System (DCS), Personal Communications Service/System (PCS), and Global System for Mobile Communications (GSM) networks, the wireless device typically had to operate within a single band, defined by the specific carrier's license(s). In today's environment, the wireless device is often required to operate in more than one band that may include several GSM frequencies, 802.11 (Wi-Fi), 802.16 (Wi-Max) and Global Positioning System (GPS) as defined in Table 2-1. Note, frequencies below GSM 800 are not presented.

In today's wireless device terminology, an antenna that covers more than one of the wireless communications bands is considered as a multiband antenna. For example, an antenna that simultaneously covers two separate bands encompassing frequencies of 824–960 MHz and 1,710–1,990 MHz is considered as a four-band or quad-band antenna since it provides coverage of the GSM 800, GSM 900, GSM 1800, and GSM 1900 frequencies.

In addition, as known from the EM wave propagation theory, the power density (S) of waves is decreased when the distance (R) from the antenna is increased. Therefore, by decreasing the mobile phone thickness, the antenna comes closer and the effect of the antenna radiation on the user becomes higher.

Protocol	Uplink			Downlink			Name	Remarks
GSM850	824	836,5	849	869	881,5	894		
GSM900	880	897,5	915	925	942,5	960		
GSM1800	1710	1747,5	1785	1805	1842,5	1880		
GSM1900	1850	1880	1910	1930	1960	1990		
WCDMA I	1920	1950	1980	2110	2140	2170	UMTS 2100	IMT-2000 / UMTS Core band
WCDMA II	1850	1880	1910	1930	1960	1990		GSM1900 band; LTA
WCDMA III	1710	1747,5	1785	1805	1842,5	1880	UMTS 1800	GSM1800 band
WCDMA IV	1710	1732,5	1755	2110	2132,5	2155	UMTS 1700	Pairing with the core band
WCDMA V	824	836,5	849	869	881,5	894	UMTS 850	For the USA
WCDMA VI	830	835	840	875	880	885	UMTS 800	For Japan
WCDMA VII	2500	2535	2570	2620	2655	2690	UMTS 2600	IMT-2000 extension band
WCDMA VIII	880	897,5	915	925	942,5	960	UMTS 900	GSM900 band
WCDMA IX	1749,9	1767,4	1784,9	1844,9	1862,4	1879,9	UMTS 1700	Japanese version of UMTS1700
WCDMA X	1710	1740	1770	2110	2140	2170	Extended UMTS 1700	

Table 2-1: Uplink and downlink frequency bands for various cellular networks (Frequencies in MHz). [1]

Although the most common fear in people's minds is the concern with the potential risk of getting a brain cancer or other serious disease, investigations on mobile terminals in the vicinity of a user are important also from the technical point of view. The reduction of power absorbed by the user not only reduces any potential health hazards but also makes the antennas more efficient. Arising from these aspects, antenna designers have been forced to pay a growing amount of interest on reducing the radiation absorbed by the user.

Fully understanding the process of how and why the fields generated by a mobile terminal antenna are absorbed by the user would enable the antennas to be designed from the very beginning so that the energy absorbed by the user could be minimized. The antenna size, bandwidth, radiation efficiency and SAR (Specific Absorption Rate) are interrelated in a complex manner, such that a design of a mobile terminal antenna that operates as desired in all possible environments is a great challenge. [2]

In this chapter, the interrelations between the most important performance parameters of a mobile terminal antenna are discussed by introducing the concepts of impedance bandwidth, radiation efficiency and quality factor. In addition, the fundamentals of the interaction between the user and the antenna are presented.

As shown in Figure 2-1 there are different antenna types commonly used as transmitting antenna such as Monopole antenna and IFA (Inverted F Antenna), PIFA (Planar Inverted F Antenna), Loop Antenna.

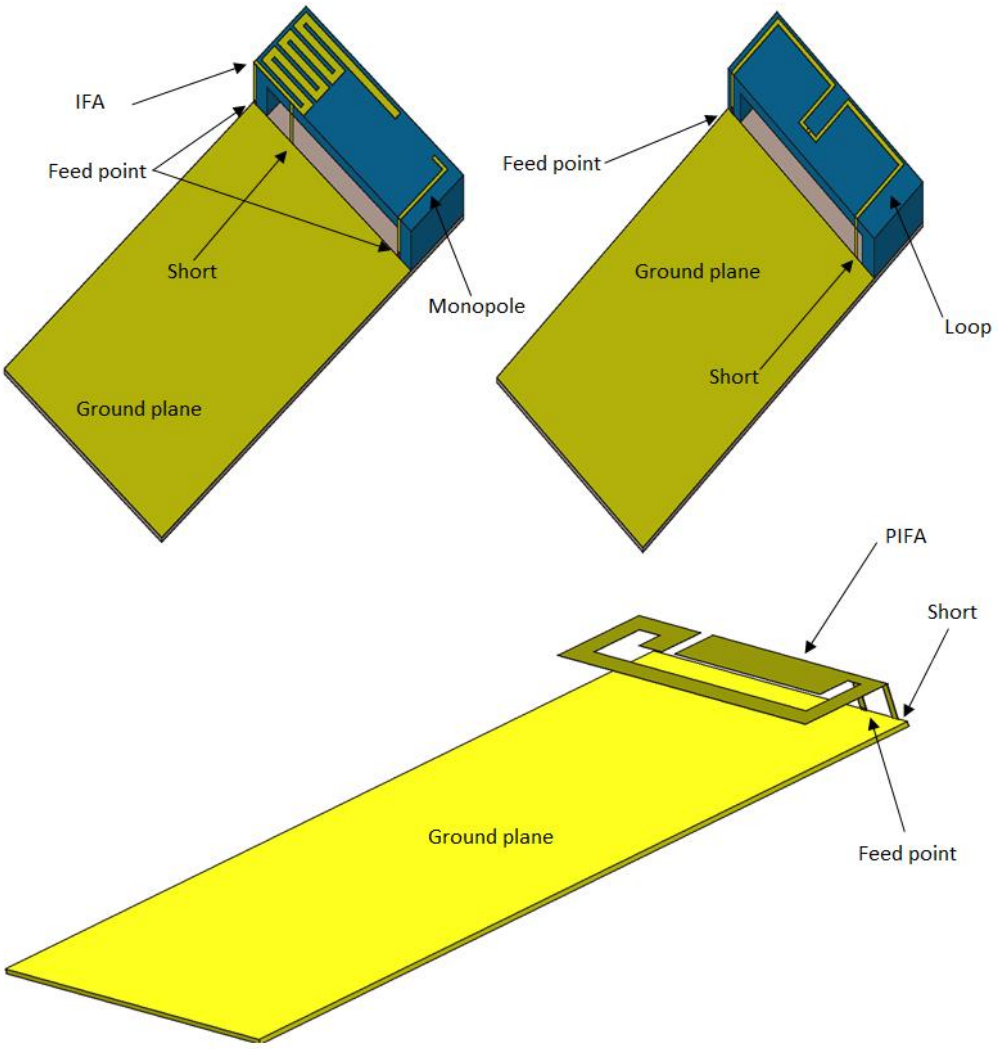

Figure 2-1: Mobile phone antenna types

2.1. Reflection coefficient:

A part of the incident wave reflects back from the antenna, when the antenna impedance $\underline{Z}_a$ differs from the characteristic impedance Z_o of the transmission line. The reflection coefficient caused by the antenna is given by

$$\underline{\rho} = \frac{\underline{Z}_a - Z_o}{\underline{Z}_a + Z_o} \tag{2.1}$$

Where $\underline{\rho}$ is often described as the scattering parameter $\underline{S}_{11}$.

The impedance of an antenna consists of resistive R_a and reactive components X_a according to Equation (2.2)

$$\underline{Z}_{\mathrm{a}} = R_{\mathrm{a}} + jX_{\mathrm{a}} \tag{2.2}$$

The equivalent circuit model for the impedance parameters of an antenna and transmission line are presented in Figure 2.2.

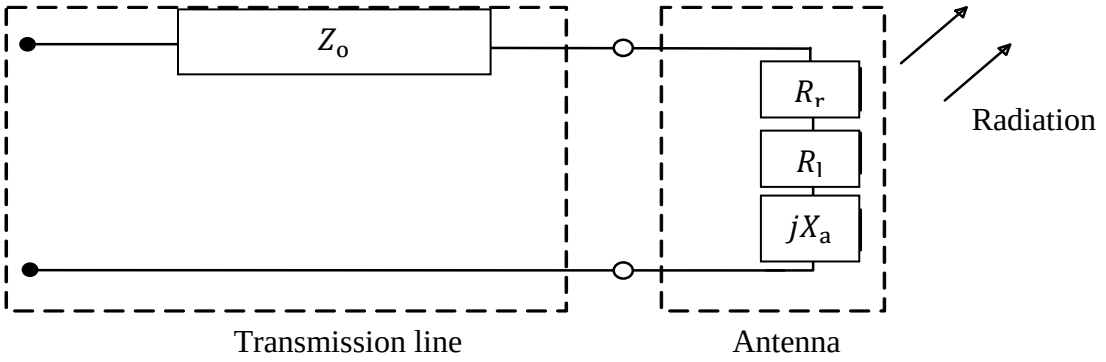

Figure 2-2 : Equivalent circuit of the transmitting antenna

The resistive part of the impedance further consists of radiation and dissipation losses,$R_{\mathrm{a}} = R_{\mathrm{r}} + R_{\mathrm{l}}$, and the reactive part X_{a} is caused by energy stored in the antenna's reactive near fields. However, at the antenna's resonant frequency, the reactive part of the impedance disappears.

A very close object affects the antenna impedance. However, in many cases a slight mismatch is accepted. E.g., for small handset antennas $|\underline{\rho}| = |\underline{S}_{11}| \leq 0.5$ is often considered adequate for the operating frequency range.

2.2. Bandwidth:

When designing small mobile terminal antennas, the absolute bandwidth BW_{abs} mostly refers to the impedance bandwidth, i.e. the frequency range where condition $|\underline{\rho}| = |\underline{S}_{11}| \leq$-6 dB is satisfied. The corresponding values for Voltage Standing Wave Ratio $VSWR \leq 3$, and return loss $R_{\mathrm{L}} \geq 6$ dB can be calculated from Equations:

$$VSWR = \frac{1+|\underline{\rho}|}{1-|\underline{\rho}|} \tag{2.3}$$

$$R_{\mathrm{L}} = 10log\frac{1}{|\rho|^2} \tag{2.4}$$

Bandwidth can also be represented relative to the center frequency f_c leading to the relative bandwidth, which is defined in the following equation:

$$B_r = \frac{BW_{abs}}{f_c} \tag{2.5}$$

BW_{abs} : Absolute impedance bandwidth, f_c : Center frequency

Table 2.2 presents bandwidth requirements for different wireless systems that can be applied in portable devices.

System	f_c [MHz]	BW_{abs}[MHz]	B_r [%]
GSM 850	859	70	8.1
GSM 900	920	80	8.7
GSM 1800	1795	170	9.5
GSM 1900	1920	140	7.3
WLAN (802.11g)	2450	100	4.1
WLAN (802.11a)	5250	200	3.8

Table 2-2: Frequency bands of different systems.

2.3. Efficiency

The radiation efficiency $\eta_{rad}$of an antenna is defined as the ratio of the radiated power P_{rad} to the power P_{in} accepted by the antenna:

$$\eta_{rad} = \frac{P_{rad}}{P_{in}} \tag{2.6}$$

By using the impedance parameter of an antenna, the radiation efficiency can be written as:

$$\eta_{rad} = \frac{R_r}{R_r + R_l} \tag{2.7}$$

Because the radiation efficiency does not take into account the losses due to mismatch between the antenna input and the transmission line, the total efficiency of an antenna is defined as the ratio of the radiated power to the incident power P_{inc} to the antenna, and it can be calculated from:

$$\eta_{tot} = \eta_{rad}\eta_m \tag{2.8}$$

Where η_m=1-$|\rho|^2$ represents the matching efficiency.

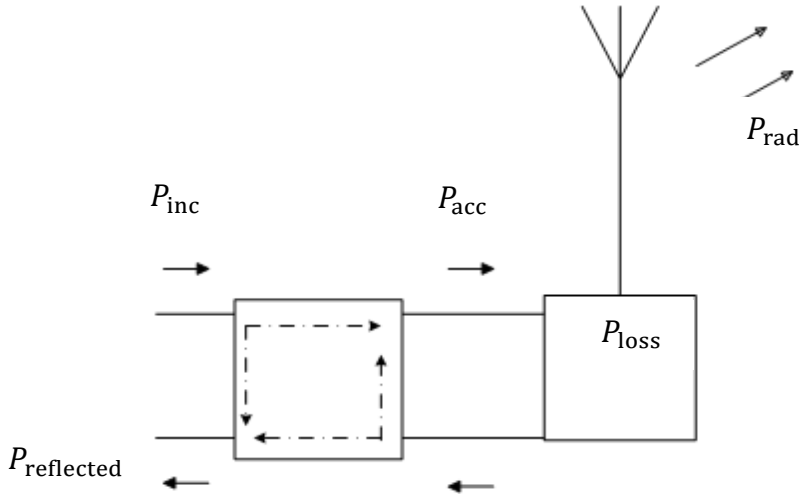

Figure 2-3 : Power distribution in the antenna system

Figure 2-3 shows the relation between the powers in the antenna system which can be written as the following:

$$P_{inc} = P_{reflected} + P_{loss} + P_{rad} \tag{2.9}$$

$$P_{acc} = P_{loss} + P_{rad} \tag{2.10}$$

Part of the accepted power is dissipated by conductors and dielectrics losses, which is symbolised as P_{loss}.

2.4. Antenna efficiency measurement

The measurement of the mobile terminal antenna performance is an important step in antenna design. The antenna performance of a mobile antenna is generally evaluated by measuring its radiation pattern in an anechoic chamber. This has traditionally been achieved by a passive measurement method that feeds the antenna from an external signal source via a coaxial cable. However, due to the fact that a feeder cable need to be drawn to the mobile antenna, spurious emission caused by leaked current on this feeder cable can significantly degrade measurement accuracy. To overcome this problem the active measurement method has been used in recent years, which measures the antenna radiation pattern with high accuracy by using the terminal's own RF transceiver

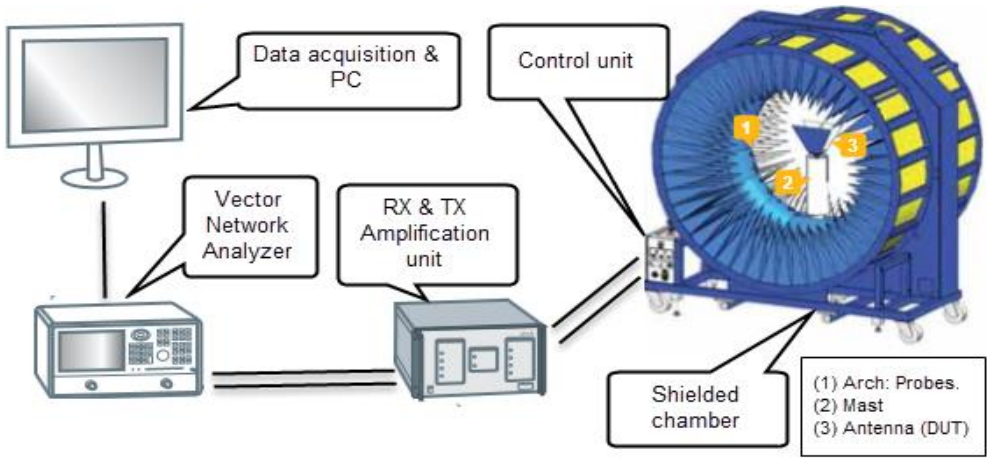

Figure 2-4: Overview of SATIMO passive antenna measurement system. After [3]

The Figure 2-4 shows the antenna measurement system from SATIMO, which was used in this thesis as passive measurement instrumentation for antenna efficiency. The Vector Network Analyzer VNA is used as RF source/receiver and the control unit drives the two positioning motors and the electronic scanning of the 15 two-polarization probes, with space 22.5° between two probes and rotation step of the mast of 11.25°.

The active measurement was used to analyse the radiation pattern shape and the efficiency; this method generally is referred to as OTA, where OTA measurements determine the **O**ver-**T**he-**A**ir performance of mobile terminals such as mobile phones. The resulting values for **T**otal **R**adiated **P**ower (TRP) are a figure of merit for qualifying a mobile terminal performance in a network as shown in Figure 2-5.

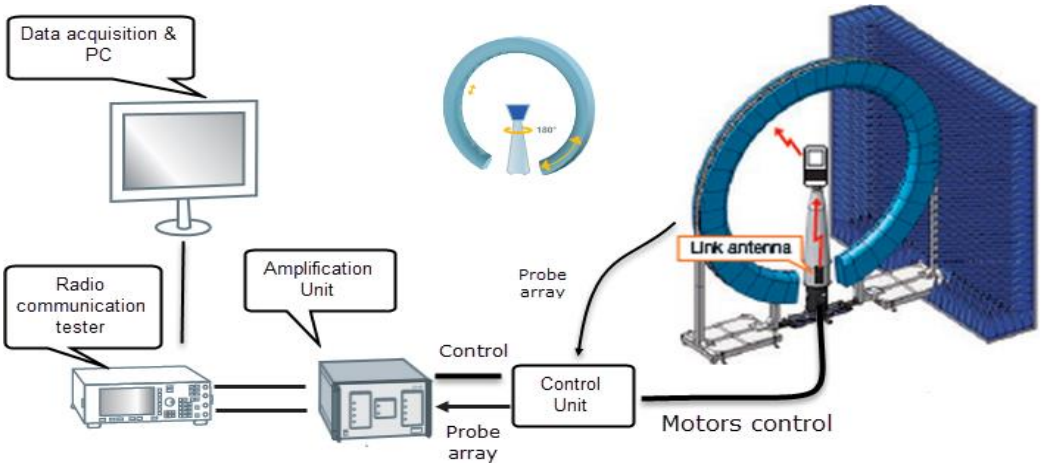

Figure 2-5: Overview of active measurement system (TRP), consisting of 64 two-polarization probes with 0.02° Azimuth accuracy.After [4]

In TRP measurement, the total RF channel power radiated by the mobile phone is calculated by integrating the measured Effective Isotropic Radiated Power (EIRP) data over the measurement sphere. The amplification unit amplifies the signal on reception channels according to the frequency bands; the Radio Communication Tester (CMU) controls the transmit power of the mobile terminal by the link antenna.

TRP measurement is on the complete system, combining the antenna performance and the RF transceiver performance and is defined in the following equation:

$$TRP = \frac{1}{4\pi} \oint \left(P_{\mathrm{tx}} G_{\theta}(\Omega; f) + P_{\mathrm{tx}} G_{\phi}(\Omega; f) \right) d\Omega \tag{2.11}$$

Here, G_{θ} and G_{ϕ} denote the vertical and horizontal polarization components, respectively, of the antenna gain pattern at frequency f and Ω denotes the area of a spherical surface cut away by a cone whose vertex is the center of the sphere. In addition, P_{tx} is the transmitted power of the DUT so that $P_{\mathrm{tx}}G_{\theta}$ and $P_{\mathrm{tx}}G_{\phi}$ denote the effective radiated power known as Equivalent Isotropically Radiated Power (EIRP).

2.5. User interaction

The everyday use of devices emitting radio frequency (RF) is rapidly increasing. Close to the antennas, the electric field strengths can reach several hundred volts per meter. Even higher values can be found close to occupational sources used for processing of various materials by heating and sometimes by formation of plasma discharge in the material. Power sources generating high levels of electromagnetic fields are typically found in medical applications and at certain workplaces. Medical devices used for magnetic resonance imaging (MRI), diathermy, various kinds of RF ablation, surgery, and diagnoses may cause high levels of electromagnetic fields at the patient's position or locally inside the patient's body. The cellular mobile communication causes on average low levels of electromagnetic fields in areas accessible to the public by comparison to the medical devices. However, it might cause significantly higher peak levels of exposure during use of mobile terminals.

2.5.1. Absorption of radiation into the user

During the last decade, the issue of electromagnetic interaction between human tissue and a mobile phone has been intensively studied to expand the understanding of radiation safety of mobile communication systems. In the case of a mobile phone, a

considerable part of the power radiated from the antenna is actually absorbed into the user's head, hand and the rest of the body.

The biological effects of electromagnetic radiation on living cells can be classified into two types: ionizing effect and non-ionizing effect, based on the radiation's capability of ionizing atoms and breaking chemical bonds.

According to present knowledge, the only influence that electromagnetic radiation has on human tissue is the rise in temperature (non-ionizing effect), Figure 2-6, when the source frequency is between 100 kHz to 300GHz [5]. If the temperature rise on the surface of the brain caused by radio waves is not more than 0.3 degrees, it is known that this does not have any physiological significance. As a comparison, the normal fluctuation is around ±1°C, and in exhausting physical exercise, even a temperature rise of two degrees is quite common [6].

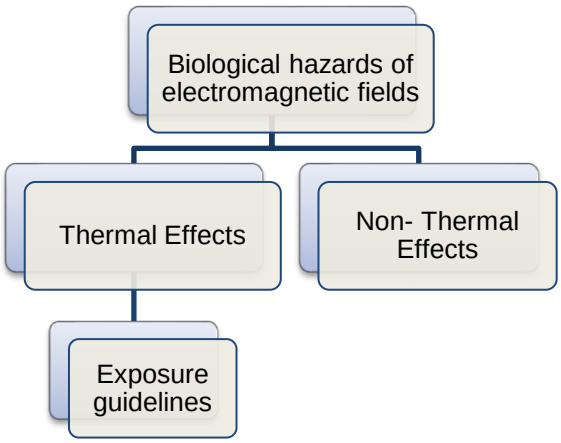

Figure 2-6 : Biological hazards of electromagnetic fields

Although the increase in tissue temperature is too small to cause any biological damage, it has been speculated that electric fields may, by some unknown non-thermal mechanism, disturb normal cell function. Hence, in addition to tissue heating, other possible health hazards of mobile phone radiation have been intensively studied in the last 20 years.

Apparently, the most popular subject of research has been to study the potential connection between mobile phone radiation and brain cancer. On the basis of research results obtained from these studies, it hasn't been possible to conclude that radiation from mobile phones would be detrimental to health [6].

Target	Effect	Threshold
Whole	Various physiological effects	1.0 °C
Eye	Cataract	3 – 5 °C
Skin	Warmth sensation	0.02 – 1 °C
	Pain sensation/Burns	10 – 20 °C
Brain	Neuron damage	4.5 °C

Table 2-3: Thresholds for the induction of thermal effects to the human body (world health organization WHO)

The electromagnetic fields as regards absorption of energy by the human body can be divided into four ranges: [7]

- Frequencies from 100 KHz to less than 20 MHz, at which absorption in the trunk decreases rapidly with decreasing frequency and significant absorption may occur in the neck and legs.
- Frequencies in the range from 20 MHz to 300 MHz, at which relatively high absorption can occur in the whole body, and even to higher values if partial body (e.g., head) resonances are considered.
- Frequencies in the range from 300 MHz to several GHz, at which significant local, non-uniform absorption occurs.
- Frequencies above 10 GHz, at which energy absorption occurs primarily at the body surface.

The main dosimetric parameter for evaluating the absorption of electromagnetic radiation to human is the Specific Absorption Rate SAR. SAR is a measure to quantify the electromagnetic energy absorbed by unit mass of tissue and is defined as:

$$SAR = \sigma_{\text{eff}} \frac{E^2}{\rho} \tag{2.12}$$

Where σ_{eff} is the effective conductivity of the tissue (Siemens per meter), E the root-mean-square value of the induced electric field strength (V/m), and ρ is the tissue density. The unit of SAR is watts per kilogram (W/kg) or milliwatts per gram (mW/g) and it denotes the time rate of non-ionizing radiation energy absorption at a given location inside the tissue.

In practice, SAR is always determined as an average value over a finite, most often 1g or 10g, tissue mass.

2.5.2. SAR-Limits

The RF energy in the frequency range of Global System for Mobile Communications (GSM): 824 MHz to 2170 MHz, and WLAN: 2.45 GHz and 5.2 GHz is called non-ionizing because the photon energy is insufficient to knock electrons from atoms in living tissue.

The most apparent biological effects of RF energy at cell phone frequencies are due to heating, which means increase in the temperature of the tissues.

Table 2.4 presents the recommended limits for local maximum SAR values in an uncontrolled environment set by IEEE (Institute of Electrical and Electronics Engineers) and ICNIRP (International Commission on Non-Ionizing Radiation Protection). In Europe the ICNIRP recommendations are the most widely followed, while the slightly stricter standards set by IEEE are applied in the United States.

The SAR limits are defined at different time duration over 6 minutes (ICNIRP 1998) and over 30 minutes (IEEE 2005).

		Workers Controlled	General public Uncontrolled
ICNIRP	Whole-body SAR	4 W/kg	0.08 W/kg
	Local SAR(10 g averaging)	10 W/kg	2 W/kg
IEEE	Whole-body SAR	4 W/kg	0.08 W/kg
	Local SAR(1 g averaging)	8 W/kg	1.6 W/kg

Table 2-4: Recommended maximum local SAR values set by ICNIRP and IEEE.

The recommendations presented in Table 2.4 give information for antenna designers. That is, the radiation safety of mobile communication devices can be designed in and tested by using these levels as references.

The fundamentals of the interaction mechanisms between electromagnetic fields and dielectric material, such as human tissue, are further discussed in the subsequent chapters of this thesis.

2.5.3. Reduction of radiation efficiency

Radiation efficiency is defined as the ratio of the total power radiated by an antenna to the net power accepted by the antenna from the connected transmitter.

When the antenna is placed beside the head, the accepted antenna power P_{acc} consists of the antenna dissipation P_{loss} , the absorbed power in the head P_{h} and (far-field) radiated power P_{r}.This can be expressed as:

$$P_{\mathrm{acc}} - P_{\mathrm{loss}} = \frac{1}{2}\, Re(VI^{*}) = P_{\mathrm{h}} + P_{\mathrm{r}} = \frac{1}{2}\int_{V_b} \sigma_1\, |\bar{E}|^2\, \partial V + \frac{1}{2} Re\left[\int_s\ (\bar{E} \times \bar{H}^{*}) \partial S\right] \tag{2.13}$$

V_{b}: Volume of body, S: Far-field sphere.

Besides the health issues, it is essential from the antenna efficiency point of view to minimize the power absorbed in the user's head and the rest of the body; the smaller the portion of power that human tissues absorbes, the larger is the share that radiates into the surrounding free space.

In fact, the portion of power absorbed in the user largely determines the total radiation efficiency of the system including the phone and the user. Especially at GSM bands, the contribution of power that is absorbed in the user is commonly very large and with internal mobile phone antennas, even more than 90 % of the total accepted power can be lost due to the presence of the user.

There is no doubt that the input power is also partly lost in the mobile phone antenna and the structure such as in the battery, display and all the plastic components. However, free space radiation efficiency of a commercial mobile phone can be still in the order of 80 % (corresponding to approximately 1 dB of loss in the structure) or more.

2.6. SAR Measurement Equipment (Near-Field Scanners)

In order to evaluate the SAR and induced current density inside of the human body exposed to electromagnetic fields, various measurement methods have been developed (IEEE C95.3-2002). For the measurements, human body phantoms are frequently used while in other cases, volunteers or cadavers have been used [8]; [9]. In order to keep

the repeatability of the measurement high, human-body phantoms with homogeneous liquid dielectric properties are preferable.

For local SAR measurement, there are two methods, one is E-field measurement and another is temperature measurement. E-field measurement is used for compliance tests of mobile phones because the sensitivity is relatively high and 3-D measurement is available if a liquid-type phantom is used.

The procedures of the compliance tests of wireless terminals such as mobile phones based on E-field measurement have been standardized internationally between 300 MHz and 3 GHz (IEC 62209-1-2005; IEEE Std. 1528-2003). It is also noted that E-field probes must be calibrated at each frequency and in phantom materials with the electrical properties adjusted to those of the biological tissues at the frequency of interest. Thus, an E-field probe which is only calibrated in free space cannot be used to measure E-field strength in phantoms.

2.6.1. 3-D Scanning System:

Figure 2-7 shows a typical 3-D SAR measurement system used to perform SAR measurement in the head and body phantom. The system measures the E field's amplitude inside the liquid. The probe is held by the robot arm and scans the entire exposed volume of the phantom in order to evaluate the three-dimensional field distribution.

Figure 2-7: Mobile phone SAR measurement system which consists of an E-field probe positioned by a robot in a head phantom exposed to a mobile phone at the right ear. From [10]

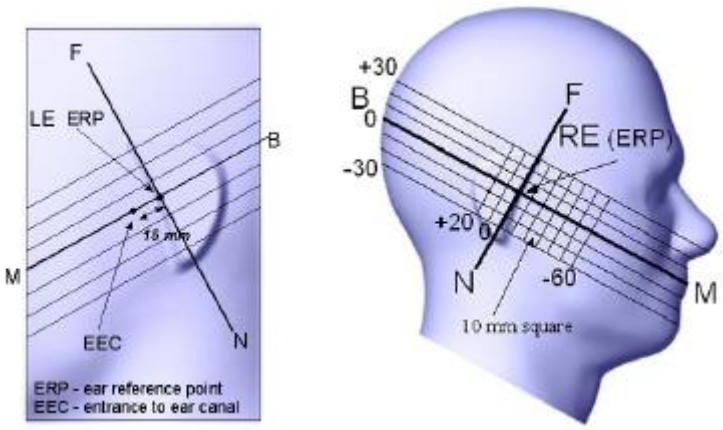

Figure 2-8 : Side view of the phantom head showing the ear and marking lines BM and NF. Intersection RE is the ear reference point (ERP). From [11]

Figure 2-8 shows the side view of the phantom. The center-of-mouth reference point is labelled "M," the left ear reference point (ERP) is marked by "LE," and the right ERP is marked by "RE." Each ERP is located on the B-M (back-mouth) line 15 mm behind the entrance-to-ear-canal (EEC) point. At the test frequency the robot measures the E field over the Scan Area (81x141x1 mm^3), with measurement grid d_x=10mm, d_y=10mm.

There are two mobile phone positions for every head side, cheek touch and 15°tilt. In this study, the cheek touch (right head) position is used to compare the SAR values from different antenna measurements. The phantom is filled with tissue equivalent liquid for various frequencies based on a plane wave analysis [12].

In the near field of a wireless handset, the EM field distributions may have sharp spatial variations in both magnitude and polarization. Thus, the typical field probe for measuring SAR shall be much smaller than the wavelength λ in a tissue equivalent liquid, be isotropic, and shall be transparent to the measured field.

The Figure 2-9 shows a typical E-field probe, which consist of three mutually orthogonal center-fed short dipole antennas. [13]

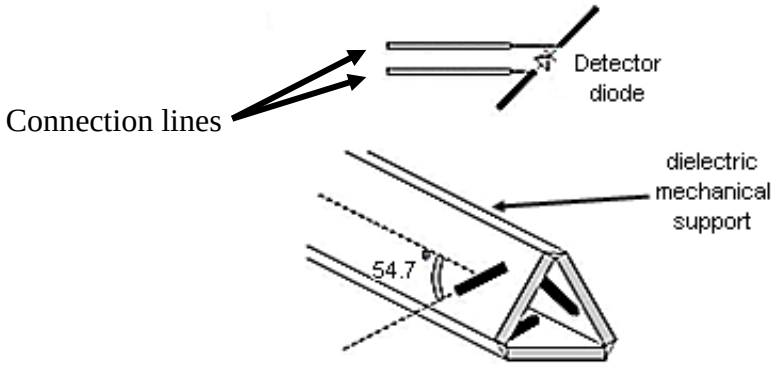

Figure 2-9: Typical E-field probe construction: Dielectric structure supports the three miniature and mutually orthogonal sensor dipoles. After [13]

Every dipole antenna (sensor) has a detector diode at the feed point, which produces a rectified voltage proportional to the square of the E-field component, and high resistance connection lines. The total E-field vector magnitude is calculated as in the following equation:

$$|E| = \sqrt{|E_1|^2 + |E_2|^2 + |E_3|^2} \tag{2.14}$$

E_1, E_2, E_3: The three orthogonal components measured by the sensors, and SAR calculated per 1g or 10g cubic by the equation (2.12).

2.6.2. 2-D Flat Scanner (iSAR):

The scanner is based on a sensor array implanted in a solid flat phantom. The phantom is filled with a broadband tissue simulating gel (useful 500 MHz to 3 GHz), with 256 sensors located at 4mm below the surface, Figure 2-10.

The density of the sensor array (grid of 15mm) is sufficient to reliably assess the exposure. The measured SAR values of all sensors are acquired and integrated in parallel; the total assessment time is less than 1second. [14]

Figure 2-10: Mobile phone 2-D SAR measurement system which consists of an array of E-field probes located 4mm below the surface. After [14]

The 2-D scanner has been used to support quick evaluations of SAR values, and this scanner can measure the two electric field polarizations (X, Y) parallel to the phantom surface. The absence of the polarization in the depth direction may cause SAR underestimation if the source has strong electric fields perpendicular to the phantom surface and the source is located in close proximity to the iSAR surface. Using low-loss spacers between the device and the iSAR can reduce this effect. [15].

Generally, both 2-D and 3-D scanners are connected to the PC, and the local SAR values for 1g, 10g are calculated from the measured E-field and presented on the PC by using special software and solving the SAR equation (2.12).

Chapter 3

3. Interaction between Handset Antenna and User

3.1. Introduction

A human is the user of the mobile communication system, and the effect of the user needs to be considered in order to design antennas with proper performance and acceptable SAR value. The user of a mobile phone can actually be considered as a part of the radiating system, as the nearby human tissue affects the electromagnetic fields generated by the device.

When radio waves propagate in a dielectric material, such as human tissue, electric and magnetic fields are generated inside the material. The frictional forces between the particles that start to move due to the electric field cause losses, which results in absorption of energy. It is well known how these fields inside a dielectric material interact with the material, but the connection between the original external fields and the generated internal fields is still an object of research.

Since the total efficiency of a system including the antenna and the user is strongly affected by the power absorbed by the user, SAR requirements, i.e., the topic of energy absorbing mechanisms in human body tissue is important not just because of the SAR limits but also from the antenna efficiency point of view. Therefore, for an antenna designer, it would be extremely useful to know and understand these mechanisms and thus to be able to predict the trends of bandwidth, efficiency and SAR.

In this chapter, the interaction between the fields generated by the antenna and the nearby dielectric tissue of a user is investigated. At first, the radiation regions of the antenna and the boundary conditions in Electro-Magnetic (EM) theory need to be reviewed for the understanding of the interaction between the user and the mobile phone.

3.2. Radiation regions of an antenna

The ultimate goal, or the mission, of an antenna is to create an electromagnetic field into the surrounding space. The properties of this particular field are, by their very nature, dependent on the distance from the antenna. The field that is generated by the antenna can be roughly divided into three regions [16]: Reactive near field, radiating near field, and far field. Figure 3-1 shows the radiation regions of an antenna.

Closest to the antenna we find the so called reactive near field, where the energy storing reactive fields, represented by the reactive part of the antenna input impedance, dominate over the radiating fields: The energy is actually just bumping back and forth, instead of radiating away.

The role of the radiating fields becomes more dominant when the observation point is moving away from the antenna. The distance, where the reactive and radiating energies become equally strong, determines the border of reactive and radiating near fields. For an antenna, whose maximum extent is *D*, the radiating near field region begins at distance r_1 from the antenna, and r_1 is approximated by:

$$r_1 = 0.62\sqrt{\frac{D^3}{\lambda}} \tag{3.1}$$

where λ is the wavelength in free space. The radiating near field region is historically called the Fresnel region. In the Fresnel region, the field pattern is still dependent on the distance from the antenna. For comparison, as the limiting case of infinitely small extent, the near field distance for an infinitely small current element (Hertzian dipole) can be calculated as $\frac{\lambda}{2\pi}$.

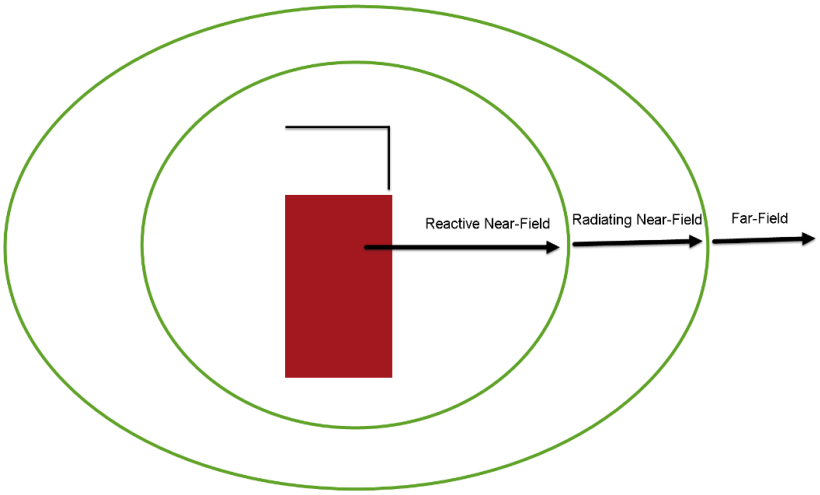

Figure 3-1: Antenna regions: reactive near field, radiating near field, and far field.

The region where the field pattern is only angle-dependent and no more distance-dependent is called the far field region, or more elegantly, the Fraunhofer region. The far field region can be considered to begin at distance r_2, which is approximated by:

$$r_2 = \frac{2D^2}{\lambda} \tag{3.2}$$

For an antenna and PCB (chassis) combination of a mobile handset, the exact distances to near and far field from the antenna structure can be difficult to define. Although the largest dimension of the antenna element itself is in the order of 40 mm at frequencies not substantially higher than 1 GHz, the PCB, whose length is about 100 mm, acts as the main radiator [17], and thus dominates the dimension *D* in equations (3.1) and (3.2).

3.3. Boundary conditions at the material interfaces

In absence of surface charges ρ_s and surface current density J_s on the interface, the tangential components of the electric and magnetic field strength are continuous at the interface. Furthermore, the normal components of the electric and magnetic flux density are continuous. In the more general case, including charges and surface current densities, for human tissue-material properties we can summarize:

Maxwell boundary conditions: (3.3)

$$E_{1t} - E_{2t} = 0$$

$$D_{1n} - D_{2n} = \begin{cases} 0 & Without\ surface\ charge\ density \\ \rho_s & With\ charge\ density\ on\ interface \end{cases}$$

$$D_{1n} = \varepsilon_1 E_{1n}$$

$$D_{2n} = \varepsilon_2 E_{2n}$$

$$H_{1t} - H_{2t} = \begin{cases} 0 & Without\ surface\ current\ density \\ J_s & With\ surface\ current\ density\ on\ interface \end{cases}$$

$$B_{1n} - B_{2n} = 0$$

Figure 3-2 shows the tangential and normal E-field components at both sides of a boundary between dielectric material with ε_1 on one side and ε_2 at the other side.

As the permittivity of the material in region 2 increases, the directions of the electric fields in region 2 are forced to turn more parallel to the interface. This can be

explained by Maxwell's boundary conditions for electric field components parallel and normal to the surface, which require that.

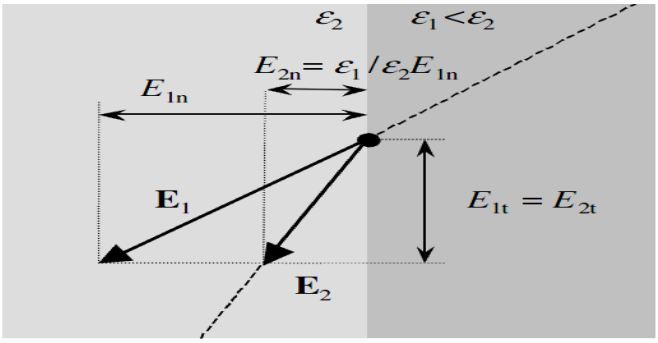

Figure 3-2 : Boundary condition for electrical field

The electric field component in region 2 normal to the interface is reduced at the boundary. The study on the interaction between the fields of an antenna near dielectric material is started by exploring the electric and magnetic fields when a large volume filled with material of different dielectric parameters (dielectric block) is placed beside the antenna.

Figure 3-3 shows two monopole antennas one for 900 MHz, one for 1900 MHz mounted on an antenna carrier (ground plane) and located above the dielectric block in 19mm distance.

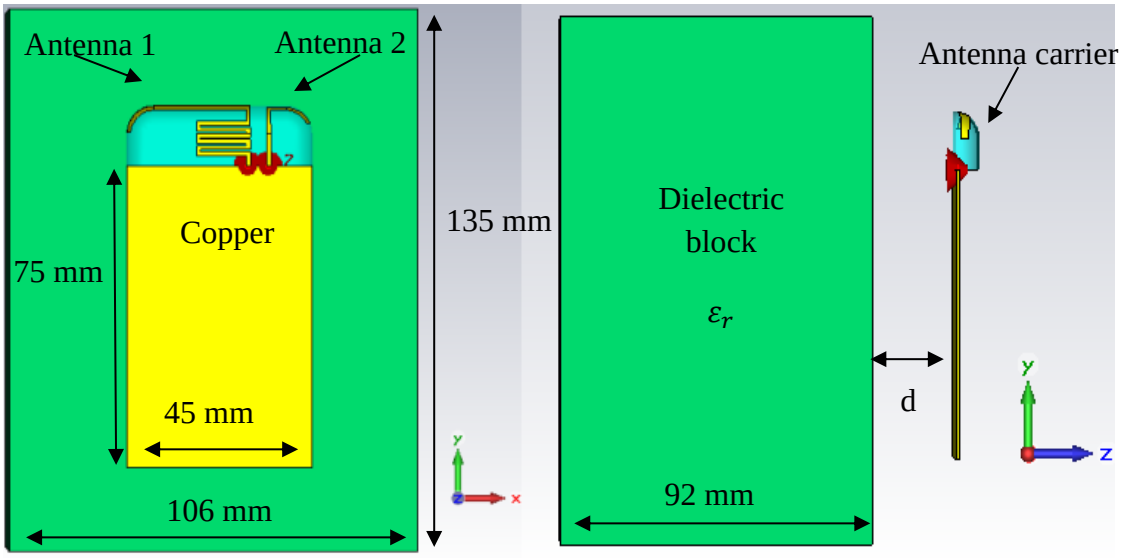

Figure 3-3: Geometry of the simulation model, Antenna 1 for 900 MHz, and Antenna 2 for 1900 MHz.

The simulation shows the distributions of electric and magnetic fields when the distance between the dielectric block and the ground plane of the antenna is fixed, and four different values of permittivity (ε_r= 1,5,20 and 42) are used, Figure 3-4 and Figure 3-5 .

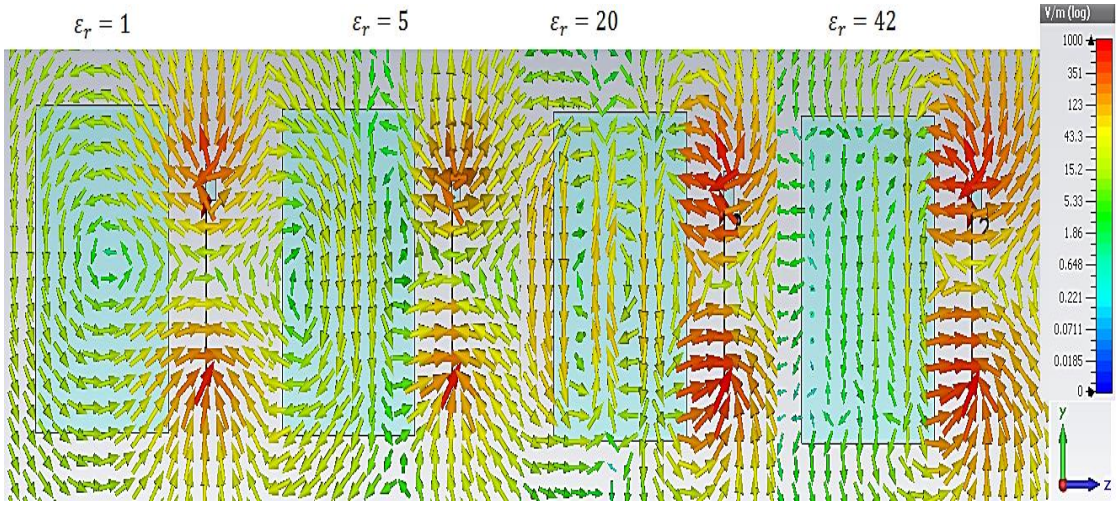

(a)

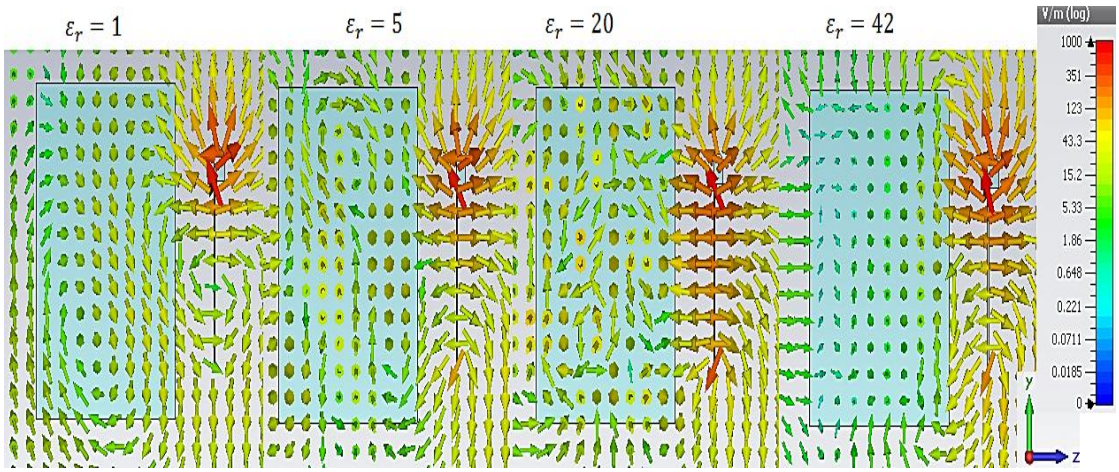

(b)

Figure 3-4: E-field distributions at (a) 900 MHz,(b) 1900 MHz in YZ-plane. Permittivity ε_r is 1,5,20 and 42 and effective conductivity σ_{eff}=0.

Figure 3-4 shows: As the permittivity of the dielectric block increases, the directions of the electric fields inside the block are forced to turn more and more parallel to the surface of the dielectric block, and the electric field component perpendicular to the surface(E_Z) of the block is more and more attenuated at the boundary. The Z-

component of the electric field hardly penetrates through the material when the permittivity of the material is high, although it is very strong between the antenna and the dielectric. The H-field distributions inside the dielectric block and at the boundary are shown in Figure 3-5.There, we see how the antenna excites a standing wave pattern inside the dielectric body, more clearly the higher the permittivity is.

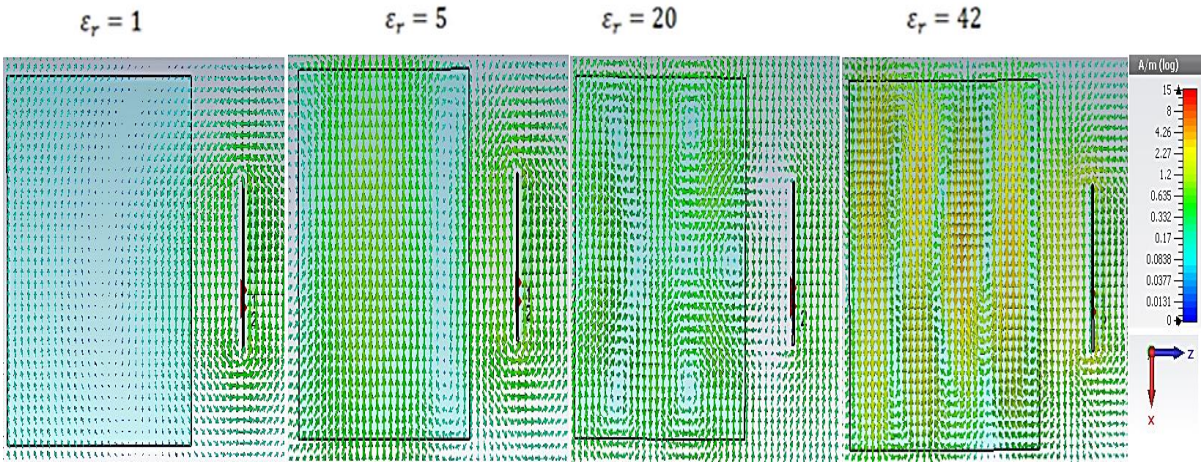

(a)

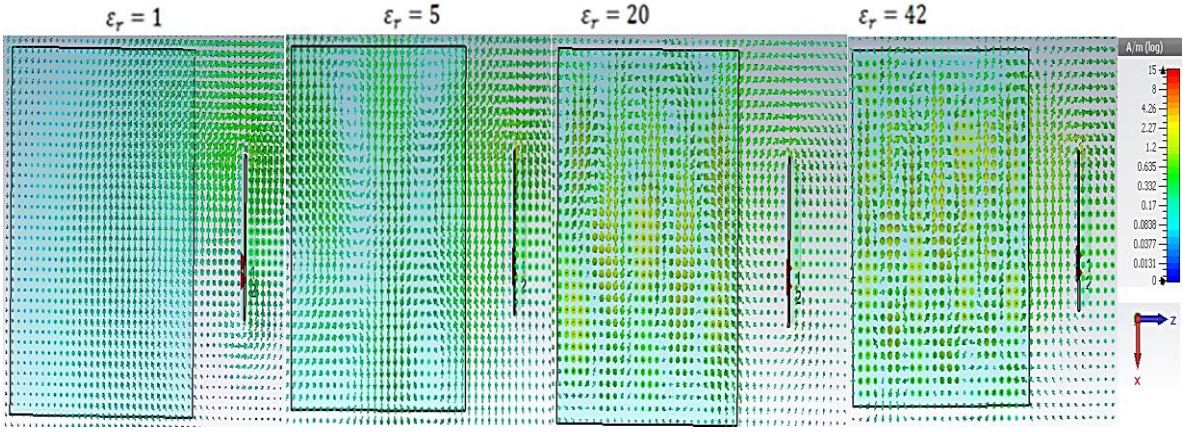

(b)

Figure 3-5 : H-field distributions at (a) 900 MHz,(b) 1900 MHz in XZ-plane. Permittivity ε_r is 1,5,20 and 42. Effective conductivity σ_{eff}=0.

Figures 3-4, 3-5 show that as the permittivity of the dielectric block increases, distributions of the magnitudes of electric and magnetic fields inside the block become more and more alike.

Furthermore, the magnitude of the magnetic field inside the dielectric block seems to increase significantly as the permittivity of the block increases. The analysis shows that electric and magnetic fields have strong values in the areas along the Y-axis close to locations where the currents on the surface of the ground plane of the antenna are high, as well.

3.4. Absorption mechanisms for mobile phones with integrated antennas:

When the free space radio frequency electromagnetic field impinges on a biological body, it is reflected, transmitted, refracted or scattered by the biological body. The reflected and scattered fields may proceed in directions different from that of the incident RF field.

The transmitted and refracted fields from the RF exposure induce electric and magnetic fields in the biological systems, which interact with cells and tissues in a variety of ways, depending on the frequency, waveform, and strength of the induced fields and the energy deposited or absorbed in the biological systems.

At the lower mobile communications frequency of 900 MHz, the wavelength in air is 33.3 cm, and for the reactive and radiation fields of a Hertzian dipole to have equal amplitudes the distance of $\lambda/2\pi$ is about 5.3 cm. At 1900 MHz, the wavelength in air is 15.78 cm and the $\lambda/2\pi$ distance is 2.5cm. Clearly, at the mobile phone frequency bands both near-zone reactive and radiative wave interactions are encountered in the vicinity of personal wireless telecommunication systems.

If the induced E-field is known, quantities such as current density (J) and specific energy absorption rate (SAR) are related to it by simple conversion formulas. In this case, for an induced electric field E in ($\mathrm{Vm^{-1}}$), the induced current density is given by:

$$J(x,y,z) = \sigma(x,y,z)E(x,y,z)\,, \tag{3.4}$$

where σ is the electrical conductivity ($\mathrm{Sm^{-1}}$) of the biological tissue and SAR is given as

$$SAR(x,y,z) = \frac{\sigma(x,y,z)|E(x,y,z)|^2_{rms}}{\rho(x,y,z)} \qquad \left[\frac{W}{kg}\right] \tag{3.5}$$

Where ρ is the mass density of the tissue ($\mathrm{kg\ m^{-3}}$).

The section 2.5 gave an overview about absorption of radiation into the user, and in this section, the mechanisms of interaction and the dielectric properties of the human body tissues are presented.

3.4.1. Biophysical mechanisms of interaction

The electromagnetic energy is known as being carried by photons or quanta, and the energy of the photon is given by:

$$E = hf \tag{3.6}$$

Where h is the Planck's constant = 4.1356×10^{-15} eVs, *f*: frequency of the waves in Hz. The higher the frequency, the higher the energy per photon, and a definite amount of photon energy is required to produce ionization by ejection of orbital electrons from atoms of the material through which an electromagnetic wave propagates. The minimum photon energies capable of producing ionization in water and in atomic carbon, hydrogen, nitrogen, and oxygen are between 12.4 and 25 eV. Inasmuch as these atoms constitute the basic elements of living organisms, 12.4 eV may be considered as the lower limit for ionization in biological systems, giving a frequency limit of 3 PHz. Figure 3-6 shows the electromagnetic spectrum, the non-ionizing frequency (DC to 3×10^{15} Hz), and the Ionizing frequency above 3×10^{15} Hz .

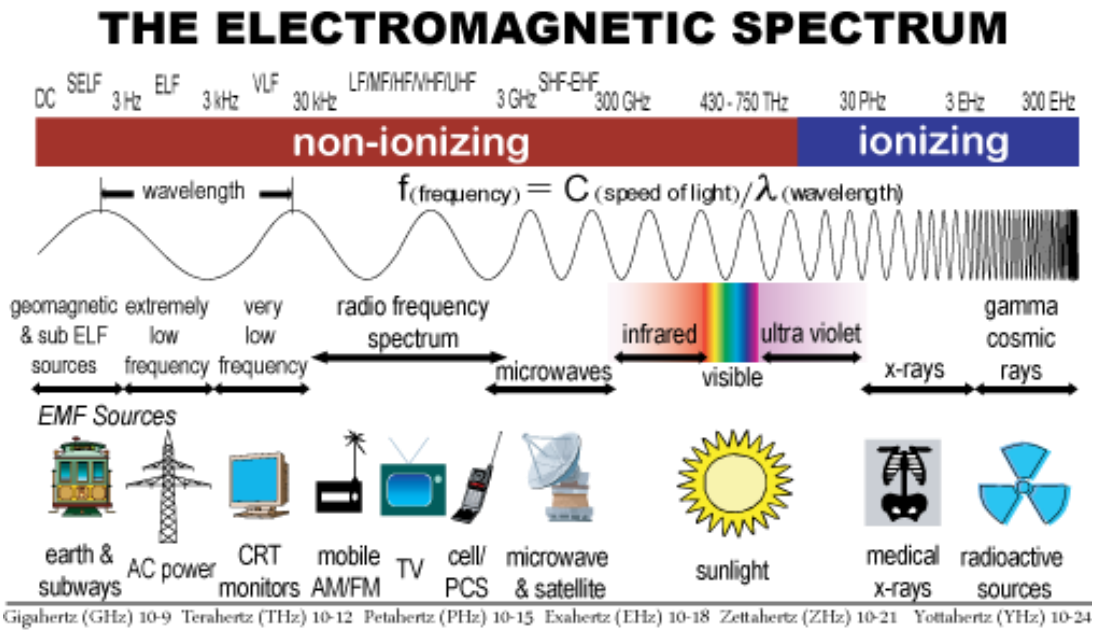

Figure 3-6: The electromagnetic spectrum and non-ionizing and ionizing bands; from [18].

A single photon of radio frequency RF and microwave MW radiation 300 Hz to 300 GHz has relatively low energy levels, less than 1.24 meV; therefore, it is not capable of ionization. Accordingly, electromagnetic radiation in the RF&MW spectrums is regarded as nonionizing radiation. That means, the tissue heating is the dominant interaction mechanism of microwave radiation with biological systems.

3.4.2. Dielectric properties of human body tissues

When an electromagnetic wave propagates in a material whose electrical conductivity σ differs from zero, as is the case in all human tissues, dissipation losses are caused due to the current density generated according to Ohm's law:

$$\vec{J} = \sigma\vec{E} \tag{3.7}$$

Part of the power in the electromagnetic field thus turns into heat. The dielectric properties of human tissue, i.e., permittivity and conductivity, are considered to decrease with age due to the changes of water content and organic composition of tissues.

The dielectric properties of a material characterized by its complex permittivity are defined in the following way:

$$\varepsilon = \varepsilon_{\mathrm{o}}\varepsilon_{\mathrm{r}} = \varepsilon_{\mathrm{o}}(\varepsilon_{\mathrm{r}}' - j\varepsilon_{\mathrm{r}}'') \tag{3.8}$$

$$\varepsilon_{\mathrm{r}} = \varepsilon_{\mathrm{r}}' - j(\sigma_{\mathrm{eff}}/\omega\varepsilon_o) = \varepsilon_{\mathrm{r}}'\left(1 - j\frac{\varepsilon_{\mathrm{r}}''}{\varepsilon_{\mathrm{r}}'}\right) = \varepsilon_{\mathrm{r}}'(1 - jtan\delta) \tag{3.9}$$

where ε_{o} is the free space permittivity (8.854 $\times 10^{-12}$F/m), ε' the real part of complex permittivity, ε'' the imaginary part of complex permittivity and $\omega = 2\pi f$ the angular frequency, and tan δ is the loss tangent. The imaginary part of the relative permittivity ε_{r}:

$$Im\{\varepsilon_{\mathrm{r}}\} = \sigma_{\mathrm{eff}}/\omega\varepsilon_o \tag{3.10}$$

Can be considered to represent all losses in the material. Here, all the losses, including(ionic) conductivity losses and dielectric losses are described by the effective conductivity σ_{eff}. Because all human tissues are non-magnetic materials, no losses due to permeability μ occur.

To be able to model the behaviour of radio wave propagation inside dielectric material, accurate knowledge of the values of dielectric parameters of the material is required. In case of a human, tissues inside the body can be roughly divided into two

categories. Tissues that have high water content, like muscle or skin, have high values of real part of permittivity ε_r' and losses described by the effective conductivity σ_{eff} are high, as well. On the other hand, in materials that have low water content ε_r' is low and σ_{eff} is low. Examples of such materials are bone and fat. The frequency dependence of dielectric parameters of human tissues was studied in [19]. A model for determining the tissue parameters over the frequency range of 10 Hz - 100 GHz is presented in that paper.

In Table 3-1, values of ε_r' and σ_{eff} for head tissue equivalent material relevant in the studies that consider interaction between mobile terminal antennas and users are presented for the frequency range 750 MHz – 2.3 GHz. Values given in the table are based on the parametric model described in [11], [19]and will be used in simulations and measurements later in the thesis.

Frequency (MHz)	**Relative permittivity (ε_r')**	**Effective conductivity (σ_{eff}) (S/m)**
750	41.9	0.89
835	41.5	0.90
900	41.5	0.97
1450	40.5	1.2
1500	40.4	1.23
1640	40.2	1.31
1750	40.1	1.37
1800/1900/2000	40.0	1.40
2100	39.8	1.49
2300	39.5	1.67

Table 3-1 : Dielectric properties of head tissue-equivalent material in the 750 MHz to 2300 MHz frequency range.

3.5. SAR Generation

Even if radio wave propagation in a lossy material can be described precisely by application of Maxwell's theory, the connection between the field inside a dielectric tissue and the original external electromagnetic field generated by a mobile terminal antenna is not fully explained. The related studies have mostly focused on determining the SAR characteristics related to concrete certain arrangements, while the general energy absorption mechanism has been left with less consideration. In addition, results of studies concerning the issue are quite diverging [20], [21] , [22].

The general energy absorption mechanism in the close near field of dipole antennas above 300 MHz was studied in [21]. The goal of that study was to find a relation between the free space field strengths of the antenna and the corresponding *SAR* values. The starting point was to examine the behaviour of magnetic fields, since electric field lines are distorted in the vicinity of dielectric material, while the current distribution and its related magnetic field around the antenna was considered to be less affected.

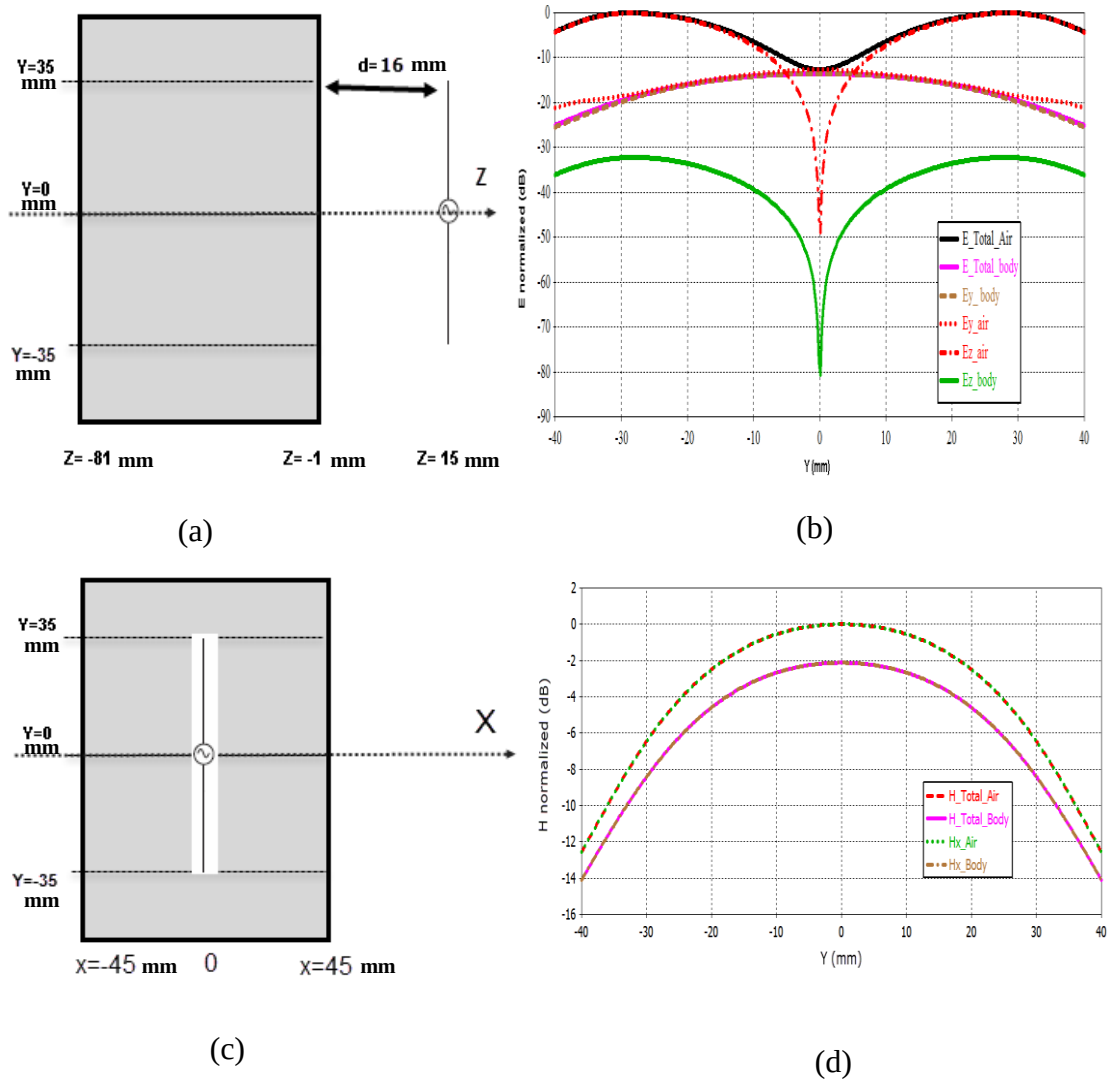

Figure 3-7 : (a) Geometry of the simulation model Side view, (c) Top view. (b) ,(d) Normalized electric and magnetic field components in air (Z=0) and in the body model (Z=-5 mm) at X=0. σ_{eff} =1.4 S/m, $\varepsilon_r' = 40$.

Research results in that paper suggested that the main absorption mechanism could be described by surface currents induced by the magnetic fields. SAR values were found to be mainly proportional to the square of the incident magnetic field strength, which

led to the conclusion that the spatial peak SAR is related to the antenna spatial peak current. Consequently, it was concluded that coupling of electric fields would be of minor importance.

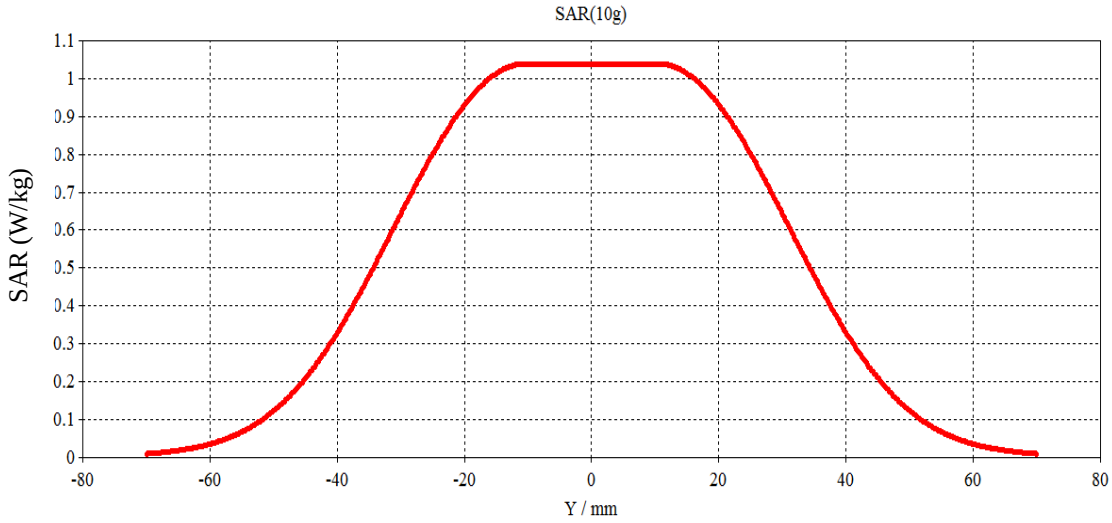

Figure 3-8: SAR distribution at X=0, Z=-5mm. $P_{\mathrm{acc}} = 0.1$Watt, frequency 1.9 GHz.

In order to gain more insight, a similar simulation configuration was studied:

As SAR measurement standards use the phantom filled with tissue equivalent liquid and without any fat layer, Figure 3-7 shows our simulation model with a half-wave length dipole antenna operating at 1.9 GHz beside a human body phantom. The maximum electric and magnetic fields inside the phantom are located on the plane Y=0. The total magnetic field is equal the tangential component H_{X} and slightly decreases below the tissue surface due to current density since $\sigma_{\mathrm{eff}} \neq 0$. The normal E-field component E_{Z} which is maximum at the two ends of the dipole is significantly attenuated at the boundary surface, and the tangential E-field component E_{Y} which is maximum at the middle of the dipole penetrates the boundary surface without any attenuation. Figure 3-8, shows the SAR (10g) distribution at 4mm below the phantom surface (Z=-5mm). The peak SAR is located close to the peak current on the dipole and the maxima total E-&H-fields, which is the location of the feed point of the dipole antenna. Due to the maximum current amplitude the excited H_{X} and E_{Y} components have maximum amplitude in the air and they propagate into the body without attenuation at the tissue surface.

From this and from results found in section 3.3, observations can be divided into two basic cases: For tissues whose ε_{r} is high as in Figure 3-7, such as muscle, inside the tissue the electric field component perpendicular to the tissue surface is significantly

attenuated at the tissue surface, and thus the SAR maxima are found in locations where the total electric field in air is moderate, but the component parallel to the surface is significant.

For low-permittivity tissues, like fat, the SAR maxima were found in [21] close to locations where the perpendicular electric field was strong also in free space, because in this case the attenuation of the normal component is small as has be seen before in section 3.3 for $\varepsilon_r' = 5$.

From these results, we can conclude that in mobile phones the highest SAR areas (known as hot spots) coincide with high surface current regions on the chassis, which are excited by the antenna and which generate high tangential electric and magnetic field at the head-to-air interface. This will be investigated further in chapter 5.

3.6. Antenna parameters in the vicinity of a user

The deterioration of the performance of the mobile terminal antenna located close to the human body is due to the fact that the human tissue consists of a lossy dielectric material [23]. From the graphs presented in Figure 3-4, 3-5, it can be concluded that in mobile communications the user is commonly situated in the reactive near field of the antenna, meaning that the parameters of the antenna are very likely disturbed.

In most cases these disturbances are case specific, and an exact prediction of the problem is difficult. Nevertheless, some theoretical background of how the dielectric loading would affect the antenna operation can be found.

The effect of the user can be presented as an extension circuit to the standard equivalent circuit model of an antenna. In the extended model Figure 3-9, dissipation losses caused by the user are presented as the conductance G_{user}, while the parallel capacitance C_{user}, symbolizes the reactive effects of the user; C_{user} can cause a shift in the resonant frequency of the antenna structure. A quick look at the definition of the resonant frequency of a resonator, known as $f_r = 1/2\pi\sqrt{LC}$ -leads to the trivial conclusion that the resonant frequency is lowered by the additional, user-originated, parallel capacitance C_{user} .

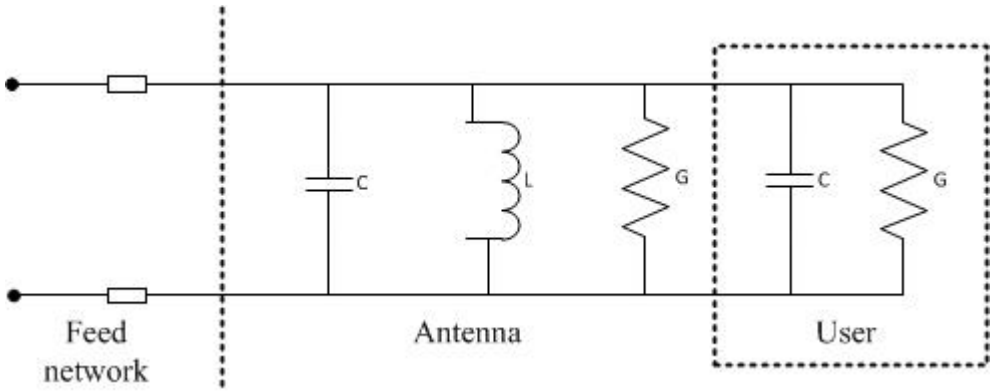

Figure 3-9: Equivalent circuit model of an antenna, including the effect of the user.

Chapter 4

4. EM Simulation Technology (Numerical Techniques)

The current evolution of wireless personal communications has necessitated a comprehensive understanding of electromagnetic (EM) interactions between handset antennas and the human body.

These human-antenna interactions influence the electromagnetic performance of the antenna by altering antenna input impedance, and modifying the antenna radiation patterns and polarization state, absorbing antenna-delivered power, and so on.

Also questions concerning health hazards have necessitated a more thorough evaluation and characterization of the specific absorption rate (SAR) in the human tissue. Recently, significant progress in understanding human–antenna interactions has been achieved due to advanced computational techniques as well as accurate near field measurements.

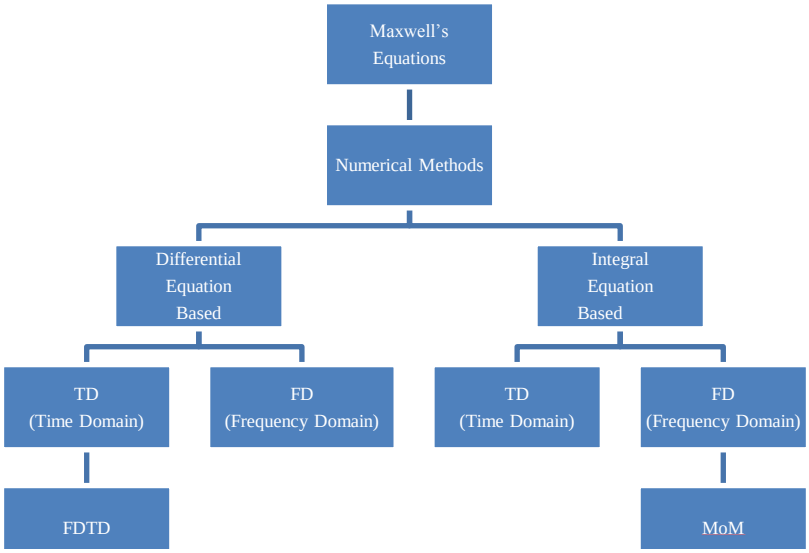

Figure 4-1: Common numerical techniques

Common numerical techniques, Figure 4-1, currently used for electromagnetic interaction computations are finite difference time domain (FDTD) method, the method of moments (MoM), the finite element method (FEM), and in addition, software codes that use hybrid methods, software that applies more than one

numerical method. All these techniques are using numerical approximations of Maxwell's equation to calculate the electromagnetic fields.

In the Finite Difference Time Domain Method FDTD the discretization grid is rectangular in general and the Maxwell equations are discretized by simple finite difference equations [24]. The solution is created via a time step-by-step propagation on the discretized grid. In most implementations there are two separate grids, one for the unknown electric field E and one for the unknown magnetic field H components. The two grids are displaced by a half-cell, such that the nodes of the ones are in the centers of the other cells. The software "CST Microwave Studio" from CST AG, which is used in this thesis, uses this method to simulate the antenna inside the mobile phone.

The Method of Moments MOM is a numerical computational method of solving linear partial differential equations which have been formulated as integral equations (IE) and Green's functions and it is sometimes called the Boundary Elements Method (BEM). MOM is used in frequency domain and has the advantage of applying easily to long thin wires or thin patches, and layered configurations such as EBG; these situations can present serious challenges to the finite difference methods since they have to discretize the entire domain where the presence of thin structures requires a very fine mesh. The software "High Frequency Structure Simulator (HFSS)" from Ansys in this study uses an MOM solver and this was used for simulations of antenna backed by EBG in free space and beside the head.

The Finite Element Method FEM is used to find approximate solution of partial differential equations (PDE) and integral equations. FEM is based on frequency domain and each solving of the matrix system gives the solution for one frequency [25]. Repeated runs and interpolation are used to obtain the systems response over a frequency band. This might give problems for resonant systems, especially those with high Q, where it is not easy to get the resonant frequency unless you sweep the frequency carefully. One solver using FEM is called Eigen Mode in CST software, which was used for EBG reflection phase tuning.

In the SAR simulation, the average SAR (10g) calculation employs two methods, IEEE C95.3 and CST legacy. For each point a cube with a defined 10 g mass is found and the power loss density is integrated over this cube, Figure 4-2.

In the standard IEEE C95.3 [26], if one face of the averaging cube is outside the tissue the cube is invalid and an inner point with maximum SAR value is copied. Therefore, a flat curve is seen at the phantom boundary and this method comes closer to the measurement setup. In the standard CST legacy (CST C95.3) the averaging cube at the boundary is increased until the biological mass reaches 10 g. In this standard, a slowly rising curve at the boundary is seen and takes for invalid averaging volumes

not the maximum but the closest valid SAR. The SAR distribution shape is different in Figure 4.2, but the maximum averaged SAR value stays equal in both procedures.

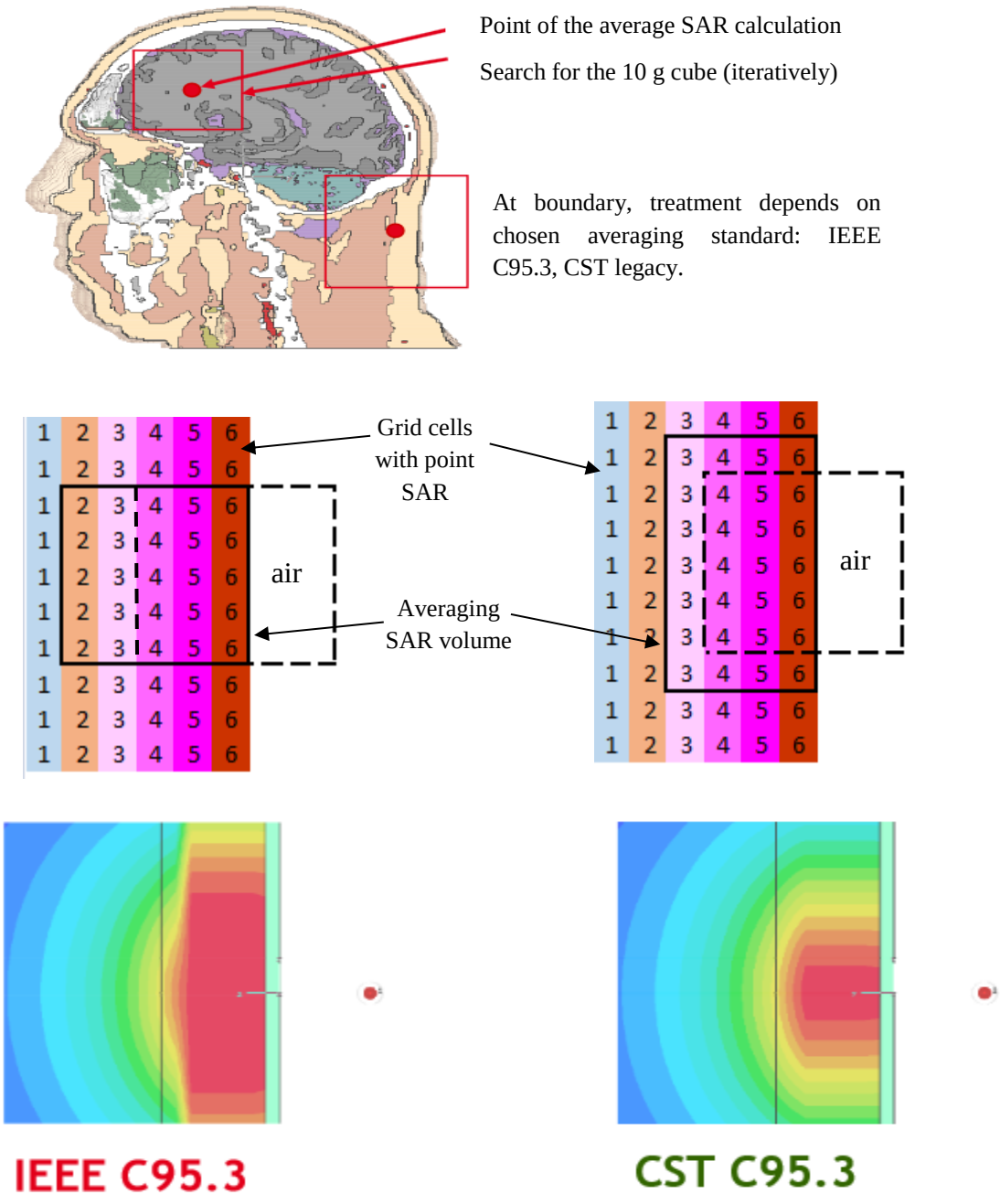

Figure 4-2: SAR Averaging procedure [CST Microwave Studio].

EM simulation, fields and SAR calculations in this thesis have used these three methods.

Chapter 5

5. Analysis of near-field distribution

5.1. Introduction

A review of studies [20] [21] [22] concerning the general mechanisms of interaction between antenna and user may lead to better understanding. However, results from these studies do not provide us with fully reliable clarification about the issue. Especially conclusions made concerning the general energy absorption mechanism in human tissue have been quite deviating. The study [20] concluded that the peak SAR is not related to antenna currents, the locations of peak SAR were clarified by exploring the real part of tissue permittivity and its effect on the electric field components perpendicular and parallel to the surface of the tissue.

The study in [21] is discussed in chapter 3 and it is suggested that the main absorption mechanism is current induction on the surface of human tissue by incident magnetic fields. SAR values proportional to the square of the incident magnetic field strength lead to the conclusion that the spatial peak SAR is related to spatial radiator currents. In [22], the EM energy deposition into the body with and without a fat layer at 915 MHz are presented and compared. A hot spot is observed on the muscle surface near the antenna feed point location for the pure muscle body and as shown also in chapter 3, two hot spots on the fat surface near the ends of the antenna are observed. Due to low permittivity of the fat $\varepsilon_r = 5.5$ the vertical E-field at the end of the dipole penetrates the boundary surface with slight dissipation loss.

In addition to the incomplete understanding of the general energy absorption mechanism in human tissue, studies that are related to user interaction have most commonly been case-specific, focusing simply on determining certain parameters related to a specific problem.

However, many things were still left in the previous studies without a suitable explanation. The main reason for the difficulties in explaining every phenomenon was considered to be the excessive complexity of the used simulation models, which

included two different antenna models, two different phantoms as the head or body model. Also, the wide frequency range in question made things more complicated. The studies that are reported in this chapter are motivated by the lack of full understanding of the mechanisms of how antennas actually interact with the user. The main goal is to improve the understanding of the near field interaction with the user.

This chapter is structured in the following way. First, in Section 5.2, the used antenna model is introduced, and properties of this particular antenna in free space are discussed to provide us with a sufficient background and points of comparison with the user interaction studies reported in the later parts of the thesis. In Section 5.3, the effects of dielectric material on the field distributions of the antenna are studied by a very simple model; field distributions inside and nearby a dielectric half space situated beside the antenna are studied as a function of different parameters. All the presented results in this chapter are based on simulations that have been carried out with commercial FDTD-based software CST-Microwave Studio.

5.2. Antenna model for the simulations

The versatility and on the other hand the simplicity of the structure provided motivation for selecting a monopole antenna structure on a mobile terminal in the user interaction studies of this thesis.

In addition, the highest SAR values in modern handsets usually come from the monopole antenna. As Figure 5-1 shows, two monopole antennas are used for both the low and high frequency bands (900MHz,1900MHz), both placed on the top position of the PCB ground plane , whose dimensions are 60 mm wide,1 mm thick and having the popular length of 95 mm. Grilamid LV-5H (ε_r=3, tanδ=0.02) standard plastic mobile antenna carrier supports the antennas.

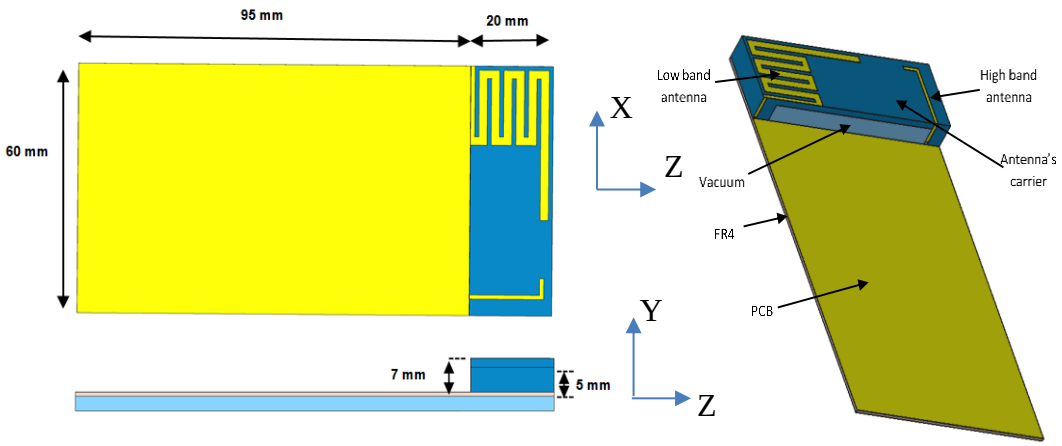

Figure 5-1: Geometry of the handset model with monopole antennas for 1900 MHz (high-band antenna) and 900 MHz (low-band antenna). FR4 for the PCB with $\varepsilon_r = 4.9$, tanδ=0.025.

The following section includes discussion about the behaviour of the reflection coefficient, current distribution and distributions of electric and magnetic near fields, and also radiation efficiency, which is an important factor in user interaction studies.

5.2.1. Reflection coefficient

For internal mobile antennas, a suitably low reflection coefficient is typically achieved by either designing the antenna part to resonate at the operating frequency or by using a separate matching circuit to match at the desired frequency. However, here the matching circuits are excluded from the antenna model, mainly because the antennas are shaped to resonate at the two GSM frequencies of practical interest, 900 and 1900 MHz, see the Figure 5-2.

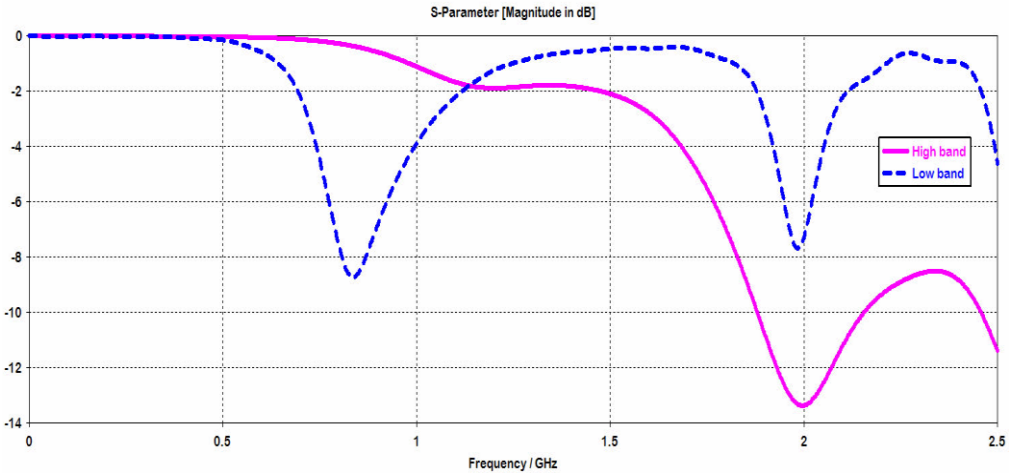

Figure 5-2: Reflection coefficient of the used antennas model in free space. Low-band antenna :900 MHz , high-band antenna :1900 MHz.

5.2.2. Current distributions

Let us spend a while looking at the current distributions of the antenna and the PCB before going through the details of the distributions of electric and magnetic fields. The current distribution of the chassis of a mobile phone with internal antennas is known to be similar to that of a thick dipole:

Figure 5.3 illustrates current distributions on the surface of the PCB ground plane at 900 MHz and 1900 MHz. At 900 MHz , the current on the monopole and chassis has one maximum value corresponding to a half-wave dipole type current distribution (close to the monopole feed point). At 1900 MHz, the effective length of the monopole with chassis is close to full-wave length, leading to two current maxima at the surface of the PCB. The surface current is concentrating at the PCB's edge.

The current distributions of the PCB can be interpreted as the two lowest order current modes of the chassis [27].

The first order current mode exists when the combination of chassis and monopole represents an electrically half-wavelength dipole. The second current mode is reached with an electrically longer chassis.

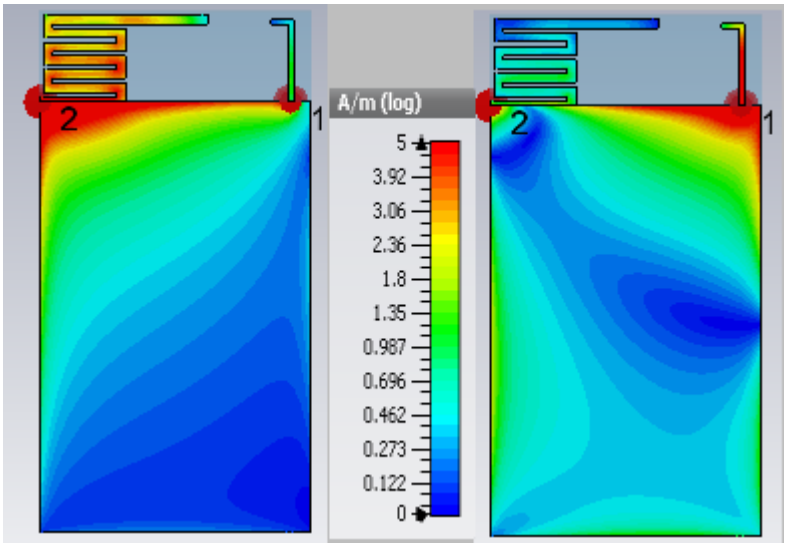

(a) (b)

Figure 5-3: Current distributions on the surface of the PCB (in free space) at frequencies (a) 900 MHz,(b) 1900 MHz. P_{inc}=1W.

5.2.3. Near field distributions

The issue of how dielectric materials and the electromagnetic fields interact with each other was discussed in Chapter 3.Dissipation losses inside the dielectric material were found to be caused by the electrical field inside the material. In the following sections the issue is re-studied to improve the understanding of the process. At the beginning of this section, the antenna field distributions are studied in free space.

Figure 5-4 shows the distributions of the electric and magnetic fields in free space on the YZ plane. The magnitudes of the fields are coded in colours, and all values are normalized to 1 W input power. The fields are noted at 900 MHz and 1900 MHz. It can be seen that at 900 MHz the resonator of antenna and chassis is excited close to the first resonance mode and at 1900 MHz is close to the second one.

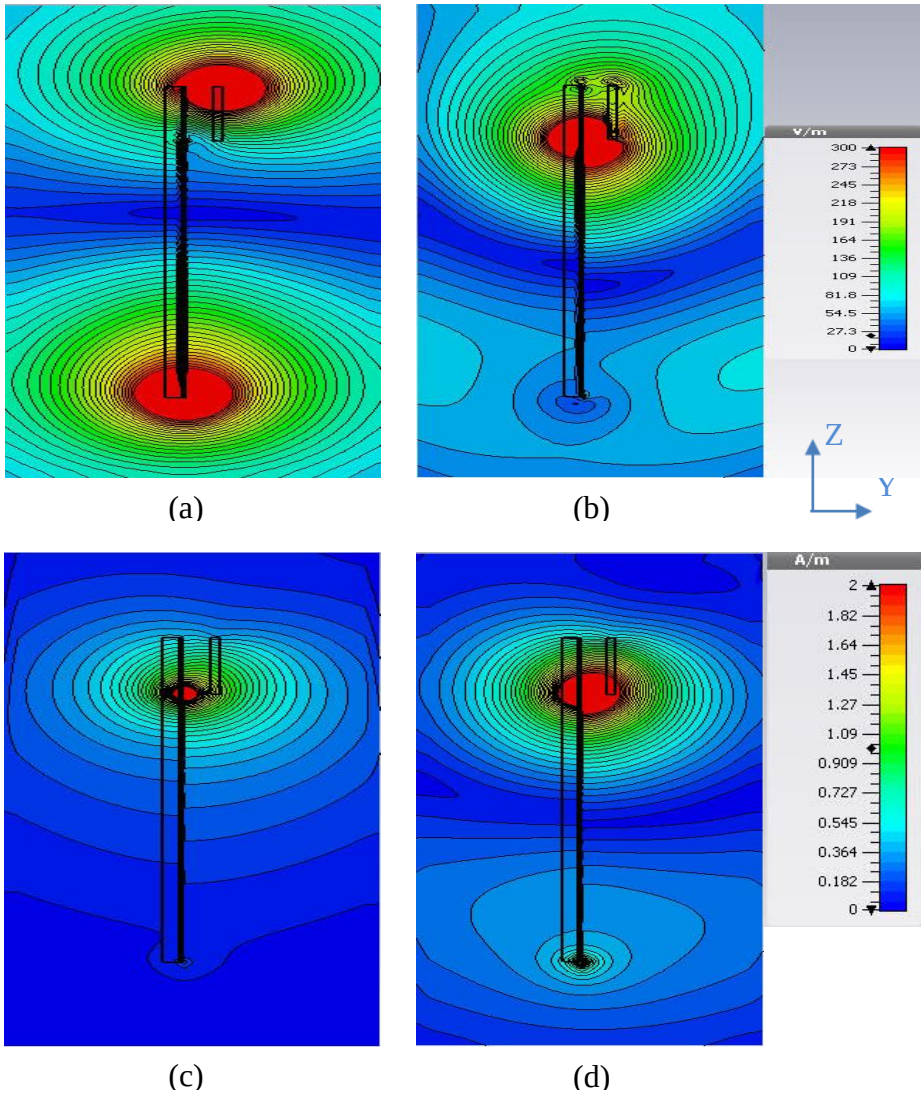

Figure 5-4 : Field distributions on YZ-plane(X=0mm) in free space. P_{inc}=1W, (a) E field at 900 MHz,(b) E field at 1900 MHz,(c) H field at 900 MHz,(d) H field at 1900 MHz .

At 900 MHz the electric field (a) is strong around both ends of the resonator (PCB + Antenna) and similar to a half wave dipole. Magnetic field (c) is concentrated significantly around the vertical (Y direction) feed point of the antenna. At 1900 MHz the length of the PCB is close to full wavelength, therefore the current has two maxima in z-direction along the PCB and a minimum close to the center of the PCB.

Consequently, the electric field has a strong area around the center of the PCB in addition to the strong areas at the ends of the resonator, and magnetic field high values around areas in which the current on the resonator is high. The relation between surface currents and fields of the antenna can be detected by comparing Figures 5-3 and 5-4.

5.2.4. The effect of chassis length on antenna performance and SAR

The effect of the handset chassis (PCB) length on the antenna performance and interaction between the antenna and near dielectric material was studied before [2], [28], [29]. While most of the earlier studies were done with PIFA or capacitive coupling element, in this chapter the chassis with monopole antenna is simulated near a dielectric block of 120 x 180 x 110 mm^3. Distance between the ground plane of the antenna (PCB) and the dielectric block is d=10mm.The dielectric block has properties of head tissue-equivalent material given before in Table 3.1.

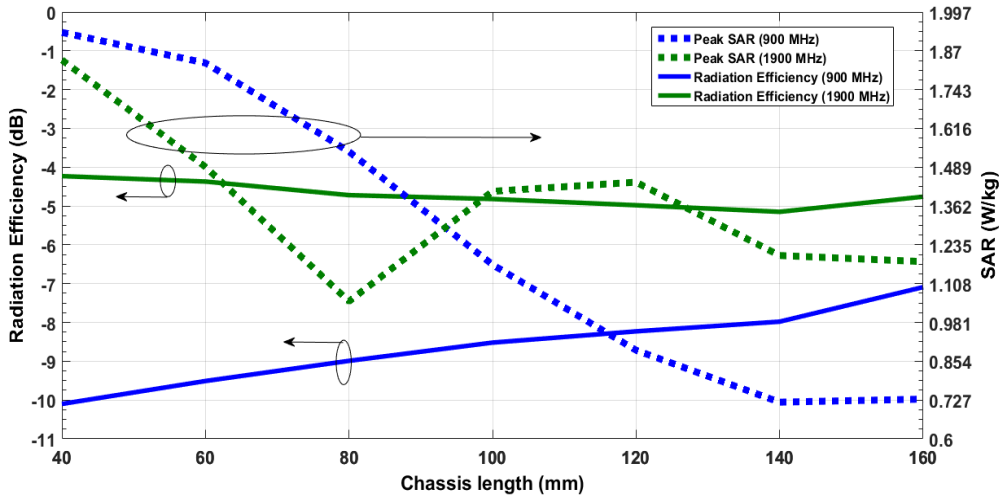

Figure 5-5: Radiation efficiency of the two antennas beside the dielectric block and peak SAR(10g) at 4 mm below the surface of the dielectric block; P_{acc}= 0.2 W.

The length of 95 mm of the chassis (as in Figure 5-1) is less than half-wavelength at 900 MHz; from the Figure 5-5 it can be seen, that the radiation efficiency is low at this chassis length, and as the chassis length increases, efficiency increases rapidly, while the peak SAR value decreases. This can be explained by the increasing distribution of the current over the chassis length when the length approaches half-wavelength. With this, the peak current density on the chassis and the peak current density inside the dielectric block reduce accordingly. Since the power dissipation (SAR) is proportional

to the product of current density and E-field, see (3.5), the peak SAR reduces more than proportional and even the total dissipated power(used to calculate the radiation efficiency) reduces.

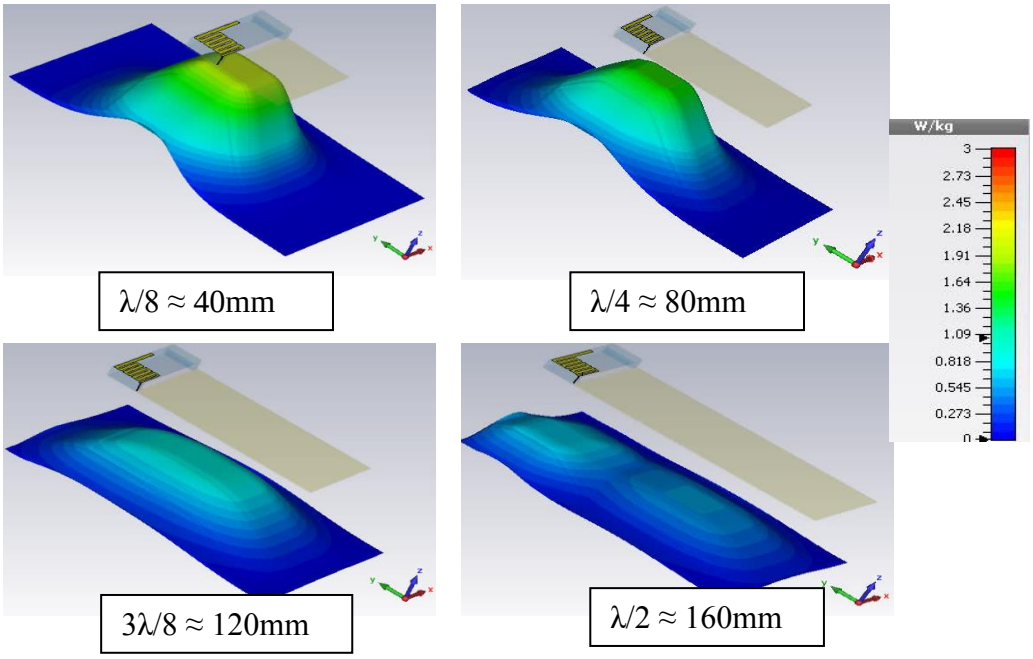

Figure 5-6: SAR distribution in XY-plane at 4mm below the surface of the dielectric block, at frequency 900 MHz as function of chassis length; P_{acc}= 0.2 W.

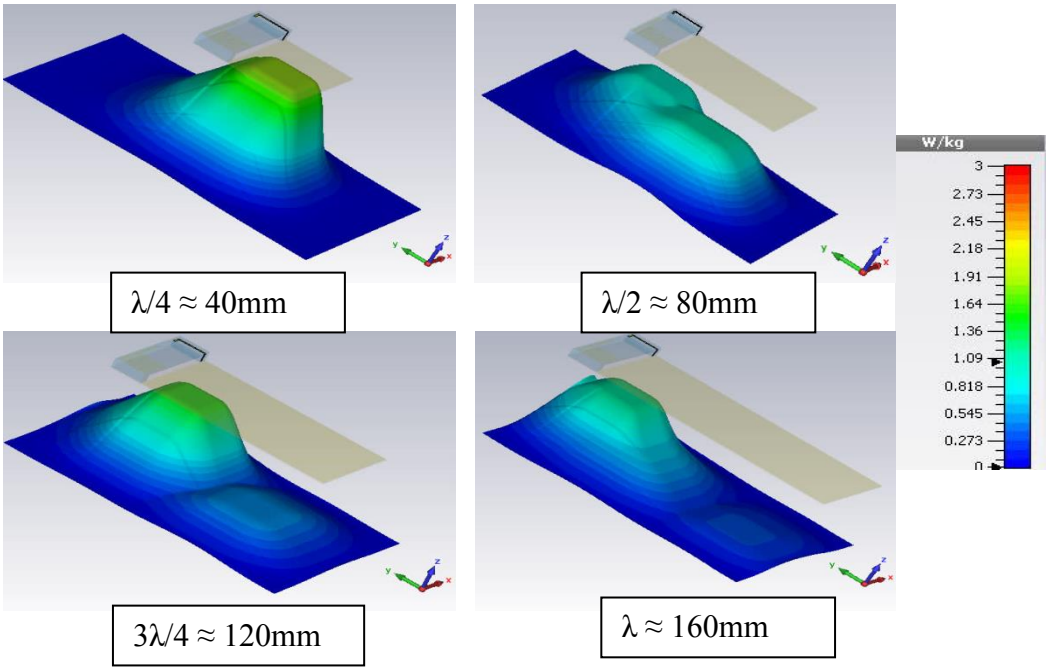

Figure 5-7 : SAR distribution in XY-plane at 4mm below the surface of the dielectric block, at frequency1900 MHz as function of chassis length; P_{acc}= 0.2 W.

At 1900 MHz, the monopole antenna is the main radiator and the effect of the ground plane current mode on the radiation efficiency is small. However, we see a similar effect on the peak SAR when the surface current approaches the half-wavelength distribution near 80 mm length. Figure 5-6 and Figure 5-7 show the SAR distribution with IEEE C95.3 calculation standard at 900 MHz and 1900 MHz respectively.

In all cases at 1900 MHz, the current distribution is more concentrated close to the monopole (even in $\lambda/2$ –case) than at 900 MHz. Never-the-less , the peak SAR values at 1900 MHz reduce in a similar pattern as at 900 MHz , producing a minimum at half-wavelength due to the effective current distribution over most of the chassis.

It is interesting to see that the radiation efficiency is less at 900 MHz than at 1900 MHz even at chassis sizes larger than 100 mm where peak SAR is lower at 900 MHz. This is an indication of the much smaller decay of the reactive near field at 900 MHz which extends into the lossy dielectric medium and creates the dissipation loss over a larger volume than at 1900 MHz.

From the Figure5-6 & Figure 5-7, it is found for mobile phones with chassis length 90 to 110 mm, that for 900 MHz the SAR distribution is dominated by the chassis currents, in accordance with the location of the peak SAR values at the center of the chassis. For the higher frequency (1900 MHz), the main contributor is the antenna, since the location of peak SAR follows the location of the antenna.

When the chassis is longer than 95 mm, the peak SAR (10g) at 4 mm below the phantom surface at 1900 MHz is higher than at 900 MHz. Since the transmit power to cover the requirements of WCDMA can be as high as 30 dBm, the 1900 MHz band is considered critical with respect to SAR limits.

Chapter 6

6. SAR control mechanisms and concepts for mobile phone antennas with reduced SAR

6.1. Introduction:

As we already see from the analysis of absorption mechanisms for mobile phones and behaviour of mobile terminal antennas near dielectric material, the currents of the chassis at the low cellular frequencies (GSM 900) and of the antenna element at the high cellular frequencies (GSM 1900) cause high peak SAR values, which especially at the GSM 1900 band is quite often problematic. Most of earlier studies on SAR reduction methods are of limited use because the antenna efficiency in free space before and after reduction of SAR was neglected, or because there is not enough space in the phone to realize the proposed concept. This is why the actual solution in present commercial phone products is simply reducing the input power of the antenna.

In this chapter, SAR control mechanisms and state of the art solutions for reducing SAR of internal antennas are introduced. In addition, some own solutions are proposed with simulation and experimental results.

6.2. State of the art of SAR control:

From earlier studies, solutions to SAR control for mobile phones can be categorized into three methods: Controlling the direction of radiation to weaken radiation toward the human body by redirecting the currents on the chassis, optimizing the antenna/PCB configuration and shielding the EM fields against the human body.

Parasitic elements, directive control antenna pairs fed in 180° phase difference, wavetraps and slots in the PCB ground plane are the methods used to control the current distribution and the direction of radiation in the near field, while ferrite, conductors and AMC (Artificial Magnetic Conductor) can be used to disperse or attenuate the EM fields radiated against the human body.

6.2.1. Parasitic Elements

The proposed method in [30] comprised a (900/1800 MHz) PIFA combined with a parasitic radiator placed on the backside of the ground plane and connected by two conductors. It was shown in [30] that peak SAR reached a minimum when the length of the parasitic radiator was L=45 mm (at 900 MHz). When the results were compared to the case when no parasitic radiator was attached to the ground plane, the SAR reduced by approximately 5 dB in the simulations (from 1.5 W/kg to 0.5 W/kg for 0.25 W antenna accepted power). In measurements, the reported reduction in SAR was 6 dB, total efficiency in talk-position (beside phantom) was approximately 1 dB higher with the 45 mm long parasitic radiator compared to the reference case (no parasitic radiator). Even if this SAR control method seems to be working quite nicely at 900 MHz, the operating principle of the parasitic radiator was left somewhat unclear at 1900 MHz. It was only mentioned that the effect of the parasitic radiator would be to cancel a part of the near field that is coupled into the head. Furthermore, it was concluded that the cancellation of the near field would be caused by the currents of the parasitic radiator, which are opposite in direction to the currents on the chassis.

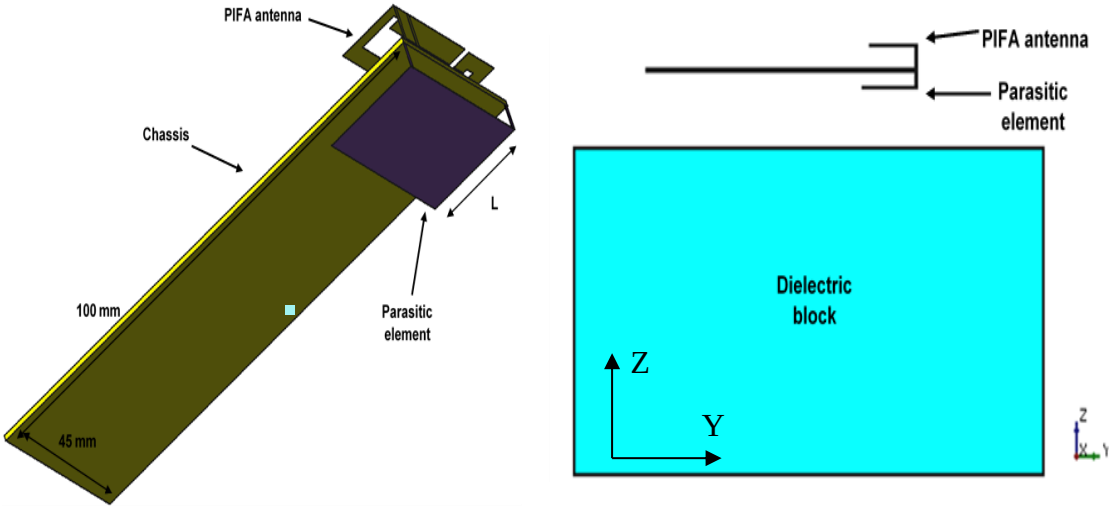

Figure 6-1 : Geometry of the simulation structure, showing PIFA antenna with parasitic element, both above the dielectric block (body) σ_{eff} =1.4 S/m, $\varepsilon_r' = 40$.

The concept was investigated by an own simulation using CST Microwave Studio. Figure 6-1 shows the simulation structure of an antenna model including a parasitic element as a SAR shield sitting beside a dielectric block. A PIFA antenna is mounted on a metal chassis (45×100 mm) with a metal parasitic radiator (L×45 mm) on the backside. A dielectric block is located at 10 mm below the structure and filled with head tissue equivalent material; dimensions of the dielectric block (Body) are 120 × 180 × 110 mm^3, L is 45 mm for 900 MHz and 22 mm for 1900 MHz .

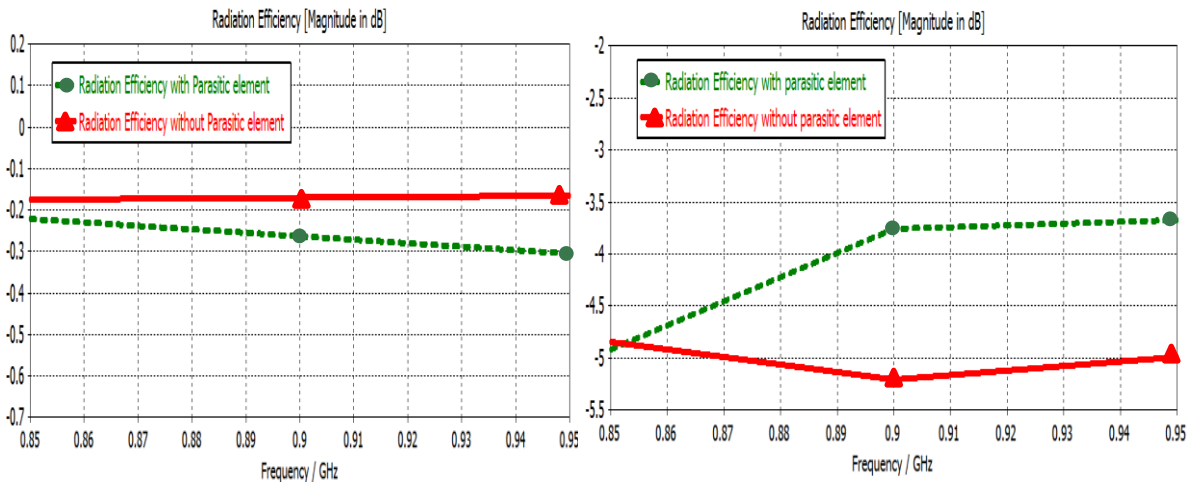

(a) (b)

Figure 6-2: Radiation efficiency at low-band (900 MHz) without and with parasitic element, L=45 mm, (a) in free space, (b) beside the body.

From the Figures 6-2, 6-3, it is observed that at 900 MHz this method can reduce SAR (10g) from 1.2 W/Kg to 0.87 W/Kg with a corresponding 1.5 dB increase in the efficiency beside the dielectric block, due to reduced E-field in the block (body) where most of the losses are generated. While the free space radiation efficiency is very slightly reduced by 0.12 dB at 900 MHz, and at the high frequency 1900 MHz the peak SAR is not affected by the parasitic radiator.

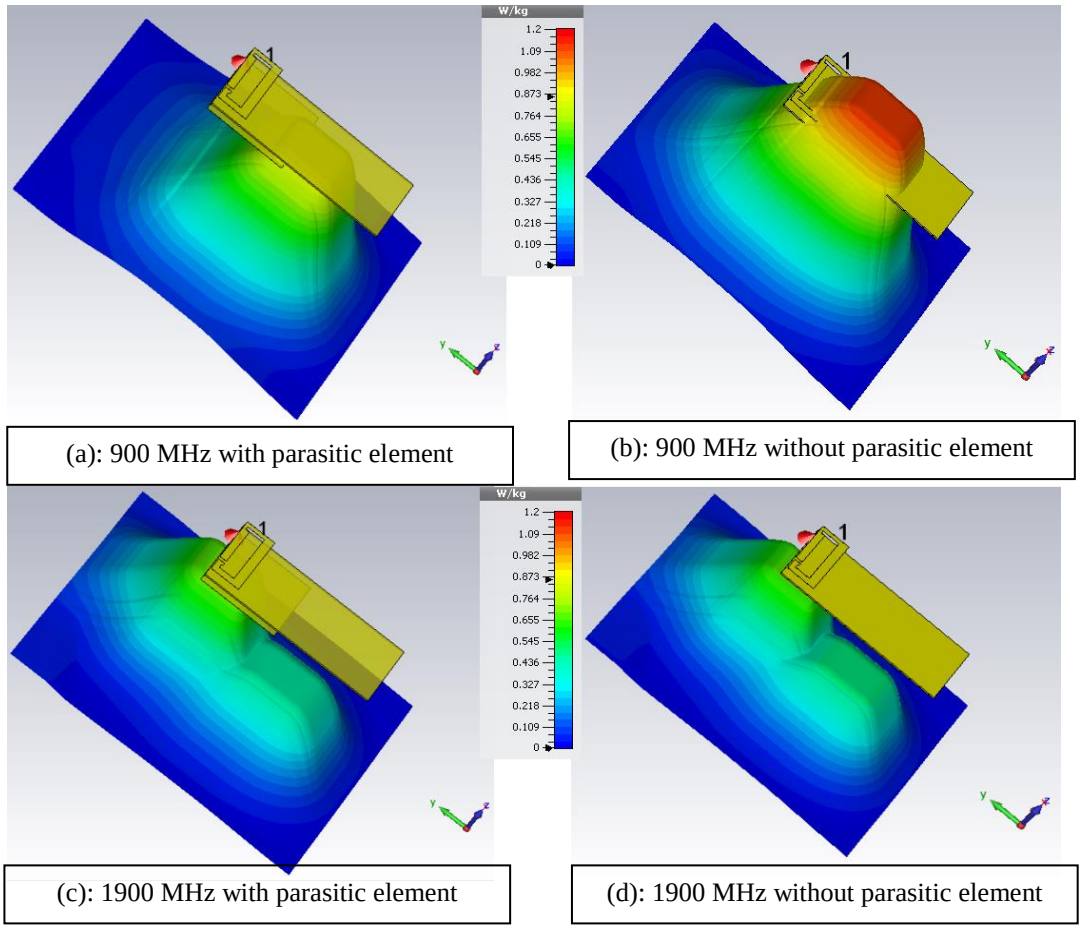

Figure 6-3: Simulated SAR distribution inside the dielectric block (body) 4mm below the surface at 900 MHz and 1900 MHz. P_{acc}=0.25 W , L=45 mm.

Figure 6-4 shows the radiation pattern of the PIFA antenna with and without parasitic element at 900 MHz and 1900 MHz. At 1900 MHz the radiation pattern is not affected by the parasitic element with L=45 mm; therefore the parasitic element is a good solution to reduce SAR at 900 MHz without affecting the antenna parameters at 1900 MHz.

With a parasitic element's length of L=22 mm ,matched for the high frequency 1900 MHz, the max SAR value is even slightly increased, Figure 6-5; therefore the parasitic element could not be a solution for high SAR at the critical frequency 1900 MHz.

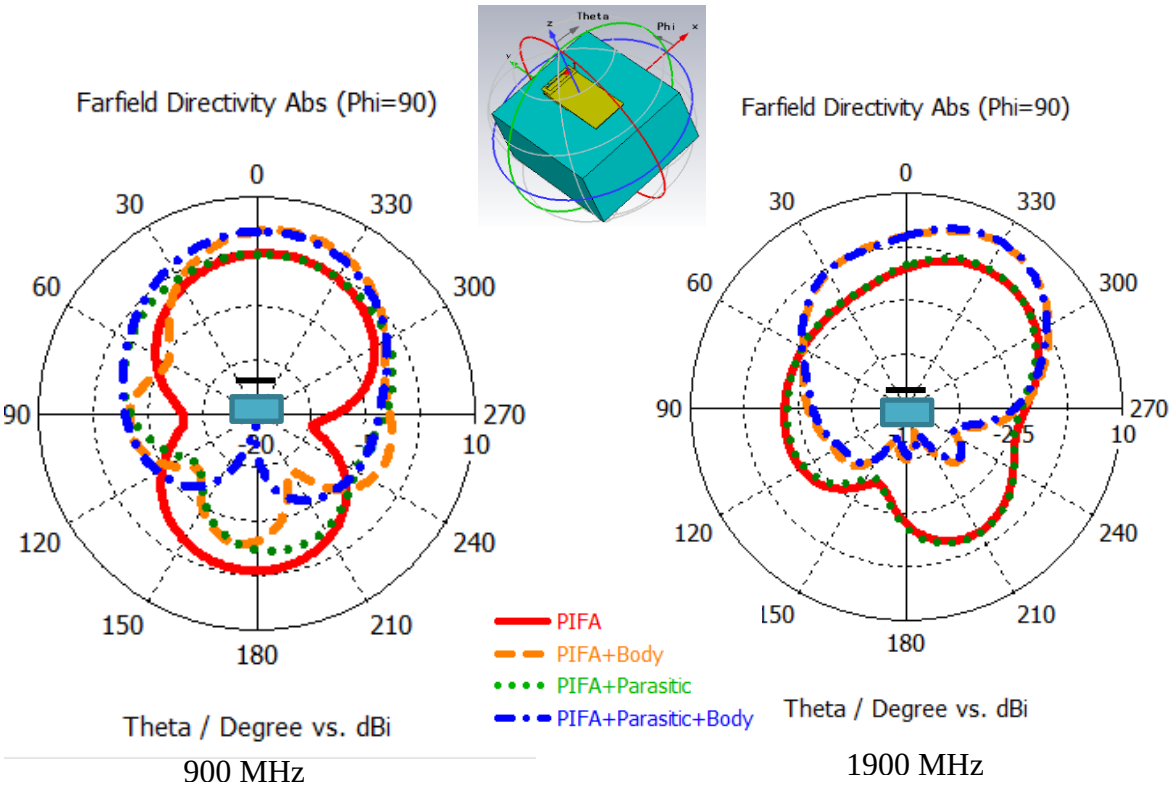

Figure 6-4: Far-field radiation pattern of PIFA antenna at 900 MHz and 1900 MHz, in free space or near block and with or without parasitic element.

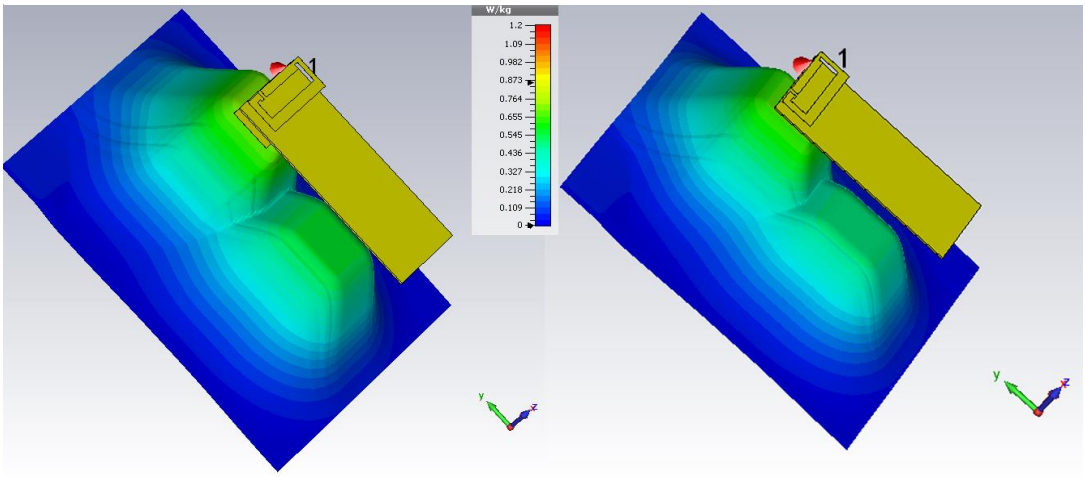

(a): 1900 MHz with parasitic element, Peak SAR(10g)=0.722 w/kg

(b): 1900 MHz without parasitic element, Peak SAR(10g)=0.65 w/kg

Figure 6-5: Simulated SAR distribution inside the dielectric block (body) 4mm below the surface at 1900 MHz . P_{acc}=0.25 W, L= 22 mm.

6.2.2. WaveTraps:

As was shown, the chassis of the mobile terminal has a significant effect on the antenna operation because the chassis operates as a significant radiator below 2 GHz. In [31], wavetraps are used to control the current distribution on the chassis and by this the near field of a mobile terminal antenna at GSM 900 and GSM 1900 frequencies. This concept was investigated by own simulations:

Figure 6-6 shows the structure with wavetraps after [31], which work efficiently when they are in resonance, i.e. the structure represents a quarter wavelength transmission line, with the impedance equation:

$$Z_{\mathrm{in}} = \mathrm{j}Z_{\mathrm{o}}\tan(\gamma L_{\mathrm{WT}}) \qquad (6.1)$$

Z_{o}: The characteristic impedance of the transmission line formed by the wavetraps and the ground plane, L_{WT} is the length of the wavetrap, $\gamma=\alpha+\mathrm{j}\beta$ is the propagation constant with real part $\boldsymbol{\alpha}$ being the attenuation constant and imaginary part $\boldsymbol{\beta}$ being the phase constant.

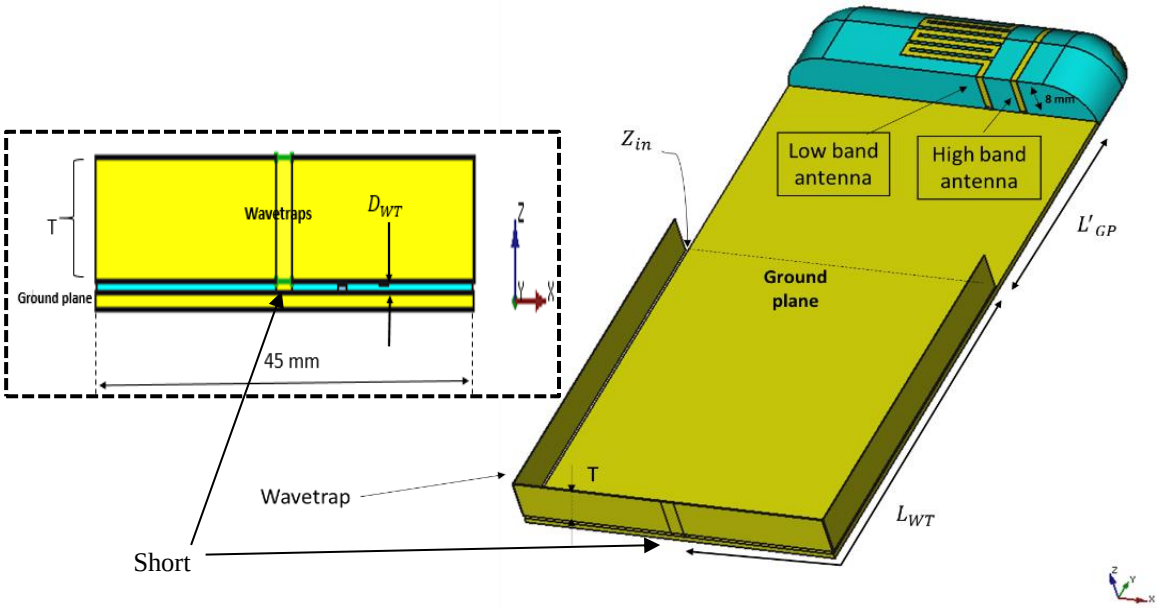

Figure 6-6 : Low-band 960 MHz terminal antenna with 8 mm height of the monopole antenna, and wavetraps height D_{WT} =0.5 mm above the ground plane and thickness T=6mm, L_{WT}=77mm, L'_{GP}=40 mm (after [31]).

Without wavetraps Figure 6-7 (b) the chassis shows a thick half-wavelength dipole-type current distribution, and the currents induced by the antenna element are concentrated at the edges of the chassis.

Figure 6-7 (a) shows that the wavetraps create a high impedance location on the chassis and thus create a new chassis wave mode and especially avoid the null of electric currents at the open end of the chassis with high current density and high magnetic field in the middle. Due to this current distribution the near-field pattern maximum is moved away from the head, and the peak SAR value is reported to be decreased by 23%. [31]

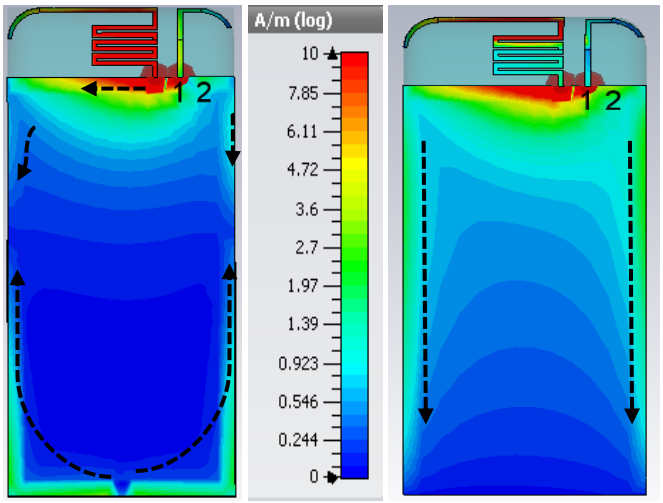

(a) (b)

Figure 6-7 : Simulated surface current distributions at 960 MHz with wavetraps $L_{\mathrm{WT}} = 77\ mm$ (a) and without wavetraps (b)

For our own investigation of SAR effects in real use cases, Figure 6-8 shows the simulation setup of a mobile phone structure beside the head with cheek position, and two antenna positions:

1. Top-mounted antenna: antenna is located close to the Head.
2. Bottom-mounted antenna: more distance between the head and the antenna.

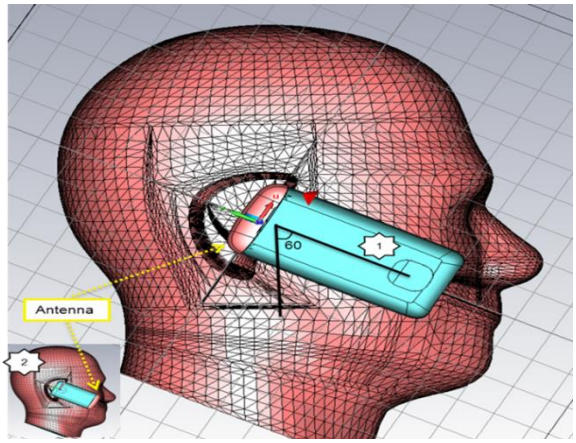

Figure 6-8 : Simulation of the mobile phone beside the phantom head in cheek position.

For the top-mounted antenna position, simulation results in Figure 6-9 show the E-field & H-field distribution close to the head with and without wavetraps at the resonance frequency of the wavetraps 960 MHz.

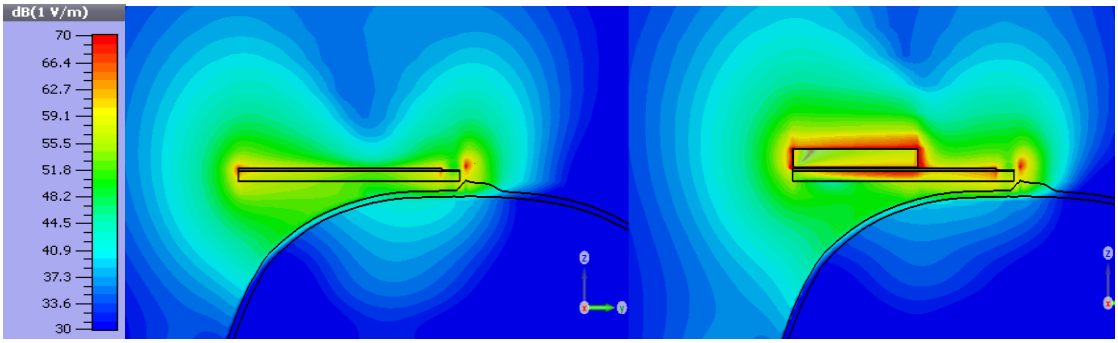

E-Field without wavetraps E-Field with wavetraps

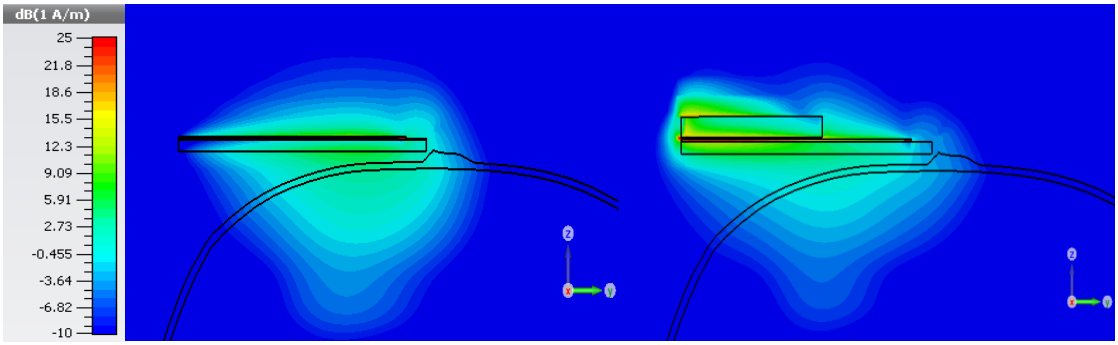

H-Field without wavetraps H-Field with wavetraps

Figure 6-9 : Simulated E & H field distributions for the top-mounted low-band monopole antenna beside the head, with and without wavetraps at the resonance frequency of the wavetraps 960 MHz.

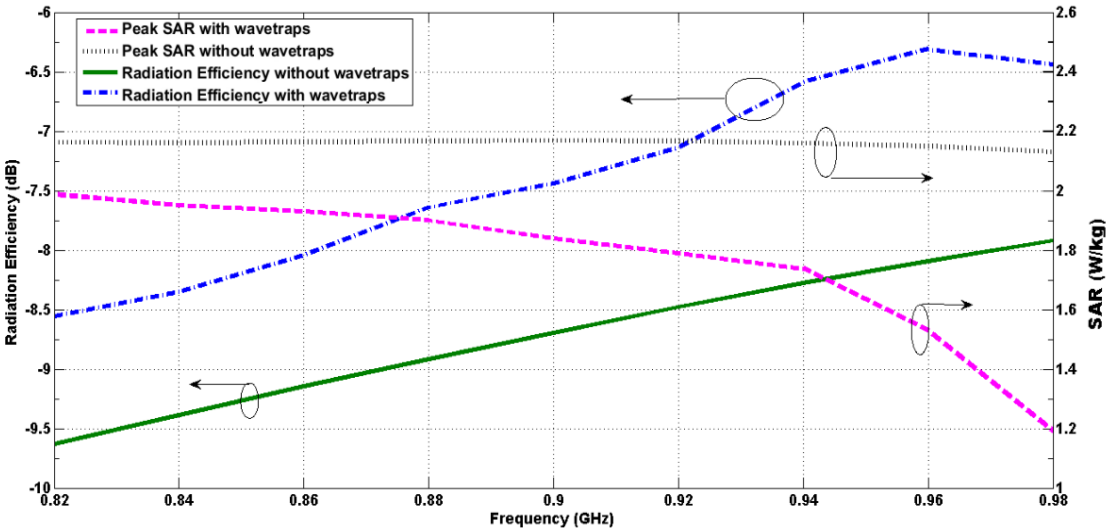

Figure 6-10: Simulated antenna radiation efficiency and peak SAR (10g) values with/without wavetraps for the top-mounted low-band monopole antenna beside the phantom's head, P_{acc}=0.25 W.

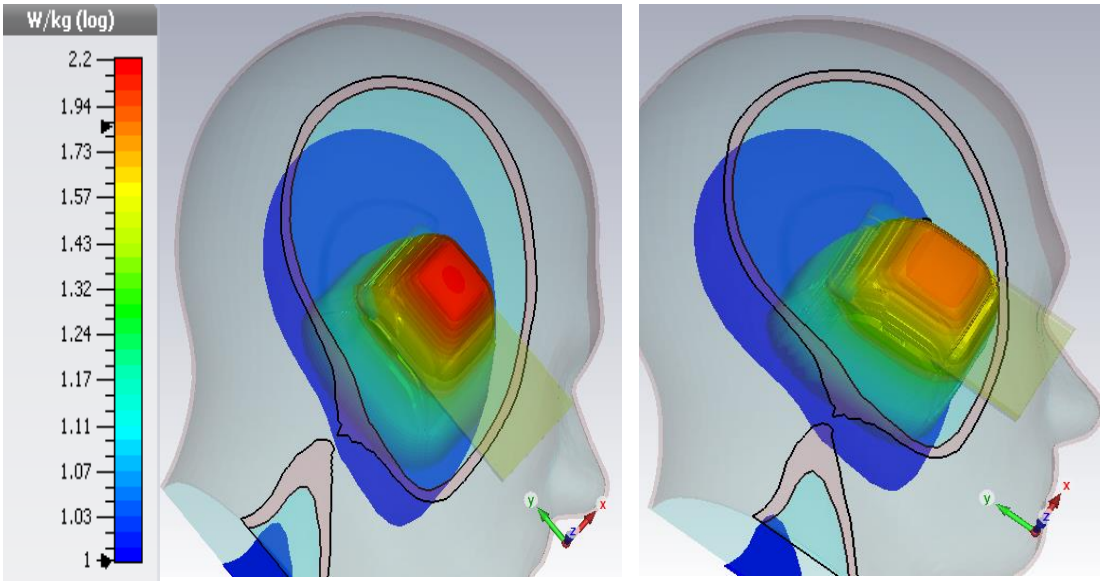

Without wavetraps. With wavetraps.

Figure 6-11: SAR distributions inside the phantom's head at 960 MHz, with and without wavetraps, in top mounted antenna configuration, P_{acc}=0.25 W.

The effect of the wavetraps operated at its λ/4-resonance is seen at 960 MHz from the change in the E&H-field distributions, where the new maximum E-field and minimum H-field appear at the center of the PCB (open-circuit of wavetraps), producing reduction in the E&H-field distributions inside the phantom, while increasing the E&H-field outside the phantom. Therefore, the SAR peak value is reduced from 2.18

to 1.53 W/kg, as seen in Figure 6-10 as a function of frequency. By this, also the radiation efficiency increases by nearly 2dB.

Figure 6-11 shows the SAR distribution for this case. We see that the peak SAR position still is the same with and without wavetraps, and remains close to the feed point of the top-mounted monopole antenna, yet the peak SAR level is lower with the wavetraps.

Most of the handsets in the market have the bottom mounted antenna position, because of the favoured antenna type has shifted from PIFA (metal ground between the antenna and the user) to monopole type (off ground antenna concept), which has higher SAR value compared to PIFA antenna ,and with the bottom-mounted monopole antenna has less interaction between the antenna and the user's body . Figure 6-12 shows the E- field & H-field distributions close to the head with and without wavetraps at 960 MHz in bottom-mounted antenna configuration.

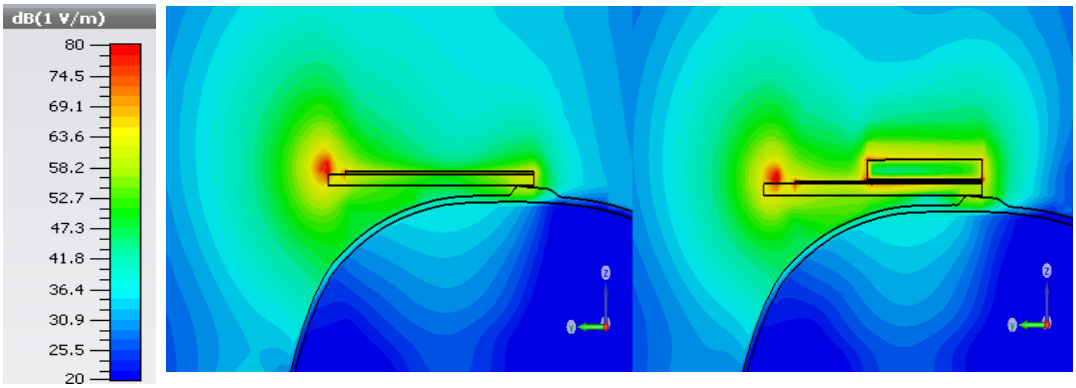

E-Field without wavetraps E-Field with wavetraps

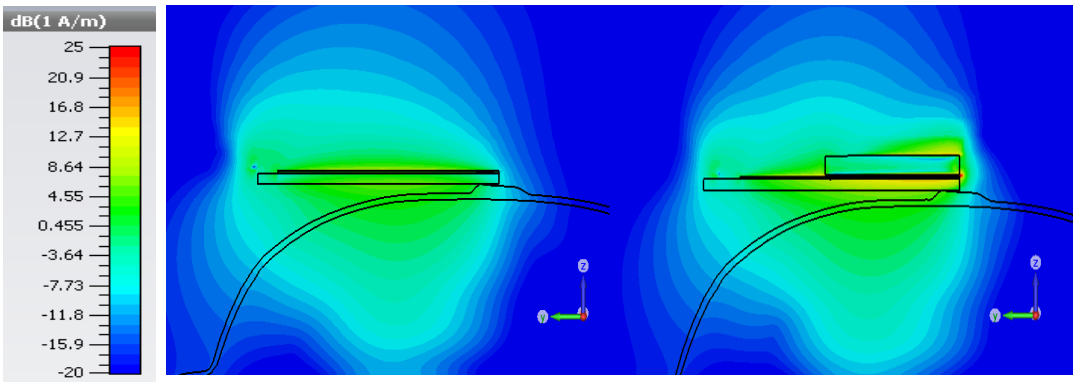

H-Field without wavetraps H-Field with wavetraps

Figure 6-12: Simulated E-& H-field distributions for the bottom mounted low-band monopole antenna beside the head, with and without wavetraps at the resonance frequency of the wavetraps 960 MHz, P_{acc}=0.25 W.

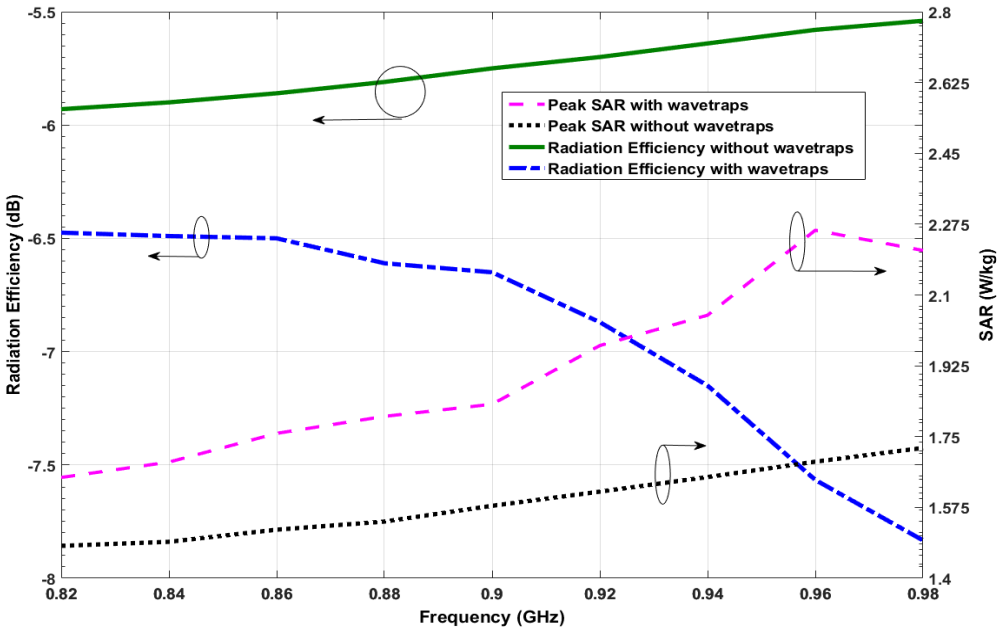

Figure 6-13 : Simulated antenna radiation efficiency and peak SAR (10g) values with/without wavetraps beside the phantom's head in bottom-mounted antenna configuration, P_{acc}=0.25 W.

Due to the location of the open end of the wavetraps, strong E-&H-fields move closer to the head, producing higher magnitudes inside the phantom's head. As a consequence, Figure 6-13 shows that the peak SAR at the wavetraps resonance frequency is increased while the antenna efficiency drops due to the wavetraps.

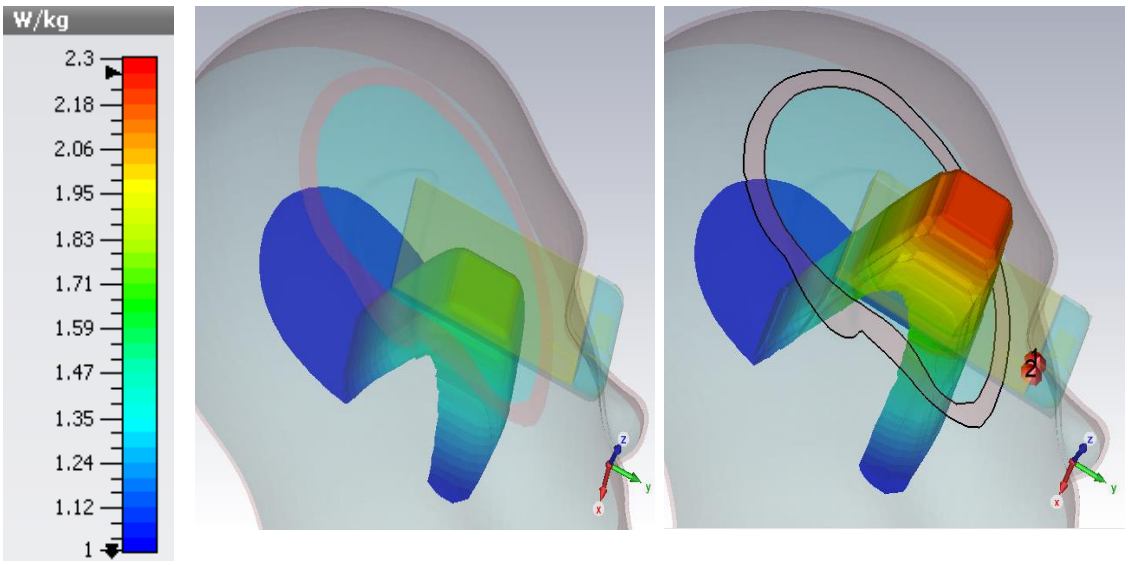

Figure 6-14: SAR distributions inside the phantom's head, SAR (10g) values are 1.7 W/kg standard antenna without wavetraps, 2.27 w/kg with wavetraps at 960 MHz, P_{acc}=0.25 W.

Figure 6-14 plots the SAR distributions and the peak SAR location inside the phantom by 4 mm with and without wavetraps. Due to the shift of the surface current distribution to the upper end the hot spot (peak SAR location) move to the upper end of the PCB, compared to the case without the wavetraps.

From the wavetraps investigation, it is found that they are not suitable as solution to reduce SAR in all antenna positions. In addition the wavetraps have some disadvantages, such as size, operation bandwidth, and require careful design to avoid high SAR and lower antenna efficiency under special user conditions, and due to the effect of the battery, metal cover, and other relevant parts of real handset on the wavetraps functionality. Due to these disadvantages, no further study is done at the GSM 1900 band.

6.2.3. Directive control antenna

This solution is used to control the direction of radiation pattern so as to weaken radiation toward the human body [32], [33]. In the study [32], the dividing feed directive control antenna (DFDCA) is proposed for a clamshell type handy phone.

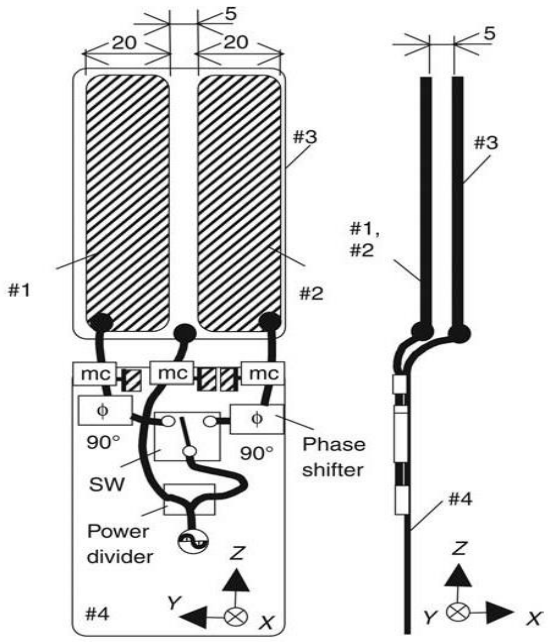

Figure 6-15: Antenna structure with power divider and 90° phase shifter and switch, at 2.14GHz; from [32] .

Figure 6-15 shows the DFDCA which is composed of three antenna elements (#1,#2,#3) and a dividing feed circuit. The directive control is implemented in the feeding phase difference between the elements. The radiation in the direction of the user's shoulder and head is reduced by the directive control.

Measurement of the radiation characteristics of the proposed antennas in the talk and viewer positions by the fabricated models and simulation using the FDTD method at 2.14GHz band are reported. As a result, the radiation efficiency of the DFDCA in the talk position is reported to be improved by 2.4 dB, which is quantitatively demonstrated by reduced absorbed power in the human body, relating to a whole-body SAR reduction of up to 90%.

This concept has similar disadvantages as the parasitic element concept: three radiators require space, and need to be designed carefully to avoid high SAR under special user conditions due to the hand effect. Additionally, the concept requires a phase shift feed in each element and one extra switch.

6.2.4. Slotted ground plane:

The popular way to design handset antennas is by modification of their geometry, and as shown in chapter 5, the PCB of the handset plays a very important role in the antenna system’s behaviour.

First reports of handsets with slotted ground plane (PCB) studied the improvement of the antenna’s bandwidth by increasing the PCB electrical length to get the optimum length ~0.4λ in GSM850 and GSM900 [34], [35]; for example, a length of 0.4λ at 900MHz is approximately 133mm and the typical physical length of the PCB is 100-110 mm. Later studies were done to use this reshaping idea to decrease SAR [36].

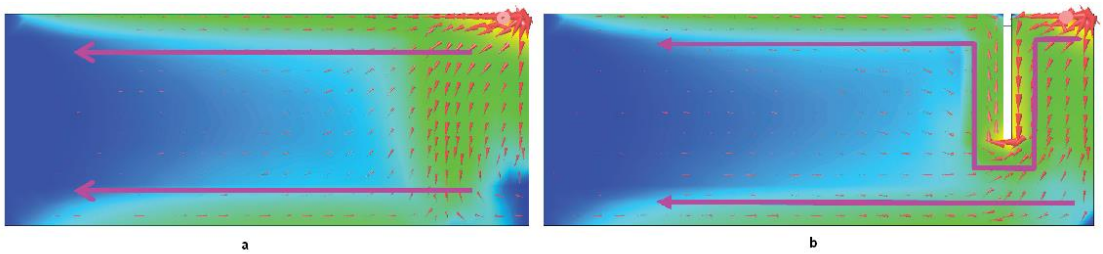

Figure 6-16 : Surface current distributions on a PCB of 100 mmm at frequency 900MHz, with slot (right). From [35]

.For illustration, Figure 6-16 shows the simulated surface current distribution on a PCB with and without a slot. The reforming of the current distribution increases the electrical length of the PCB. Reference [35] studies the reduction of the interaction between the head and the handset PIFA antenna by using a slotted ground plane and evaluates two positions top and bottom. At 900 MHz, which was representative of the low-frequency region, the SAR values did not vary between the top (up) and bottom (down) mounted antenna positions.

In the first position, the handset's antenna is located near the phantom ear (up position), in the second position, the handset device was rotated 180°(down position),and SAR is decreased in high-band 1900 from 2.7 to 1.2 W/kg (70%) and radiation efficiency is improved 67% with the U-shaped slot in its ground plane and up position ,Figure 6-17.

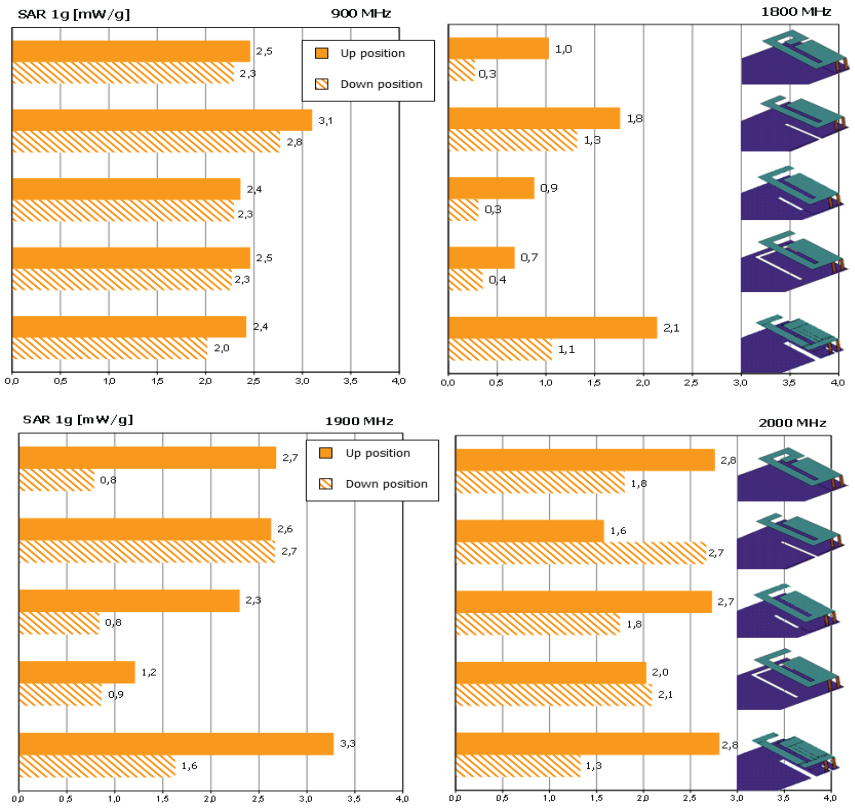

Figure 6-17: The measured SAR (1g) values for the PIFA with slot when the handset antenna was located above the phantom's ear (up position), and for a 180° rotation (down position).From [35]

The high frequency selectivity of the slot was the first problem with using a slot in the PCB as high SAR solution in handsets. The second problem can arise in the practical

structure from the effect of the metal parts (battery, battery metal cover,..) on the slots functionality.

6.3. Advanced concepts for SAR control:

In this part some concepts for SAR reduction are presented, and evaluated. iSAR is used as SAR measurement tool to evaluate the SAR distribution improvements.

6.3.1. Antenna Type Optimization (Dual-Loop,)

In practical handsets, most monopole type antennas suffer from excessive SAR values; therefore antenna designers seek antennas with multiband capabilities and low SAR values. As one suitable candidate, Figure 6-18 shows a single-loop antenna, which is a multiple-resonance antenna; this antenna can lead to small-excited surface current distributions on the system ground plane (PCB).

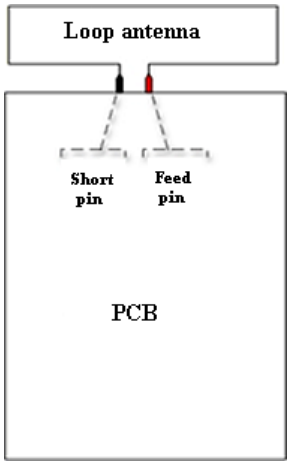

Figure 6-18: Principle layout of a single-loop antenna mounted on the PCB with one feed pin and short pin.

As was found in section 5.2.4, it can be expected that the chassis current effects at the user's head will become small, when the excited surface current distribution on the system ground plane is small.

A bottom-mounted folded dipole antenna (single-loop), tuned to work at cellular frequencies can have three operational modes, as shown in [37]. Two of the resonance modes, first and third, are called **'Common Modes'** standing for the antenna operation where the antenna element couples strongly with the antenna ground, the PCB, in the same way as two monopoles which are excited in phase. In this mode the antenna excites currents along the long edge of the PCB, which in turn excite near fields around the phone. SAR behaves similar as with any other bottom-mounted monopole antenna.

The second (middle) mode, is called **'Differential Mode'**, or Balanced mode. It concentrates the ground currents in the vicinity of the antenna, along the short edge, therefore suppressing the currents along the long edge of the PCB. In this mode the antenna is working like a dipole along the narrow dimension of the PCB. Since the antenna is mounted at the bottom of the

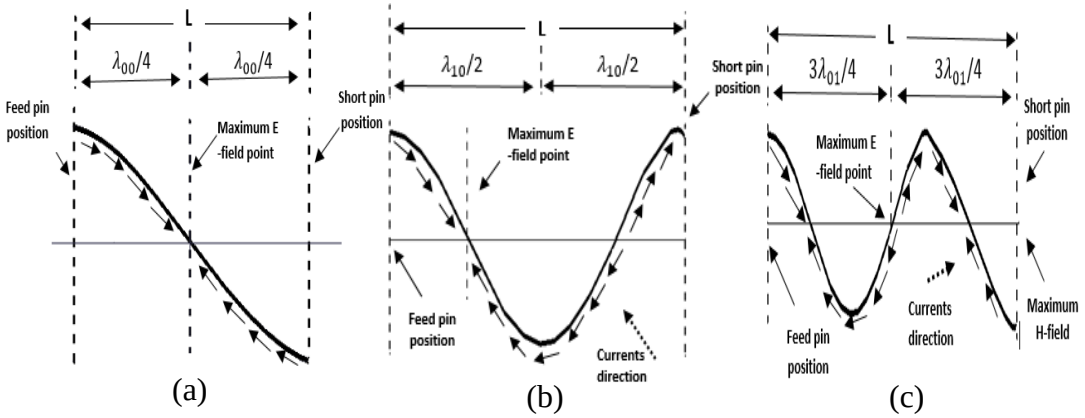

Figure 6-19: Resonance modes and current distributions of single-loop antenna, (a):0.5λ Common mode,(b) 1.0 λ Differential mode ,(c) 1.5 λ Common mode.

phone, most of the currents are flowing in the area, where the distance to the head is maximized, with SAR values reduced. The Figure 6-19 shows the three operational modes of the single-loop antenna: 1st harmonic (a) 0.5λ effective length, equivalent to a pair of folded monopoles with common mode excitation used for GSM 850/900. 2nd harmonic (b) 1.0λ effective length, equivalent to a folded dipole with differential mode excitation used for GSM 1800, which is called low SAR mode. 3rd harmonic (c) 1.5λ effective length , equivalent to a pair folded monopoles with common mode excitation used for GSM1900.

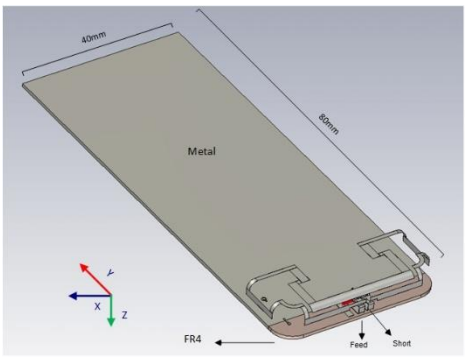

Figure 6-20: Geometry of the investigated structure with single-loop antenna's dimensions (15×40×10mm^3). The ground plane (PCB) is represented by a copper sheet of 0.1 mm thickness.

Figure 6-20 shows a single-loop antenna at one end of a PCB of 1×80×40mm^3; the feeding and shorting pins locations are at the center of the antenna in order to make the current distributions symmetrical on the ground plane. This structure is used in the following to investigate the loop antenna as low-SAR antenna design in simulation and measurement. This loop has three resonance frequencies at 0.92 GHz, and 1.75 GHz, 1.87 GHz.

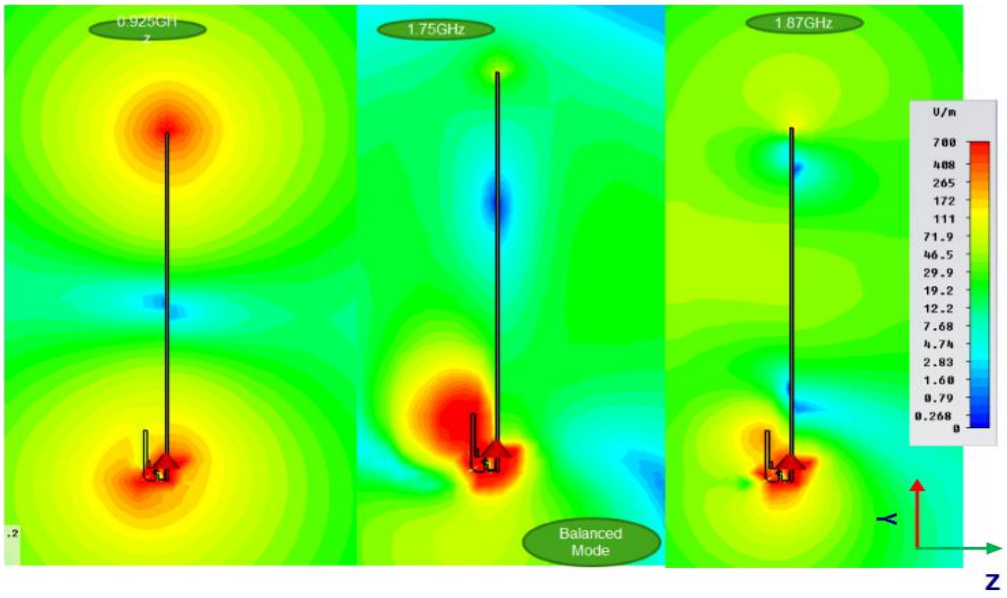

Figure 6-21: The total amplitude of electric field distributions at resonance frequencies 0.92 GHz, and 1.75 GHz, 1.87 GHz.

At 1.0λ effective loop length the differential mode or balanced mode is excited, the excited current at the PCB suppressed to zero since the feed bin current equal to the return current and in the opposite direction from the short pin.

Figure 6-21 shows the absolute value of E-field on the Y-Z plane at the three antenna resonance frequencies 0.92 GHz, and 1.75 GHz, 1.87 GHz. The coupling between the PCB and the antenna is suppressed at the balance mode, as seen at 1.75 GHz. Therefore, this antenna type is used at the balanced mode improve the Hearing Aid Compatibility (HAC) [38] and can be considered a low-SAR antenna.

For the problematic frequency band GSM 1900 (1.86 to 1.92 GHz), a major reduction of SAR values is sought. This could be realized by using the balanced/differential mode at GSM 1900 in place of GSM 1800 band with less change of the antenna's bandwidth. For the normal folded loop the mode order is always common – differential – common; therefore, the loop can be used to cover the GSM 850/900, GSM 1800, and GSM 1900 bands, where favourable SAR performance occurs at GSM1800 band.

However, adding a second loop path to the folded loop, to form a dual-loop [39], makes it possible to change the mode order to common – common – differential. Therefore, the dual-loop can be used to cover 850/900 – 1800 – 1900 bands, establishing the favourable SAR performance at the 1900 band. Figure 6-22 shows the proposed dual-loop antenna.

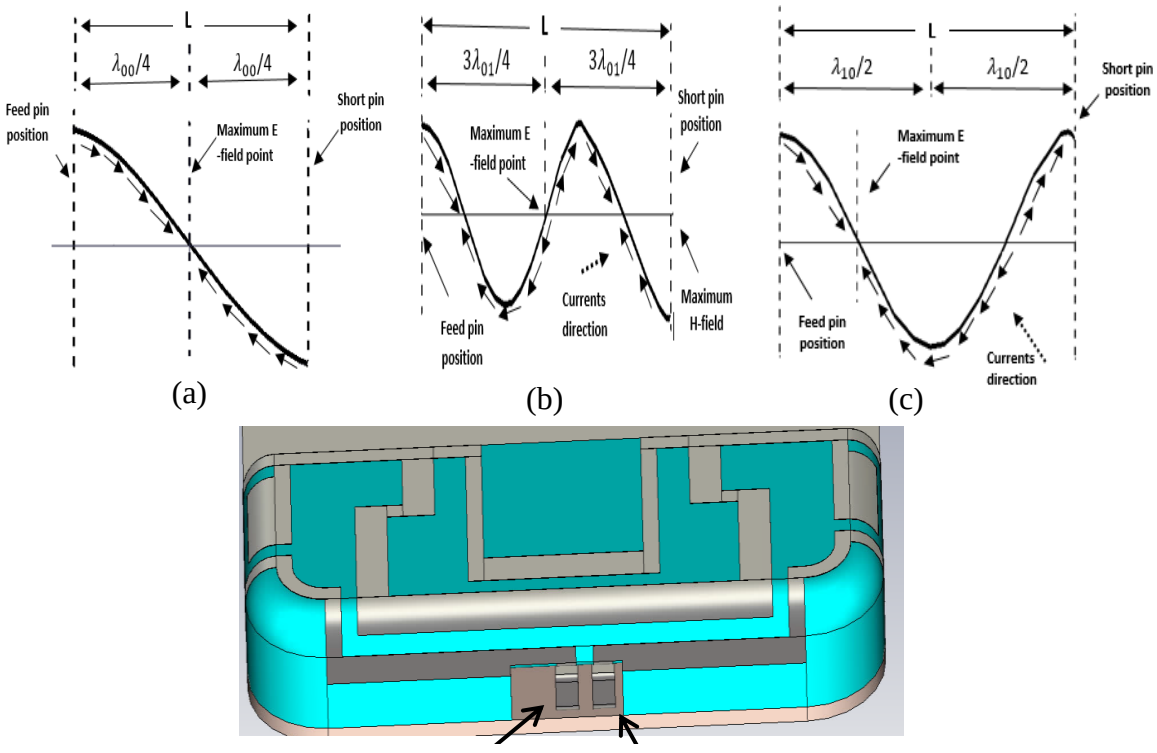

Figure 6-22: Dual-loop etched over plastic carrier [39], with current distributions (a): common mode 0.5λ for short and long loops,(b): long loop 1.5λ common mode,(c):1.0λ short loop differential mode.

In addition, it is possible to increase the bandwidth by using the dual-loop because the radiation resistance is stepped up and the reactance can be made to cancel in the balanced and unbalanced current modes. The mutual capacitance between the lines depends on the distance between them. Increasing the distance between two metal strips or decreasing the strip width in the meander line reduces the mutual coupling and the resonance frequency shifts down, as shown in Figure 6-23. The three resonance modes are: Single loop-short and Single loop-long and Dual-loop modes.

In the dual-loop antenna mode, the 0.5λ resonance of the short and the long branches overlap; the second resonance appears at 1.85 GHz and the third resonance at 2.0 GHz, producing a high-band bandwidth of about 235 MHz, which is suited for GSM and WCDMA bands.

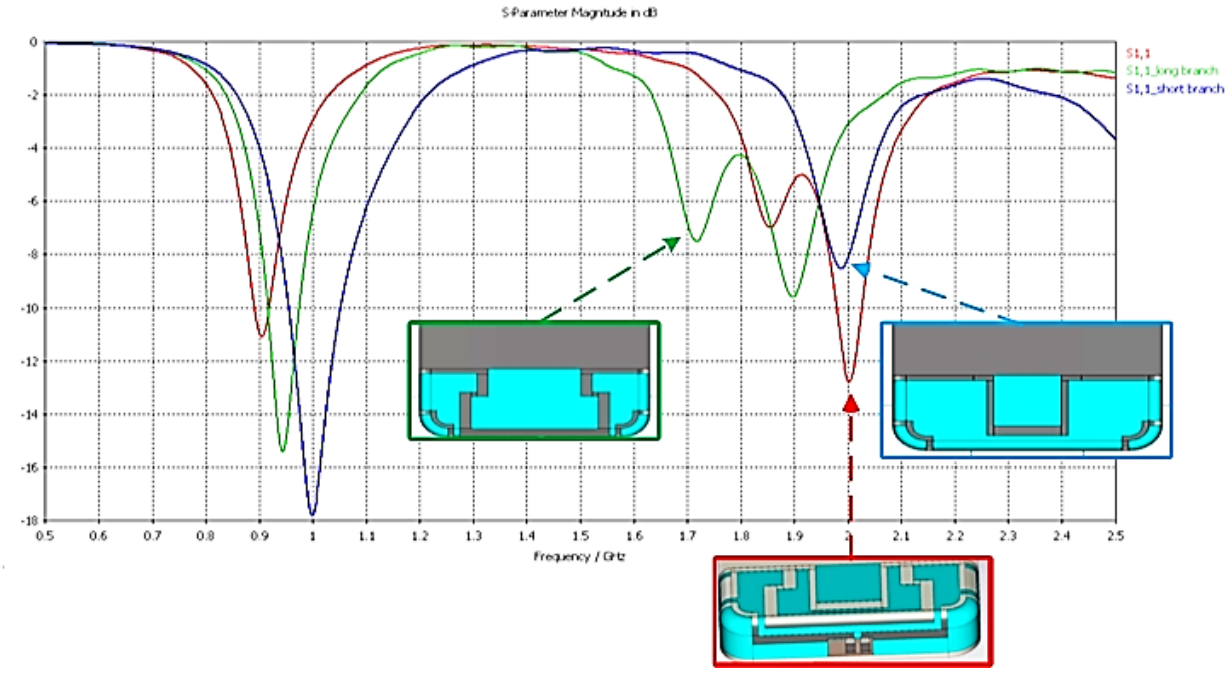

Figure 6-23: The reflection coefficient S11 of dual loop (red), S11 of single loop-long branch(green),S11 of single loop-short branch(blue).

In practice, when the handset antenna has bottom position, the PCB of the handset is closer to the user's head, which is an important factor in human head interaction and requires further investigation.

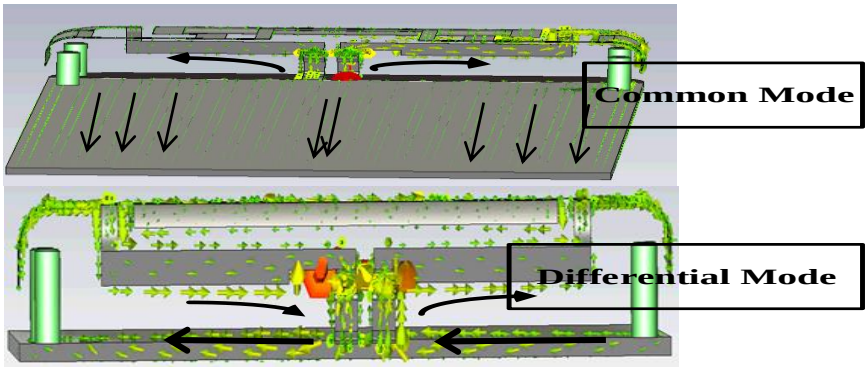

Figure 6-24: Simulated surface current distribution on the dual-loop antenna for common and differential modes.

Figure 6-24 shows the current flow on the antenna for the common mode excitation compared to the current on the chassis for the differential mode (balanced mode); the loop antenna is seen to be the main radiator in the mobile phone at the balanced mode, while in the common mode the PCB carries high current and considerably contributes to the fields, which is also seen from Figure 6-25.

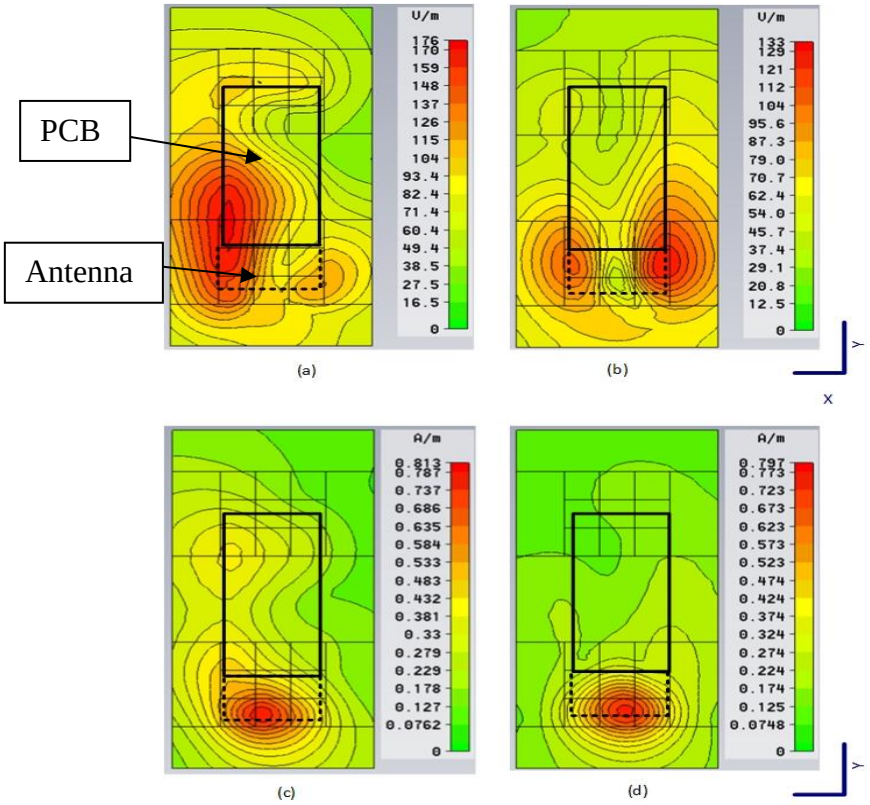

Figure 6-25: Simulated absolute E&H-field distributions in free space at Z=10mm level below the PCB. Common mode (1.85 GHz) (a): E-field (c): H-field. Differential mode (2 GHz), (b): E-field, (d): H-field.

Figure 6-25 shows the absolute E-and H-fields for the two modes in free space, where the absolute E-field is dominated by E_z in (a), and (b).

At 2 GHz, differential mode, the two current minima are causing two balanced E field maxima at the two sides of the loop (full wave mode), which shows similar functionality as a folded dipole. In addition, the current maximum produces an H field maximum at the middle of the loop's electric length.

For the measurement of a fabricated prototype antenna structure, the iSAR (2D SAR) was used to investigate the E-field and SAR values of common and different current modes. Figure 6-26 shows the fabricated structure, which is placed 10mm above the

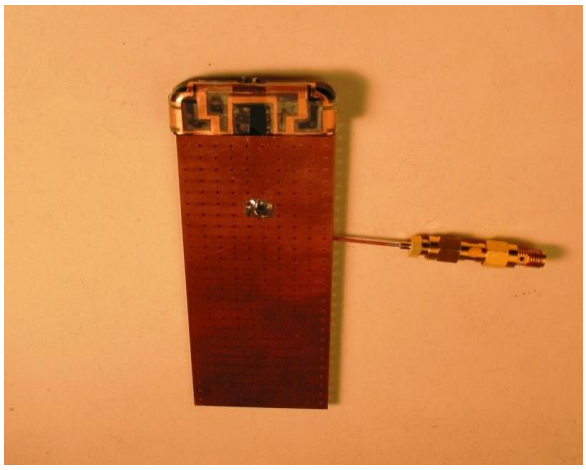

Figure 6-26: Dual-Loop prototype, PCB 80×40 mm, antenna is etched over the plastic carrier.

iSAR surface and is fed with 13dBm input power from a signal generator.

Figure 6-27 shows the E_y field distribution 4 mm underneath the surface of the phantom flat body (iSAR's Dielectric Block). Two symmetric electrical field concentrations are seen at the differential mode frequency of 2 GHz, similar to what can be expected from a folded dipole.

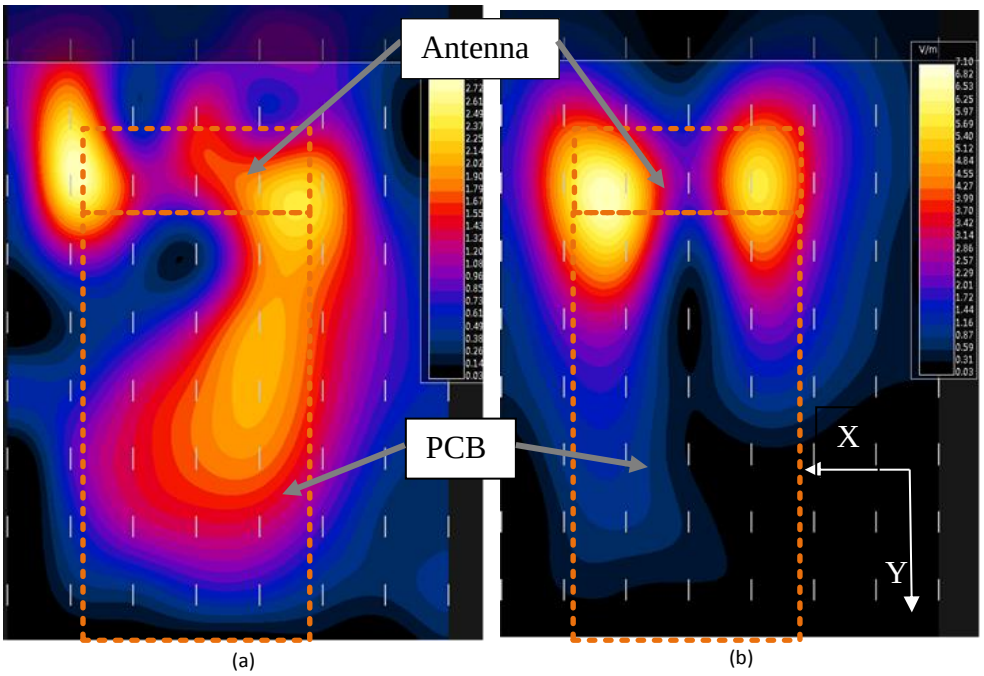

Figure 6-27: Y-component of E-field's distribution 4mm inside the phantom, P_{inc}=13dBm. (a) 1.85 GHz Common mode,(b) 2 GHz Differential mode.

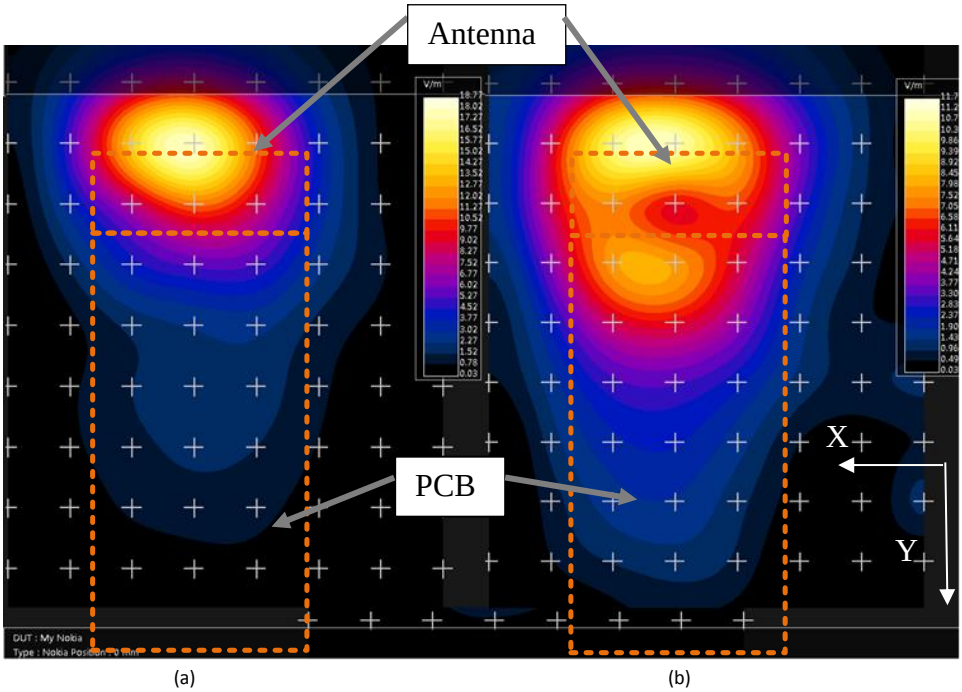

Figure 6-28: Measurement of the absolute value of total E-field 4mm inside the iSAR phantom, P_{inc}=13dBm. (a) 1.85 GHz, Common mode (left), (b) 2 GHz, Differential mode (right).

Figure 6-28 shows the total E-field distribution inside the phantom. Due to boundary conditions at the phantom surface, the tangential (X, Y) E-field is continuous and the normal (Z) E-field is highly reduced inside the phantom. The peak magnitude of the differential mode is lower by 37% compared to the field peak magnitude of the common mode.

The simulation of Figure 6-25 and the measurement of Figure 6-28 show the difference between the total E-field distribution in free space and inside the phantom. In free space the absolute value of E-field is dominated byE_z, while in measurement beside the phantom, the E-field inside the phantom is dominated by the tangential electric field E_x, due to the high permittivity.

Optimized antenna geometries that give the lowest SAR values for GSM 1900 were found by simulation and a prototype was manufactured. The SAR distributions of the prototype antenna at 1.85 GHz and 2 GHz are presented in Figure 6-29, with peak SAR (10g) of 0.47 mW/g and 0.19 mW/g respectively at P_{inc}=13dBm .

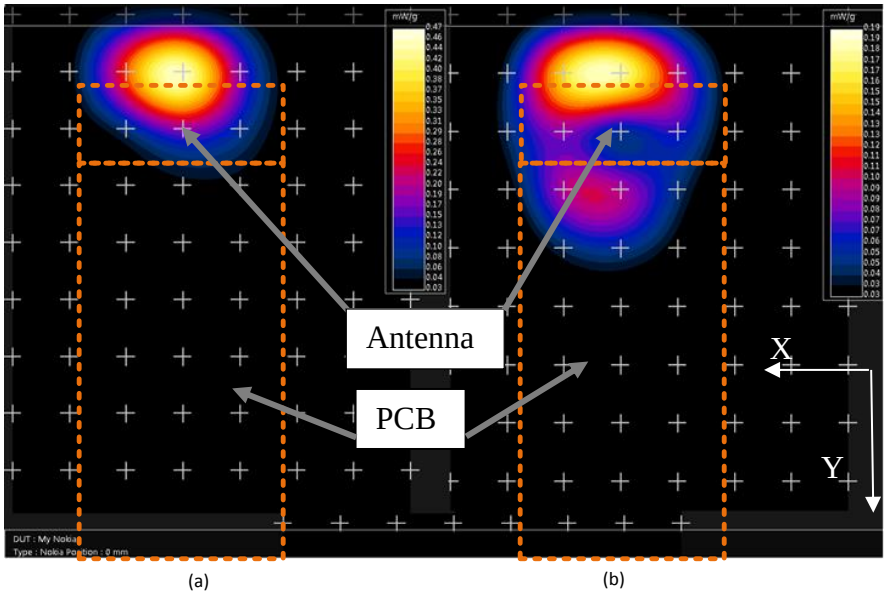

Figure 6-29: Measured SAR (10g) distributions of the prototype antenna 4mm inside the phantom, i.e., 14mm below the antenna, P_{inc}=13dBm. (a) Common mode, (b) differential mode.

6.3.2. RF Shields (Ferrite, Conductor, PMC)

Within the many studies on SAR compliance in the last decade, some studies inserted a reflector between the radiator and the head [40], [41].Other studies applied a ferrite sheet [42], [43] or other shielding materials [44], [45].

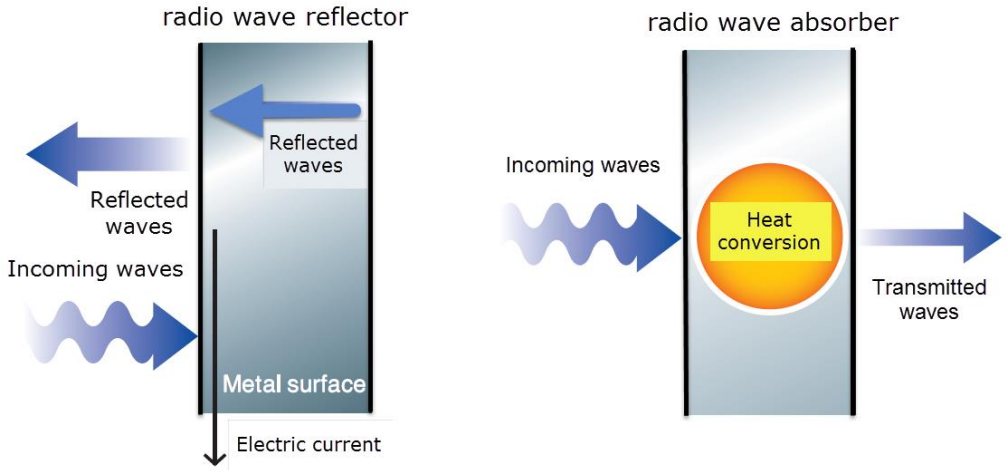

Figure 6-30: Concept of shielding material

Figure 6-30 shows the two main electromagnetic shielding concepts, the EM reflector and the EM absorber. The following section uses simulation and measurement to present an overview of SAR reduction by using reflection, absorption or dispersion of the radiation against the human body.

In the analysis, it is important to discriminate the components of the power that is delivered by the antenna.

The antenna output power can be separated into:

$$P_{\text{out}} = P_{\text{head}} + P_{\text{sch}} + P_{\text{rad}}$$

Where:

P_{head}: The power absorbed by the head

P_{sch}: The power dissipated in the RF shield

P_{rad}: The radiated power of the antenna.

A. Ferrite:

RF shields made of ferromagnetic material are used to suppress surface current on antennas with medical implantation [46]. This was the strong motive behind most of the studies.
Ferrite has been shown to offer potential for SAR reduction. Some low-SAR antenna designs have considered the use of a ferrite sheet behind the handset antenna to reduce the surface currents on the back of the PCB that cause electromagnetic fields directed to the user [42] [43]. SAR improvement by 40-57% was achieved, but the radiation efficiency of the antenna with ferrite was not considered .

The disadvantage of this technique as shown in [46] [47], is the high cost of material itself and the special properties of permittivity and permeability that the ferrite has to comply with in order to obtain low SAR. On the other hand, [42] reports the SAR value reduced by 88% compared to conventional phones and an efficiency of 38% at 1.8 GHz. Unfortunately, the radiation efficiency of the antenna installed on the mobile phone without phantom (in free space) was not considered.

Our own experimental investigation of a handset antenna backed by ferrite material was done with one commercial phone employing a PIFA-antenna. The ferrite sheet thickness t=0.25mm and relative magnetic permeability μ_r =15 at 1.88 GHz [48] is placed on the backside of the PCB.

Figure 6-31 shows the mobile phone with the PIFA antenna position and the ferrite sheet. The SAR (10g) distributions of the antenna at 1.88 GHz is displayed by iSAR with and without the ferrite sheet located between the antenna and the phantom.

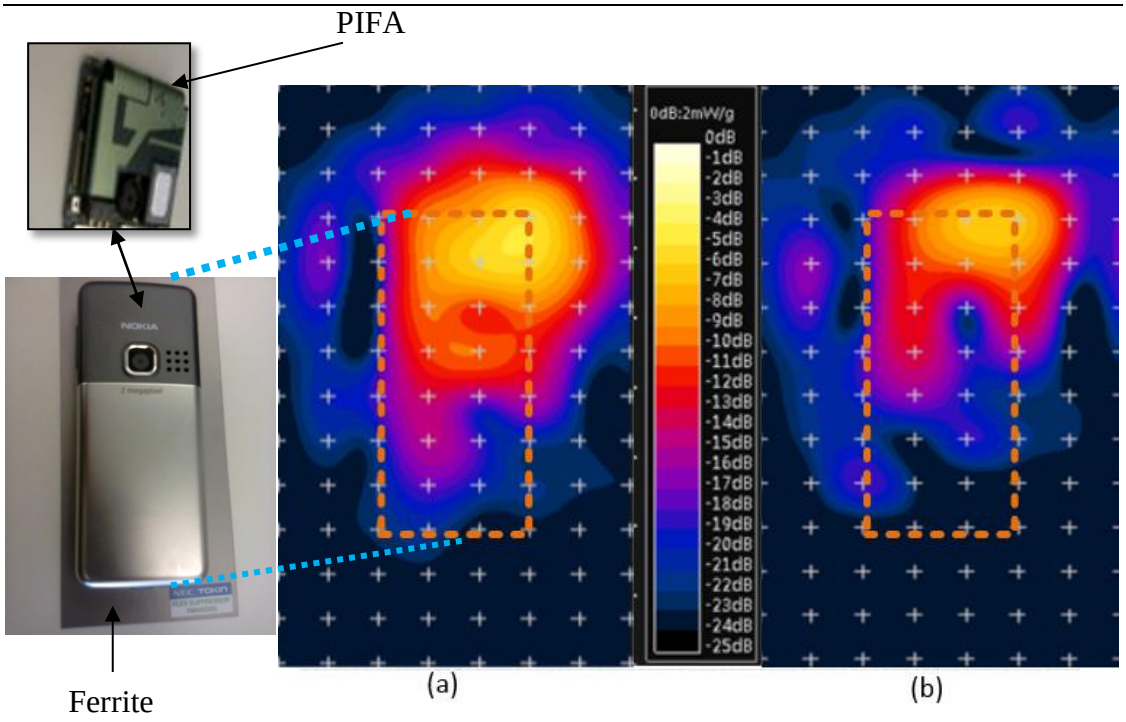

Figure 6-31 : Mobile phone and SAR distribution measurement 4 mm inside the iSAR phantom. P_{inc}=30dBm. SAR(10g) distribution for (a) antenna without Ferrite ,max. 0.33mW/g, (b) antenna with ferrite, max. 0.229mW/g.

From SAR and OTA investigations of this configuration, the ferrite can reduce SAR by about 30%, while the total radiated power (in free space) drops by about 41%, from 25.4dBm to 23.1dBm, due to absorption by the ferrite. Due to that power loss, the ferrite is not considered a viable solution for SAR reduction in mobile phones, where high radiation efficiency is one of the key antenna-design requirements.

B. Electric conductor as RF shield:

In section 6.2.1, the metal a parasitic element was connected to the ground plane of the PCB with two conductors. In this section, a metal sheet or Perfect Electrical Conductor (PEC) is investigated as EM reflector. Electrical conductors are used as EM reflectors in many applications, and are used in some SAR investigations [49] [50]. These recent investigations are based on simulation just for 900 MHz and without consideration of the antenna's radiation efficiency.

In order to study the effects on SAR reduction effectiveness due to PEC shielding material at 1900 MHz, a simulation was set up as shown in Figure 6-32.

A monopole antenna is mounted on the top of a PCB matching a frequency of 1.9 GHz. A Non-connected sheet of perfect electric conductor as RF shield is inserted below the antenna and PCB by 8 mm distance with dimensions of 46mm × X mm, X: is the variable length of the metal sheet. The metal model of the PCB of dimensions 46 × 100 mm with the monopole antenna is located at 18 mm above the phantom.

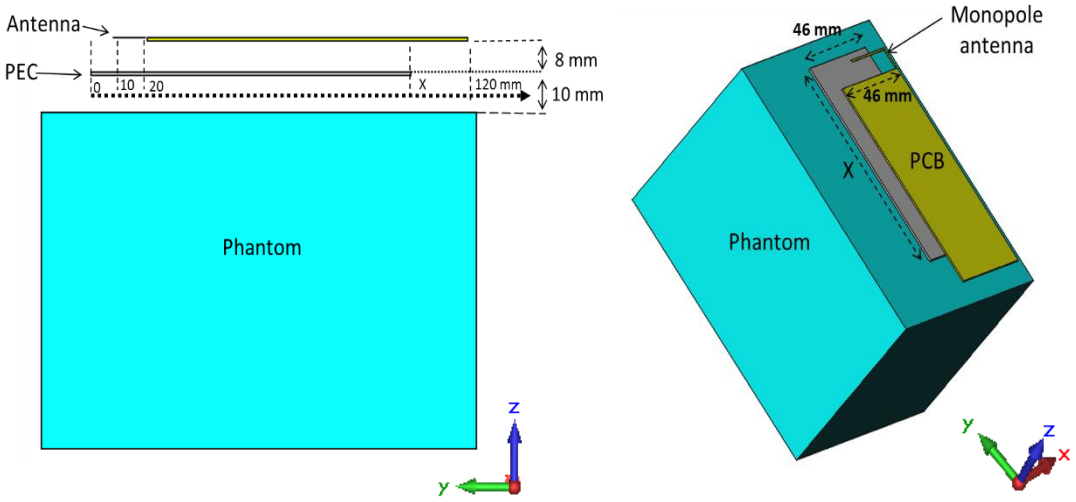

Figure 6-32: Simulation structure consisting of monopole antenna with the PCB (46×100 mm) and phantom with dielectric properties of head tissue-equivalent material, and PEC sheet (46 × X mm) as reflector.

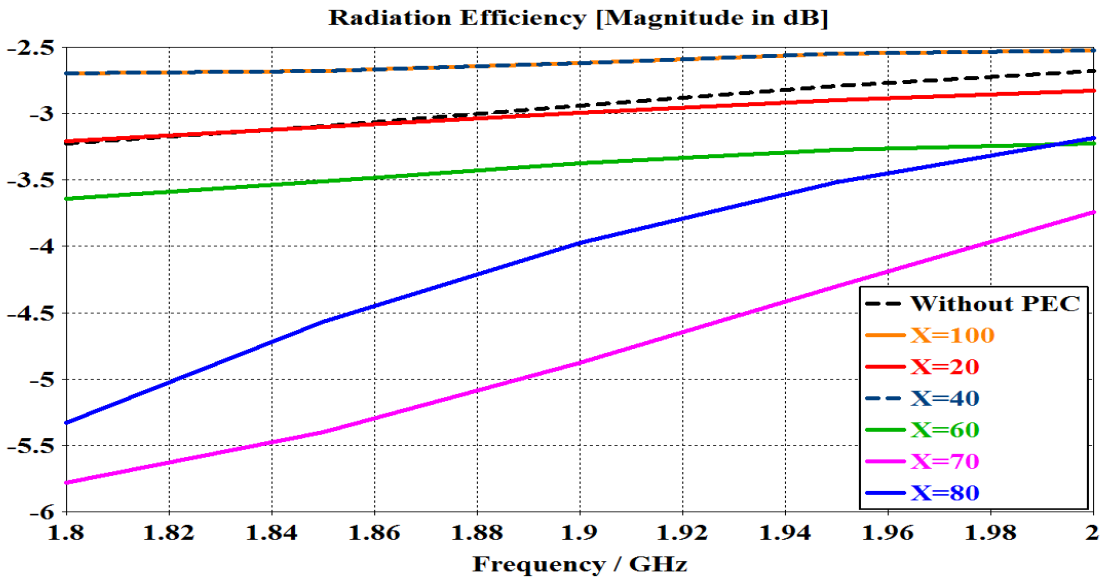

(a)

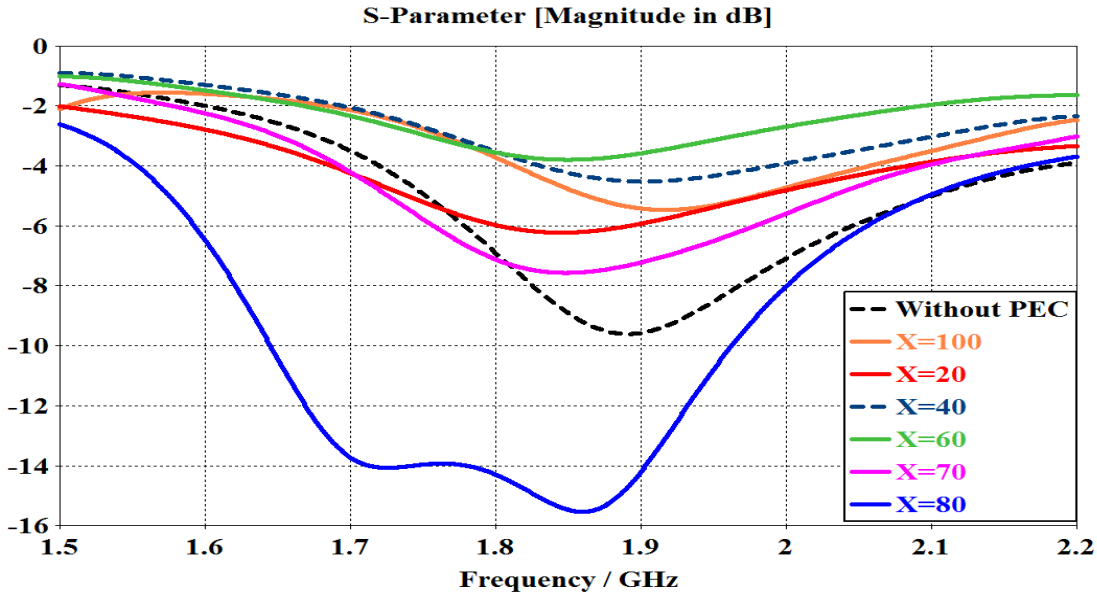

(b)

Figure 6-33: The antenna performance with variable PEC's length, (a) radiation efficiency, (b) reflection coefficient.

Figure 6-33 presents simulation results for the radiation efficiency and reflection coefficient of the monopole antenna as function of the length X of the PEC sheet.

It is seen in Figure 6-33(a) that the length X is a very critical parameter for radiation efficiency, leading to slight improvement for short (20mm-40mm) and long (100 mm) sheets and reducing efficiency for sheet sizes in-between. In particular, at X=70 mm we even see a degradation of 2 dB with respect to the case w/o a reflector sheet. The

two extreme cases are investigated in Figure 6-34 where the E-fields are plotted and the surface currents on the back (towards the phantom) of the PEC sheet are shown. It is obvious that the 70 mm sheet acts as a half-wavelength resonator with high field strength between the sheet and PCB as well as between the sheet and the phantom. The resonator wave length is seen to be much reduced with respect to free space due to high permittivity of the phantom dielectric.

With the closer coupling to the phantom than w/o the sheet more power is dissipated and the radiation efficiency drops. In contrast, the 40 mm sheet shows little surface current and moderate field intensities between the sheet and the phantom which can be attributed to the length X much less than the resonant length.

As a side-effect, the PEC sheet also detunes the monopole antenna, as seen in Figure 6-33(b), improving or degrading the match depending on length X. While this could affect total efficiency, matching of the antenna could be restored by modification of the matching network for any length X.

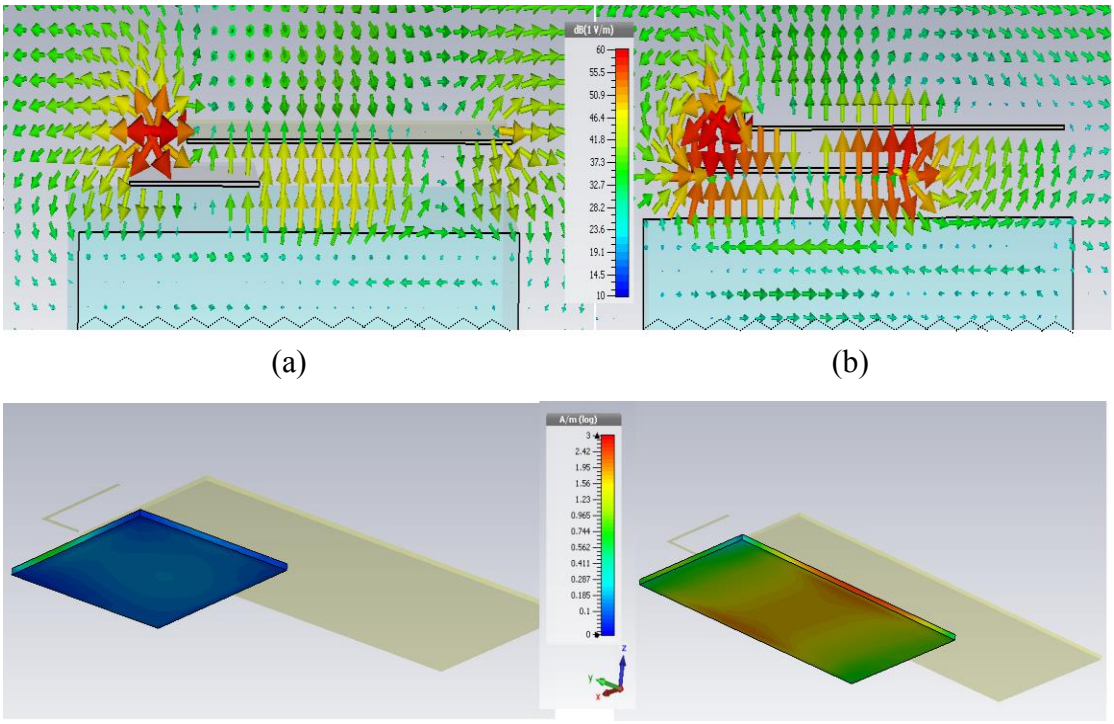

Figure 6-34: E-field and surface current distribution for metal sheet of (a),(c) 40 mm length (b),(d) 70 mm length.

The evaluation of the maximum SAR inside the phantom as a function of the sheet length is shown in Figure 6-35. Due to the high power loss into the phantom at the

resonant length of X= 70 mm, we observe a peak in the calculated peak SAR at 2.01 W/kg while the simulation scenario w/o PEC sheet gives only 1.08 W/kg. For smaller or larger PEC sheet with X much less or much more than the resonant length of 70 mm, the calculated peak SAR is found lower than w/o a PEC sheet. This indicates some potential of a metal reflector sheet as a SAR control concept. However, the metal sheet has the disadvantages of requiring extra space below the PCB and needing special design modifications to avoid lower total antenna efficiencies under special user conditions such as the location of the user fingers, and with respect to other relevant parts of the real handset, like the metal cover and the LCD. Never-the-less, the major reason why the metal reflector sheet has not been considered a viable approach for SAR control in mobile phones is the strict design rule in the industry to avoid non-grounded metal parts.

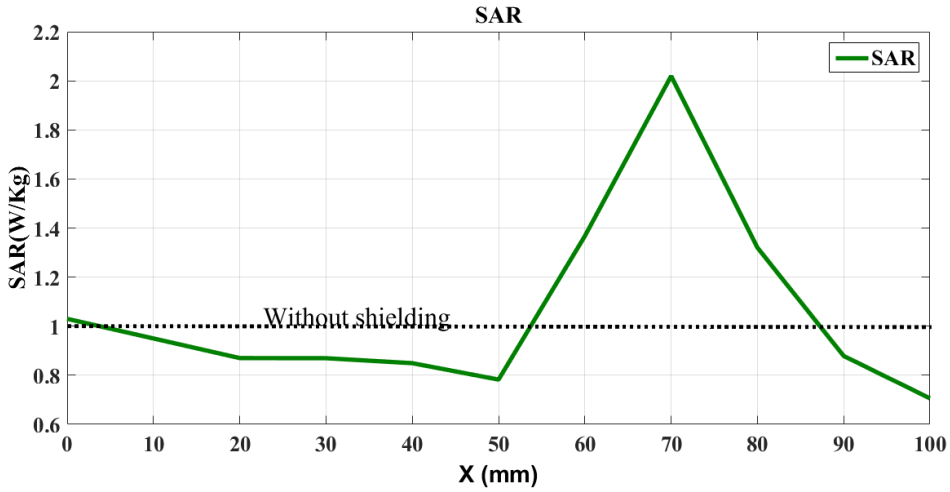

Figure 6-35: Peak SAR (10g) inside the phantom for the monopole antenna backed by PEC sheet as function of PEC's length, P_{inc}=0.25 W, peak SAR (10g) =1.08 W/kg for the antenna without shielding.

C. PMC:

Any metallic sheet as ground plane or reflector can partially shield objects located on the other side [16].When a monopole antenna is placed near to a metallic reflector, as shown in Figure 6-34, the antenna will radiate into free space and generate currents flowing on both sides of the metal sheet. The surface currents on the PEC generate an EM field between the PEC and the phantom, and because the metal sheet can be considered a dielectrically loaded transmission line (together with the phantom), SAR value is increased in the phantom and the antenna performance is degraded when the (metal sheet) transmission line becomes resonant at λ/2 length.

Therefore a new investigation is focusing on a new special material that can suppress the wave excitation below the shield. This material is the Perfect Magnetic Conductor (PMC), which can be approximated by a Metamaterial [51]. The PMC can be characterized by a vanishing tangential magnetic field at the surface and the boundary condition at the surface of such materials then becomes: $\vec{n} \times H_s = 0$.

Figure 6-36 shows the simulation structure of a monopole antenna backed by an RF shield of PEC material or of PMC material, which is modelled by a very high magnetic conductivity $6e^{30}$1/Sm and zero losses.

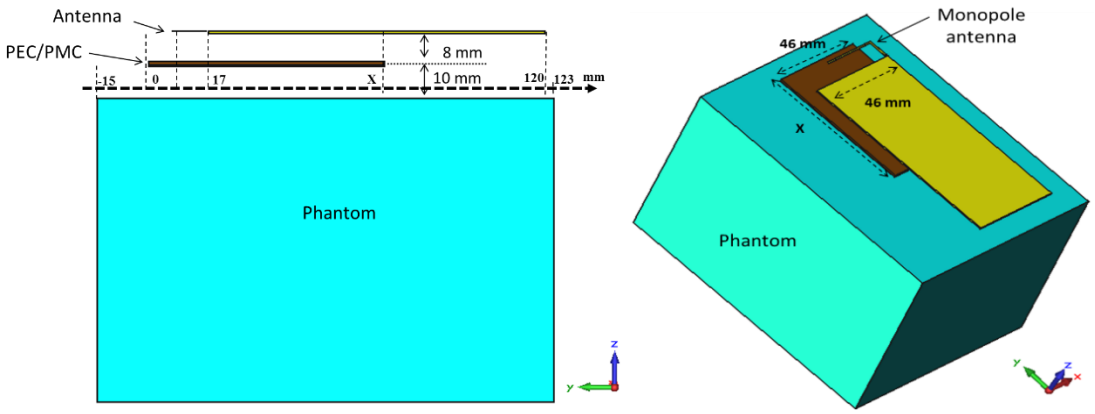

Figure 6-36: Simulation structure for monopole antenna backed by 1mm× 46mm×X mm PEC or PMC shield.

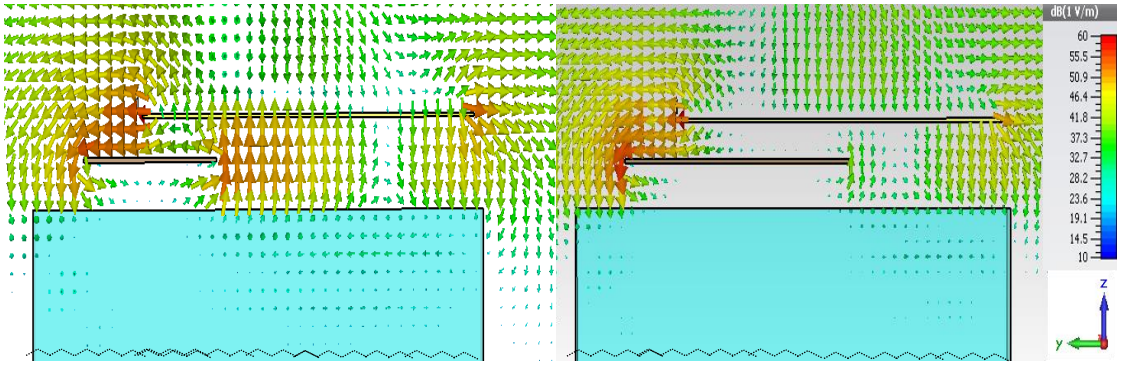

(a)

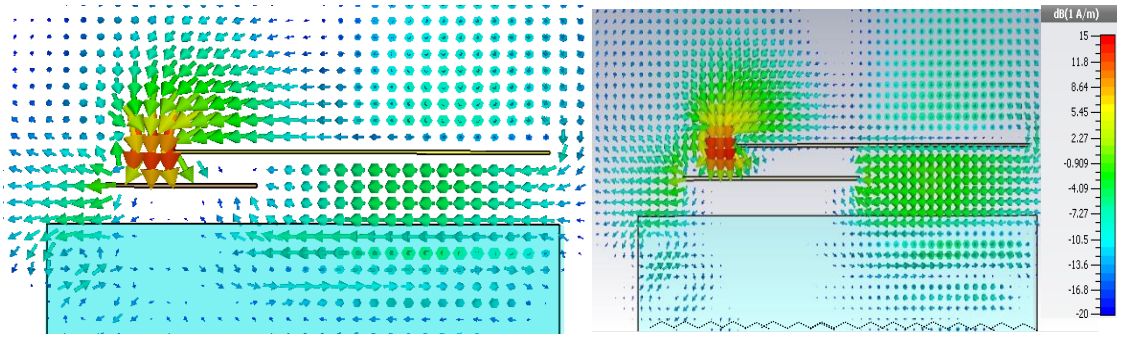

(b)

Figure 6-37: Simulated field distributions of monopole antenna backed by PMC with 40 mm and 70 mm length.(a) E-field,(b) H-field.

Figure 6-37 shows the E-&H-field distributions of the monopole antenna backed by a PMC sheet. The antenna is mounted on the PCB and placed above the phantom's body with 18mm distance and the sheet is placed 8mm below the antenna and PCB.

On the backside of the sheet the amplitude of E-&H-fields are found very small, proving the PMC as perfect reflector .The tangential H-field component at the PMC surface and the vertical E-field component are zero, combined with zero surface electric currents due to the boundary condition. However, still at the left corner (below the antenna) of the sheet we see strong field intensifies which generate a hotspot in the SAR distribution.

The radiation efficiency at the frequency band (1.8 - 2 GHz) with different RF shielding material 1 mm×46 mm×X mm at 8 mm below the monopole antenna is shown in Figure 6-38. Results for 40 mm and 70 mm show that the sheet length has negligible effect on the antenna performance and even the short reflector sheet improves radiation efficiency considerably.

With 70 mm PEC sheet's length and at the frequency 1.9 GHz, the antenna radiation efficiency is decreased by 2 dB while with PMC it is increased by 1.5 dB. In addition, peak SAR is improved from 1.08 to 0.58W/Kg.

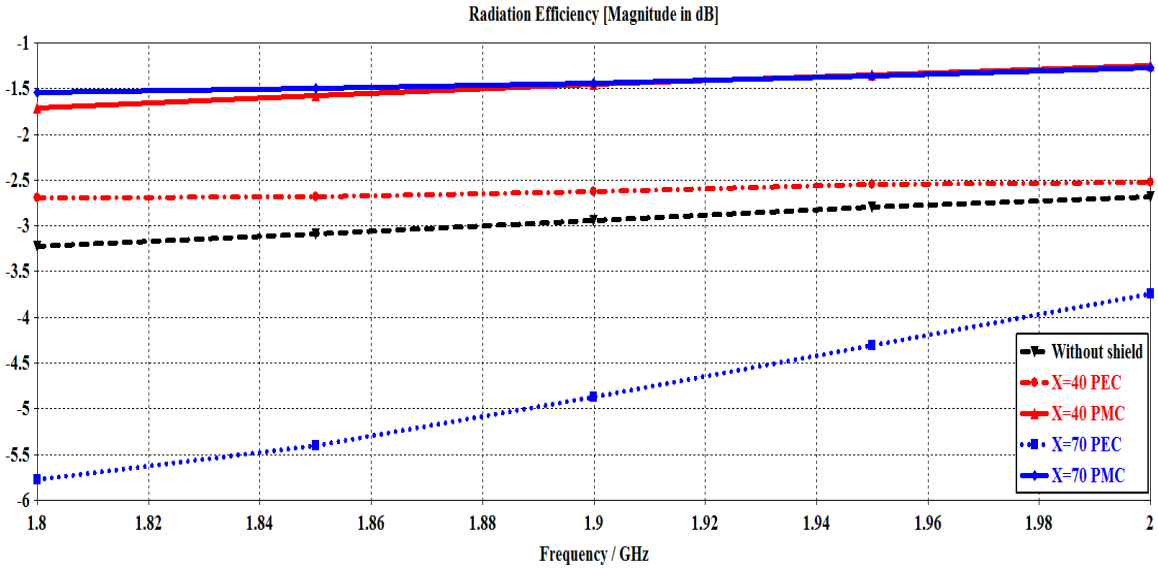

Figure 6-38: Efficiency of monopole antenna beside the phantom's body when it is backed by different RF shields at 8mm underneath of the antenna

This result indicates that the PMC is a promising candidate material for reduction of high peak SAR in mobile phones.

Since bulk PMC material is not available in nature, we have to turn to its metamaterial version of Artificial Magnetic Conductor (AMC) material. Before investigating realistic models of AMC in the form of Electromagnetic Band Gap (EBG) structures, a simplified model using a combination of PEC and PMC bulk material is investigated which comes close to the realistic EBG-structures: Most AMC structures use a PCB with a PEC ground plane and planar single-or multi-layered periodic patch/strip structures, some also with metallized vias. Such a structure is modelled by a mixed PEC/PMC structure shown in Figure 6-39. This model is used to investigate the fields and SAR properties when used as a shield below the antenna.

Figure 6-39: Mixed structure of PMC and PEC.

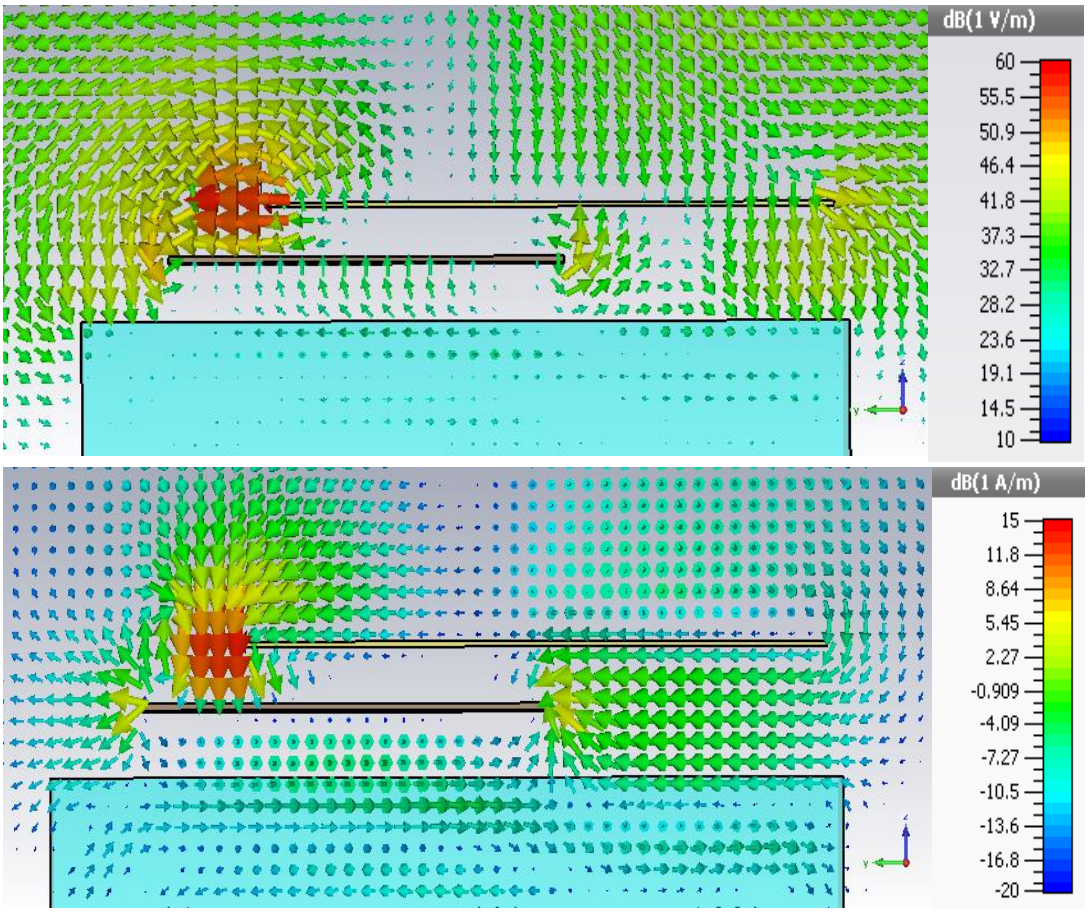

Figure 6-40: Simulated E-&H-field distributions of monopole antenna backed by mixed structure of 70 mm length. E-field (above), H-field (below).

The EM field distributions are shown in the Figure 6-40. Due to the PEC in the mixed structure, the normal component of the E-field and the tangential component of the H-field are generated on the bottom side, together with electrical surface current, however to a lesser extent and magnitude when compared to a pure PEC sheet.

With the mixed structure, the peak SAR (10g) value is less than with a pure PMC sheet as seen in Figure 6-41. Part of the radiated power causes a wave propagating between the PEC and the phantom, which increase the SAR value below the shield.

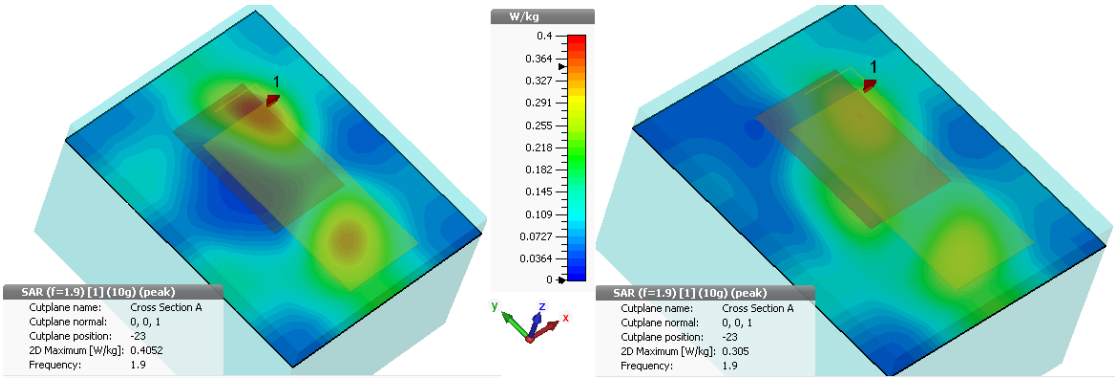

(a) (b)

Figure 6-41: SAR (10g) distribution at 5 mm below the phantom's surface, the antenna backed by (a) PMC peak SAR (10g) =0.4 W/kg, (b) PMC+PEC peak SAR (10g) =0.3 W/kg.

Chapter 7

7. EBG structures and application for SAR reduction

This chapter concentrates on EBG structures as a SAR reduction technique for GSM 1900. Max SAR location and SAR amplitude inside the phantom's head are investigated using a sample dipole antenna backed by an EBG ground plane as compared without EBG. In addition, the proposed EBG below real antennas in a mobile phone is investigated comparing the radiation efficiency and SAR when the antenna is backed by EBG ground plane to the case without EBG ground plane.

7.1. New potential concept: Electromagnetic Band Gap (EBG) structures

The electromagnetic properties of metamaterial have led to various terminologies found in the literature, such as: double negative (DNG) materials, left-handed (LH) materials, negative refractive index (NRI) materials, magneto dielectric material, soft and hard surfaces, high impedance surface (HIS), and artificial magnetic conductor (AMC). In the literature, also various terms are used based on the domain of the applications. In general, EBG structures are artificial periodic objects that prevent the propagation of electromagnetic waves in a specified band of frequency [52].

The basic characteristics of EBG-structures, the surface wave suppression band gap and the frequency band where the structure reflects vertically incident waves in-phase can be extracted from the dispersion diagram and the reflection coefficient plot over frequency, respectively.

In the recently published investigation [53] the EBG is proposed to protect the human body from the exposure of EM fields and to suppress the excited surface waves on the ground plane. In the examination done with a capacitive antenna element (PIFA) and with an EBG with vias and without vias as shown in Figure 7-1, the SAR (1g) measurement values are reduced by up to 75% when the PIFA antenna is backed by an EBG structure as compared with the PIFA backed by a metallic ground plane .

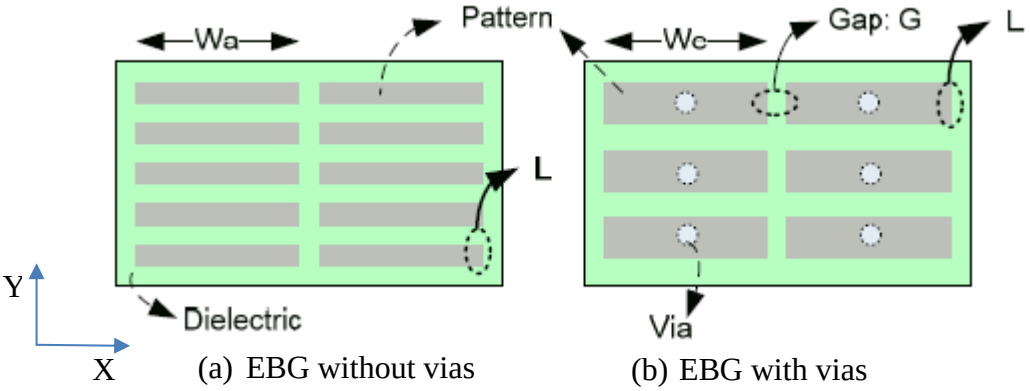

(a) EBG without vias (b) EBG with vias

Figure 7-1: Two types of the EBG structures, Wa= 20mm, L=3mm, We=19mm, from [53].

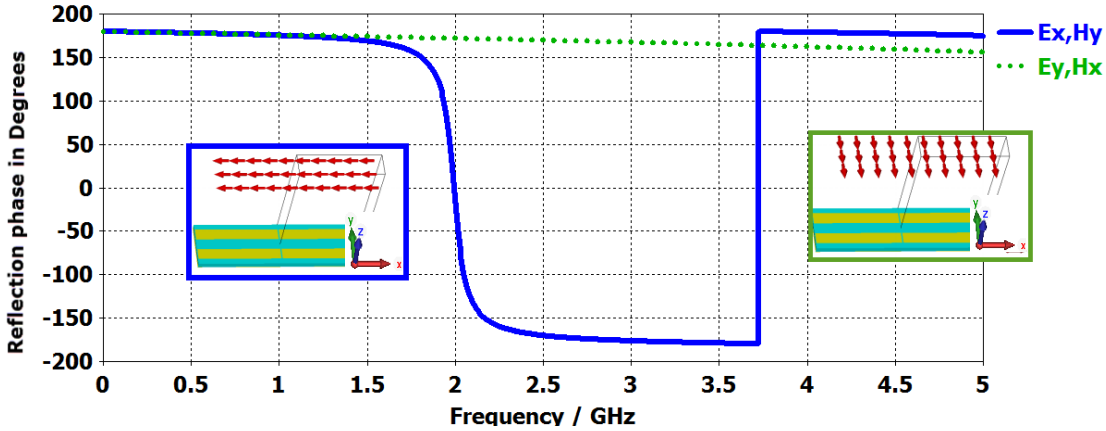

Figure 7-2: Plane wave reflection phase of EBG structures (without vias) for orthogonal-polarization cases.

In that study [53] , the EBG is fabricated using the Rogers Ro3010 laminate, which, however cannot fulfil the industry's mobile phone mechanical design requirements because it can break during the drop test. In addition, own simulations with two polarizations, see Figure 7-2, show polarisation dependence of the EBG reflection phase: If the antenna polarization is in X direction the EBG works around 2 GHz and only at very high frequencies with Y direction polarization. Therefore, a new stacked EBG is proposed in this section, and evaluated as solution for reducing SAR at the frequency band GSM1900 with actual mobile phone antennas concepts.

Figure 7-3 shows the geometry of the proposed stacked EBG cell for GSM 1900, where FR4 material is used as substrate. Optimized and smaller dimensions have been realized using the Eigen Mode solver simulation in CST and the Method of Moment solver in HFSS.

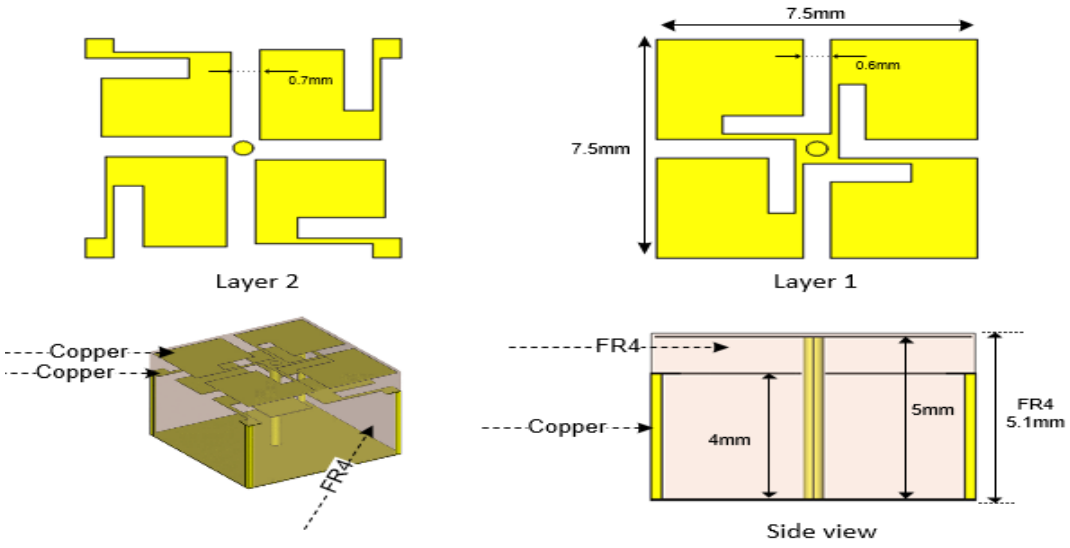

(a)

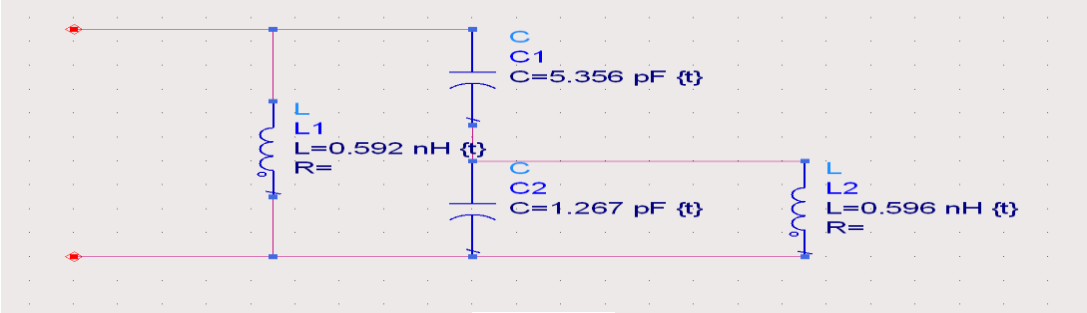

(b)

Figure 7-3: A planar stacked EBG which is investigated to reduce SAR at the frequency band GSM1900. (a) Geometry of one unit cell, (b) Equivalent circuit model for one unit cell.

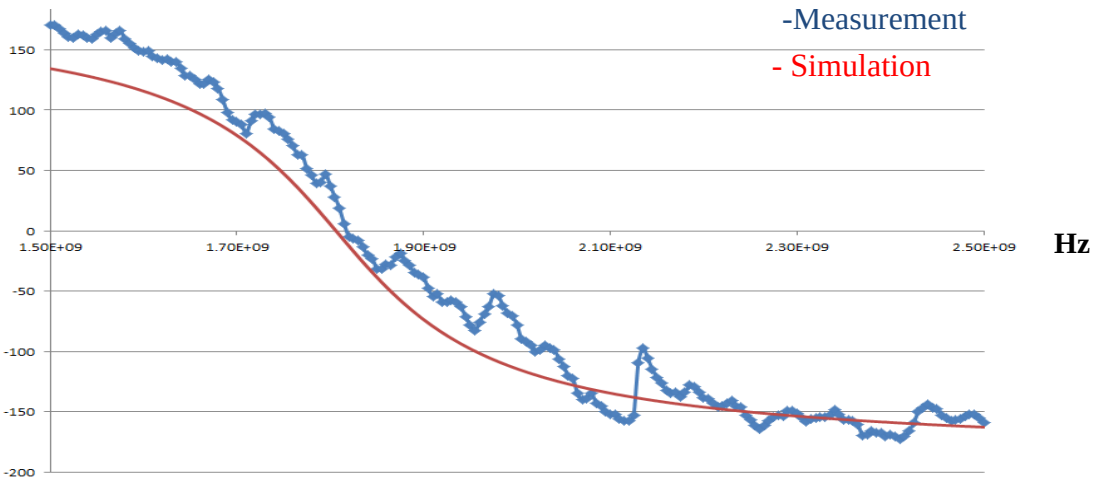

Figure 7-4 : The reflection phase for vertical plane wave incidence.

Figure 7-4 shows the EBG reflection phase from the measurement as shown in Figure 7-5: The reference measurement is taken of a surface with known reflection properties, a sheet of metal.

The metal surface is then removed and replaced by the surface under test (EBG) and the subsequent measurement is normalized to the reference. When performing phase measurements, the surface under test must be placed in exactly the same location as the reference metal surface, because variations in path length would create an additional phase shift.

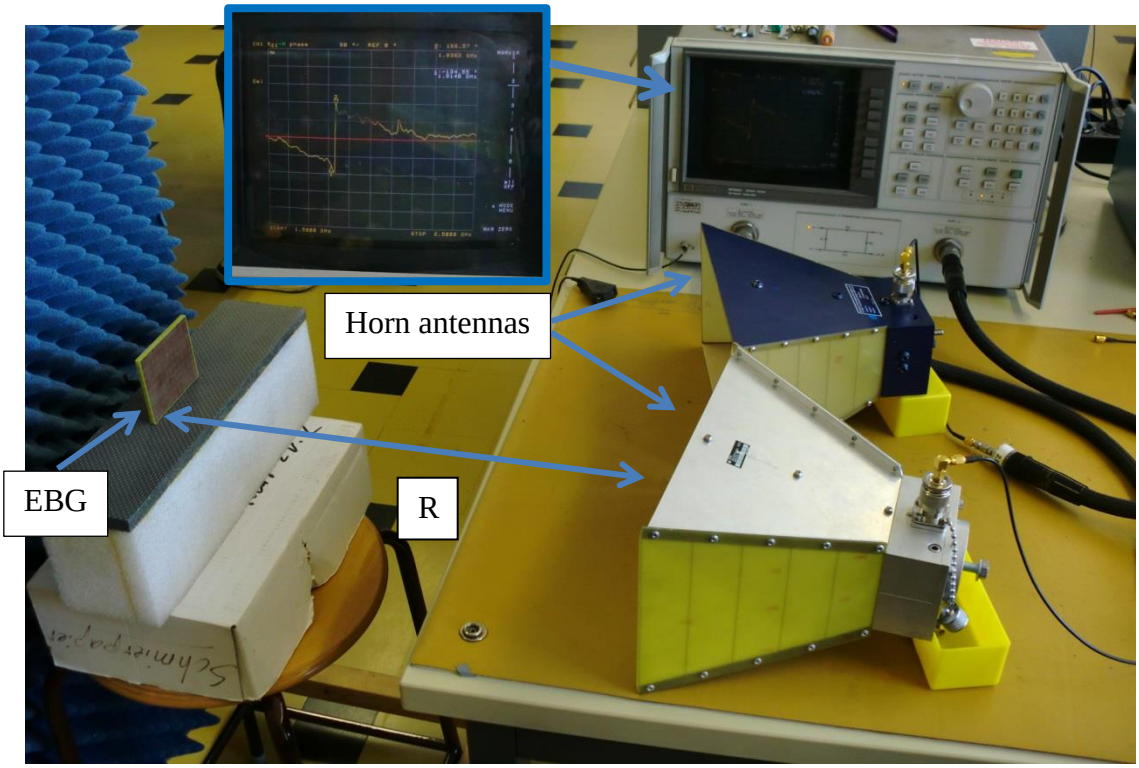

Figure 7-5: The EBG reflection phase measurement. Two vertical polarization horn antennas are used as receiver and transmitter.

A 180° is added to the phase data to account for the reference phase of the metal sheet, which is known to have a reflection phase of 180°.Since the assumption is that a plane wave is normally impinging on the surface of EBG, the distance between the horn antenna and the EBG's surface has to fulfill the far field condition.

The reflection phase, Figure 7-4 shows that the proposed EBG operates between the frequencies 1.74 and 2 GHz which includes it the GSM 1900 frequency band (1.86-1.92 GHz) .

In the next sections, the effect of the proposed stacked EBG structure close to a mobile antenna is investigated and the specific absorption rate SAR is compared to a mobile antenna without EBG.

7.2. Dipole antenna over EBG and PEC ground plane:

A monopole antenna over a PEC as RF shield was investigated in section 6.3.2 as SAR reducing solution, and the EM interaction was shown between the antenna and the nearby metal ground plane. In this section, we study a comparison of PEC and EBG ground planes with respect to the influence on the dipole antenna performance and SAR value, when the dipole antenna length is tuned to operate at frequency band 1.7 to 2.2 GHz; later, the monopole antenna with EBG is studied in next sections.

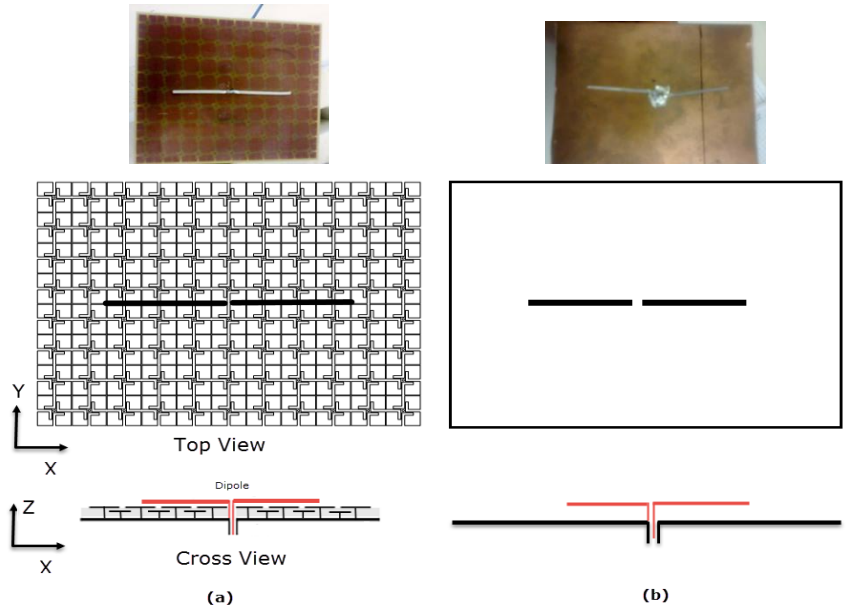

Figure 7-6: Dipole antenna over (a) EBG ground plane and (b) PEC ground plane. Dipole length= 60 mm, height= 6 mm above the PEC, ground plane size ($68\times83mm^2$).

Figure 7-7 is showing that the reflection coefficient is improved when the dipole is backed by the EBG ground plane; in addition, the antenna efficiency is linked to the reflection coefficient and it is improved when the antenna is backed by EBG as compared with the antenna backed by PEC. As was seen before in Figure 6-33, the length of the RF shield is a very critical parameter, which is limited by the size and the design of the mobile phones. Therefore, the EBG ground plane is investigated next

with smaller dimensions (number of unit cells) as RF shield inside the mobile phone to reduce the SAR in the user body.

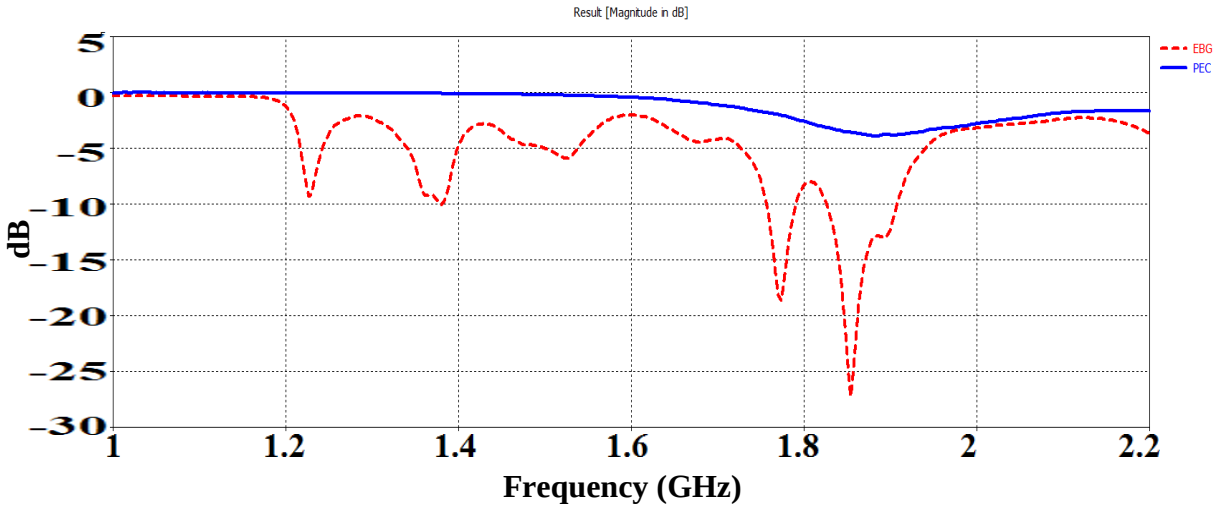

Figure 7-7: Measured reflection coefficient of the dipole antenna backed by EBG and PEC ground plane.

As soon as the electrical dimensions of the EBG structure become smaller than the wavelength the diffraction effect of bending waves around the edges of the ground plane become considerable. In addition, the hotspot positions below the body's surface move close to the maximum surface currents positions on the EBG's edges, and this could be one of the problems to use EBG in the SAR application. Due to this, the SAR value from an antenna over the EBG is investigated and compared to the case without EBG.

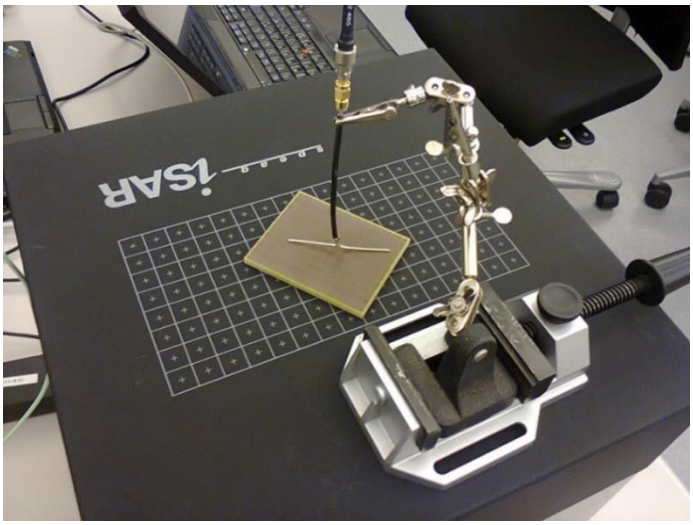

Figure 7-8: SAR measurement setup of the unbalanced dipole antenna above the EBG ground plane as RF radiator, dipole length= 60 mm,

To investigate the influence of the diffraction effect on the SAR value and peak SAR location, Figure 7-8 shows the SAR measurement setup using a dipole antenna touching the surface of the EBG which is at 5mm over the iSAR surface.

The reflection coefficient of the dipole antenna with EBG is compared to the case without EBG is shown in Figure 7-9.

The measurement shows a minor change in antenna matching. Therefor, with the EBG the antenna system still has efficient accepted power at the operating frequency range 1.86 to 1.92 GHz. Since the reflection coefficient < -6 dB, no modification of the matching network of the proposed antenna is required after implementing the EBG structure.

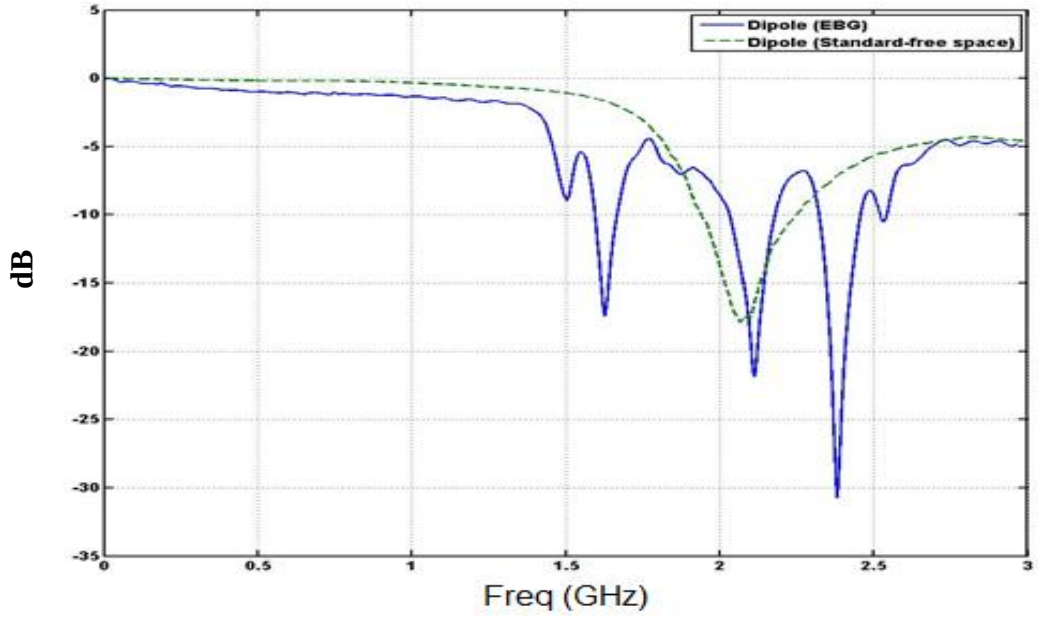

Figure 7-9 : Reflection coefficient of the dipole antenna on the surface of the EBG and for the dipole in free space.

Figure 7-10 shows that the EM wave from the antenna toward the EBG is exciting fields at the edges of the proposed EBG, which create a SAR distribution inside the phantom which shows hot spots close to EBG edges. Moreover, the SAR (10g) is decreased to 0.3 mW/g with EBG as compared to 3.18 mW/g without EBG.

Based on the last measurements, we may conclude that due to the wave diffraction on ground plane of the EBG, the SAR (10g) can be improved by using the EBG as RF shield between the antenna and the human head.

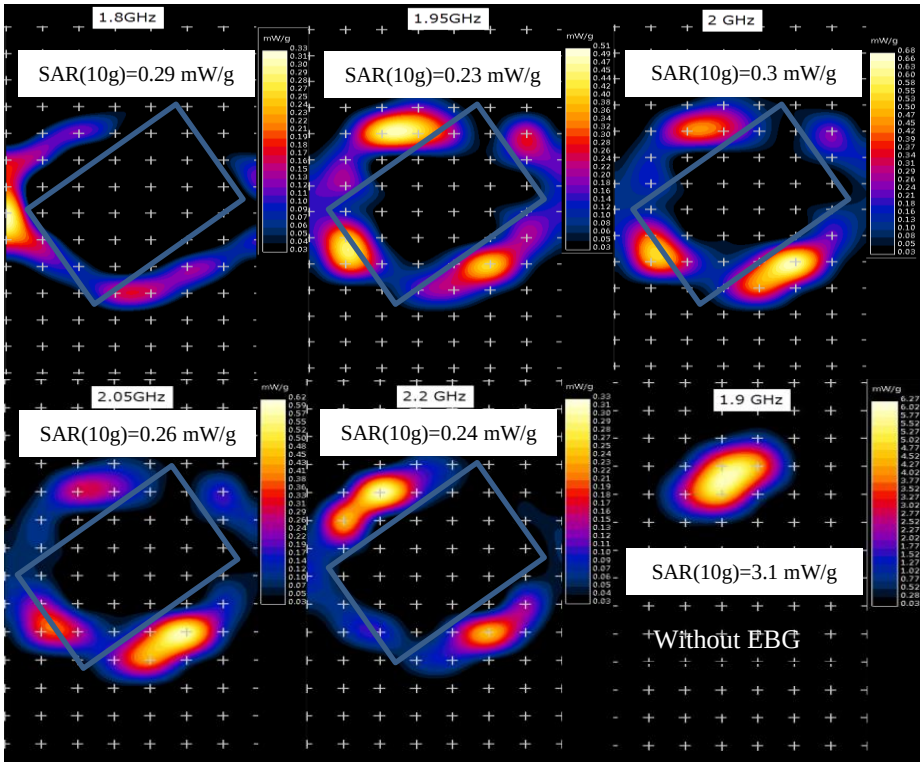

Figure 7-10: Hot spot locations and SAR values from dipole antenna over the EBG, P_{inc}= 23 dBm.

7.3. Mobile phone antennas over EBG and PEC ground planes:

The antenna models in this section are designed to operate at the frequency bands of GSM850, GSM900 and, GSM1900 such as the PIFA antenna. In addition to the PIFA antenna, other antenna types are also investigated such as the monopole antenna and the folded dipole antenna (Loop). These antennas have been widely used in recent commercial mobile phones to cover the WCDMA band.

7.3.1. PIFA antenna over the EBG ground plane:

The PIFA antenna is limited for its commercial use for mobile phones by narrow bandwidth. Therefore, it cannot be adopted for the frequency bands 3G. However, one of the main advantages of the PIFA antenna is its reduced backward radiation toward the user's head and hence, minimizing the electromagnetic wave power absorption (SAR) and enhancing the antenna performance.

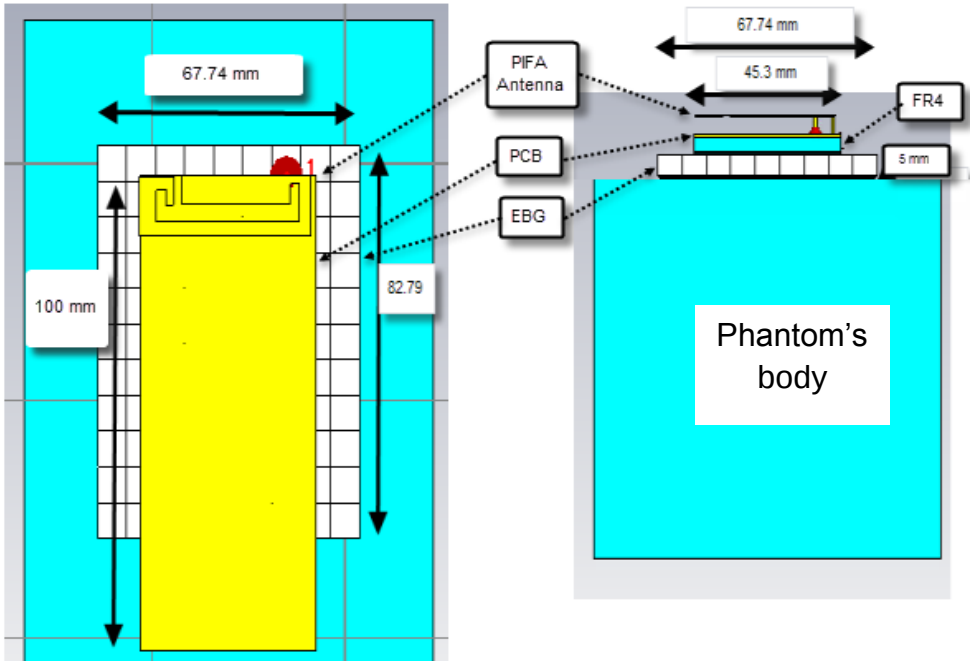

Figure 7-11 : Simulation structure of PIFA antenna on the PCB stacked by EBG structure (9×11 unit cells) as RF shield between the PCB and the phantom body. FR4 for the PCB with $\varepsilon_r = 4.9$, tanδ=0.025.

Figure 7-11 shows the PIFA antenna mounted on top of the PCB (46mm×100mm); the antenna shape is tuned to operate at the frequency band GSM 1900. From the simulation results in Figure 7-12 the antenna radiation efficiency beside the phantom is seen to be improved by 1dB by using the EBG. With the use of the EBG, the absorbed electromagnetic fields inside the phantom is decreased, as seen in Figure 7-13, and the radiation efficiency is improved; therefore the total efficiency is increased by 42%. In free space: we find no change in the radiation efficiency while the total antenna efficiency is increased with EBG due to the matching network used in the simulation model.

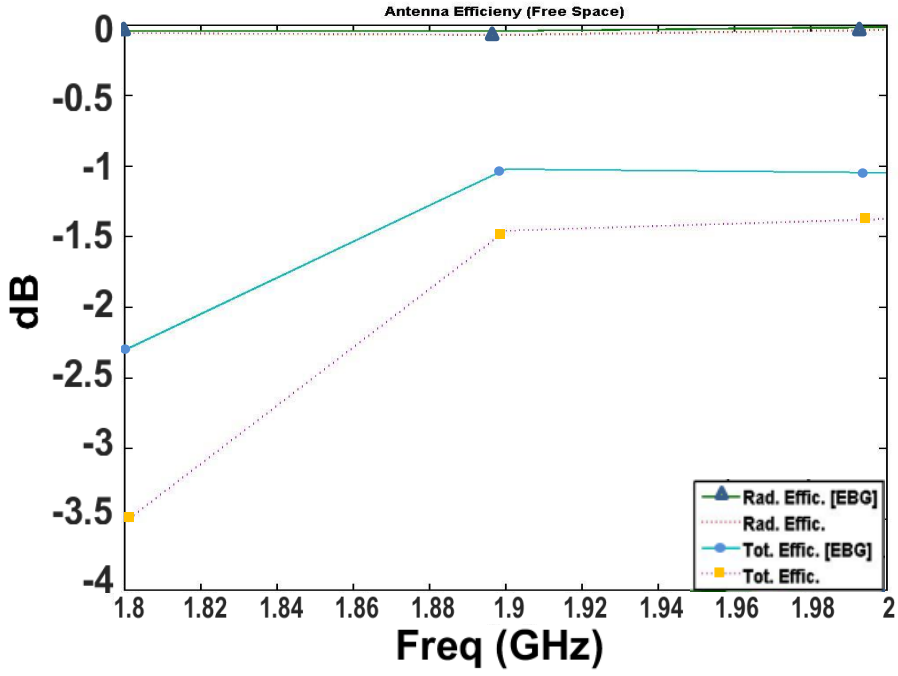

(a)

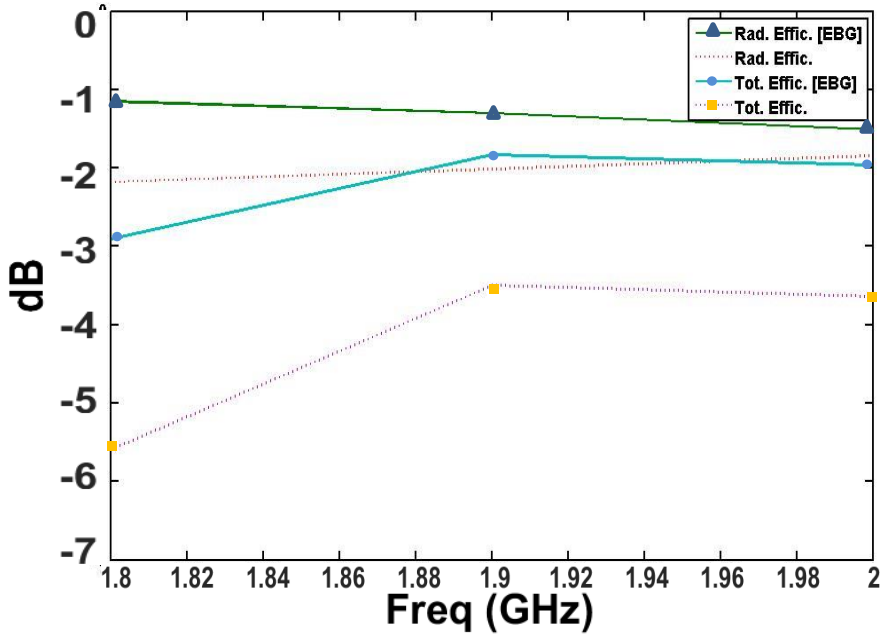

(b)

Figure 7-12: PIFA Antenna efficiency with and without the EBG below the PCB. (a) free space (without body), (b) with body.

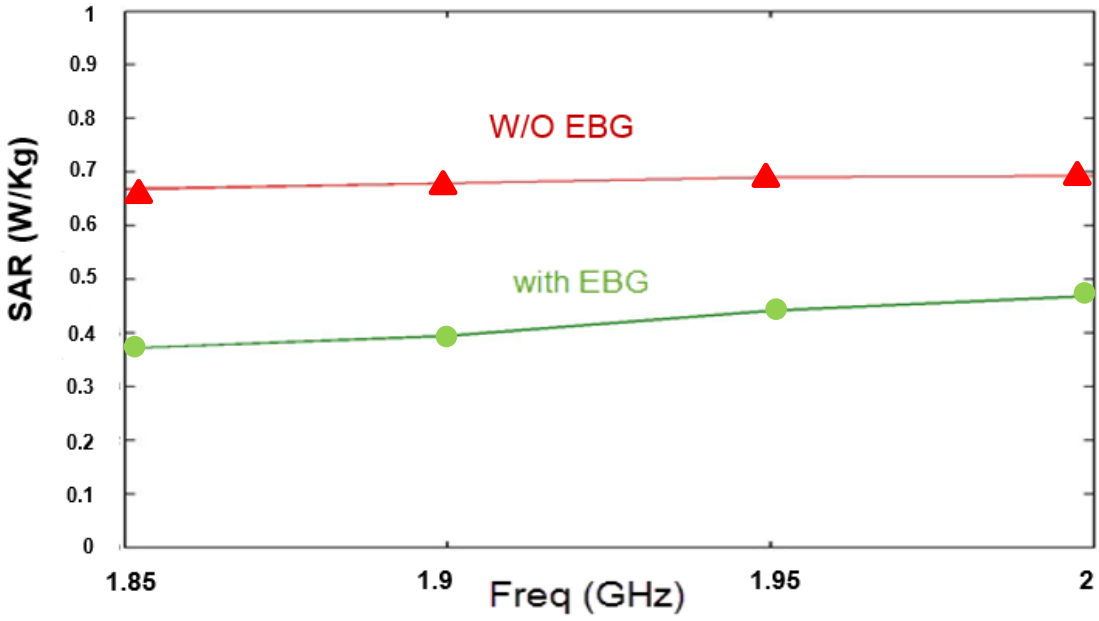

Figure 7-13 : Peak SAR (10g) value inside the phantom with P_{acc}= 0.25 W.

Results in Figure 7-13 show that if the EBG structure is inserted between the mobile and the phantom, then the Peak SAR (10g) is reduced by around 55%.

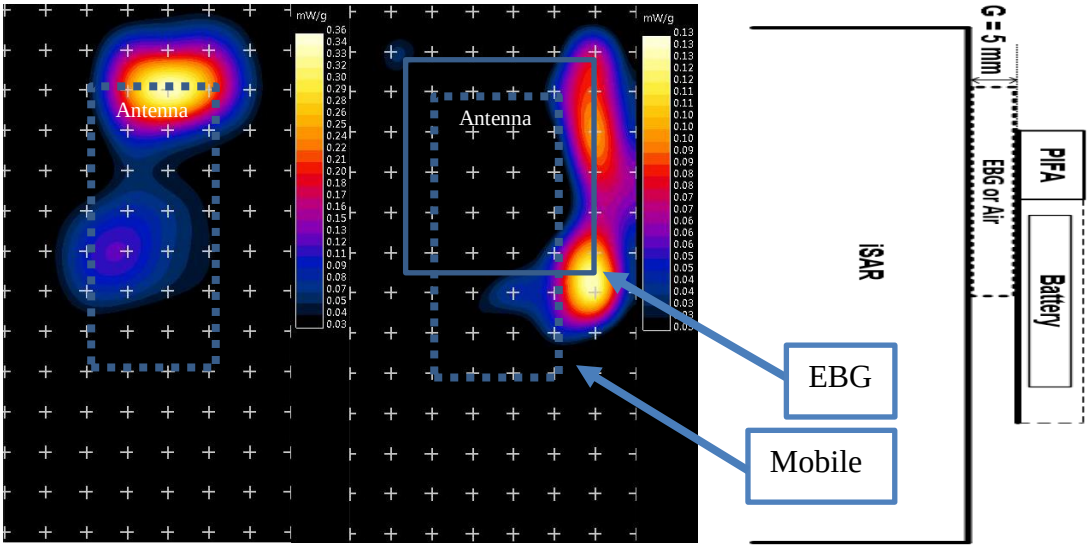

Figure 7-14: SAR measurement of commercial mobile at 1.88GHz and P_{inc}= 30dBm, with EBG (right) and without the EBG (left) inserted between the mobile and the phantom. Peak $\mathbf{SAR_{10g}}$=0.13W/kg (with EBG), peak $\mathbf{SAR_{10g}}$=0.36W/kg (without EBG).

A commercial mobile phone with PIFA antenna, as presented in chapter 6, Figure 6-

31, was used to experimentally investigate SAR levels inside the phantom when the EBG is implemented under the mobile.

Figure 7-14 shows that the EBG (9×11 unit cells) can reduce SAR by 65% from 0.36 W/kg without EBG to 0.13 W/kg when EBG is used as RF shield between the mobile phone and the phantom. The device under test is operated at the frequency band of GSM1900 and fed with output power=P_{inc}= 30dBm from the IC transmitter; the SAR measurements are done at the middle uplink channel of the frequency band GSM 1900, which is 1.88 GHz.

The SAR distribution measurements can be compared to the simulations presented in section 6.3.2 under headline C.PMC for the mixed structure of PMC and PEC to understand the distribution of SAR. The normal component of the E-field and the tangential component of the H-field generated on the bottom side as shown in Figure 6-40 excite surface waves on the backside of the EBG, which supports a wave propagating between the PEC and the phantom, as seen also in Figure 6.41, and which generates SAR below the shield.

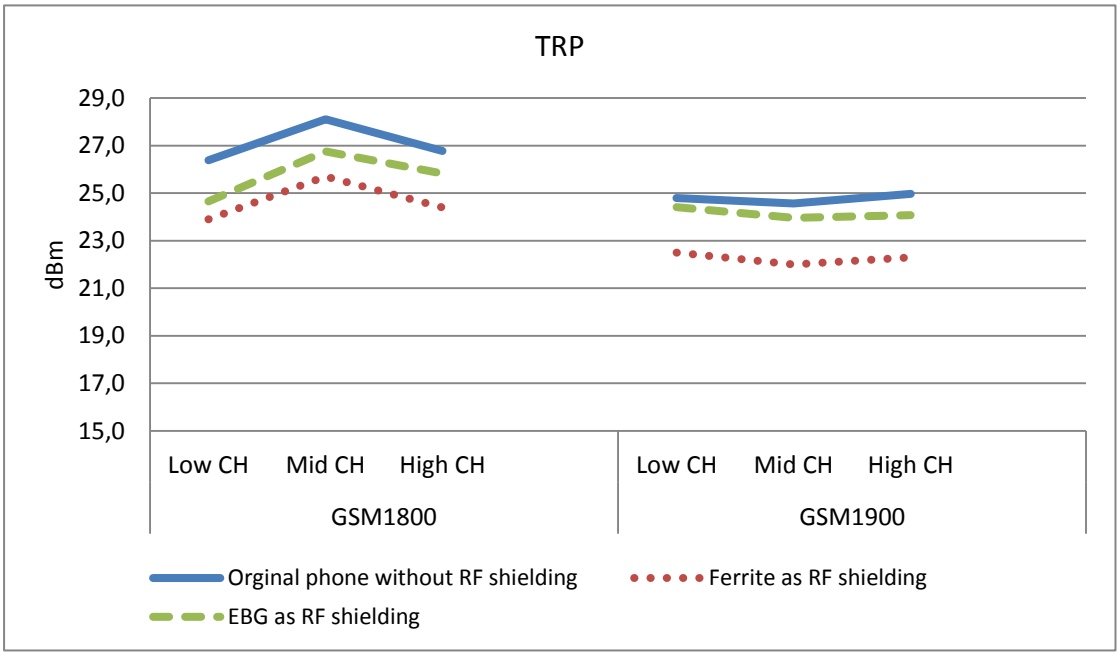

Figure 7-15: Measured Total Radiated Power (TRP) of the mobile phone with 30dBm transmitter's output power and with ferrite or EBG material as RF shield measured in free space (without head).

A check of the total radiated power in free space using the OTA measurement, Figure 2-5, shows that with the EBG, the total radiated power is reduced by a maximum of 13% at the EBG frequency band (GSM 1900) and 33% outside the EBG frequency

band (GSM 1800) ,which is less degradation than when ferrite material is used as RF shield in free space, see Figure 7-15.

As a conclusion, it is found that the use of an EBG below a PIFA antenna leads to SAR reduction by 55% inside the phantom while the total radiated power in free space is reduced by 15%, possibility due to miss-match of the antenna and/or due to dissipation loss in the EBG structure.

7.3.2. Dual-Loop Antenna over the EBG ground plane:

The commercial demand for multisystem handset equipment has recently increased rapidly. Therefore, the antenna in the smart phone must be capable of operating at four or more frequency bands. In this section the commercial mobile phone with dual-loop antenna and multiband characteristics, presented in section 6.3.1.is investigated with the EBG below its PCB.

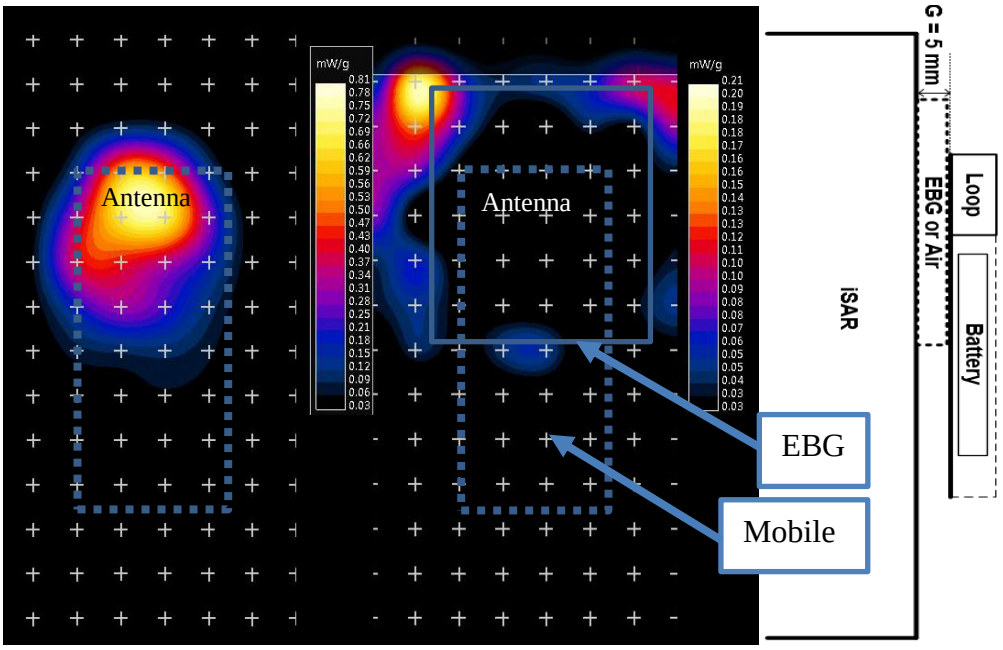

Figure 7-16 : Measurement of SAR distribution at 1.88GHz for a commercial phone with loop antenna at P_{inc}= 30dBm. Without EBG (left) peak $\mathbf{SAR_{10g}}$=0.81 mW/g, with EBG (right) peak $\mathbf{SAR_{10g}}$=0.21 mW/g.

This dual-loop antenna with EBG is investigated to study the effect of the electromagnetic band gap EBG on the loop antenna radiation efficiency and SAR

distribution inside the phantom body. Figure 7-16 shows that the maximum SAR value is decreased by about 74% at 1.88 GHz.

Figure 7-17 shows the TRP measurement values of the mobile phone with and without using the EBG as RF shield in free space case , at the GSM 1800 and GSM 1900 frequency bands with feeding power P_{inc}=30 dBm . The radiated power without shielding is between 25.6 and 27.2 dBm and with EBG is between 22.5 and 25.5 dBm.

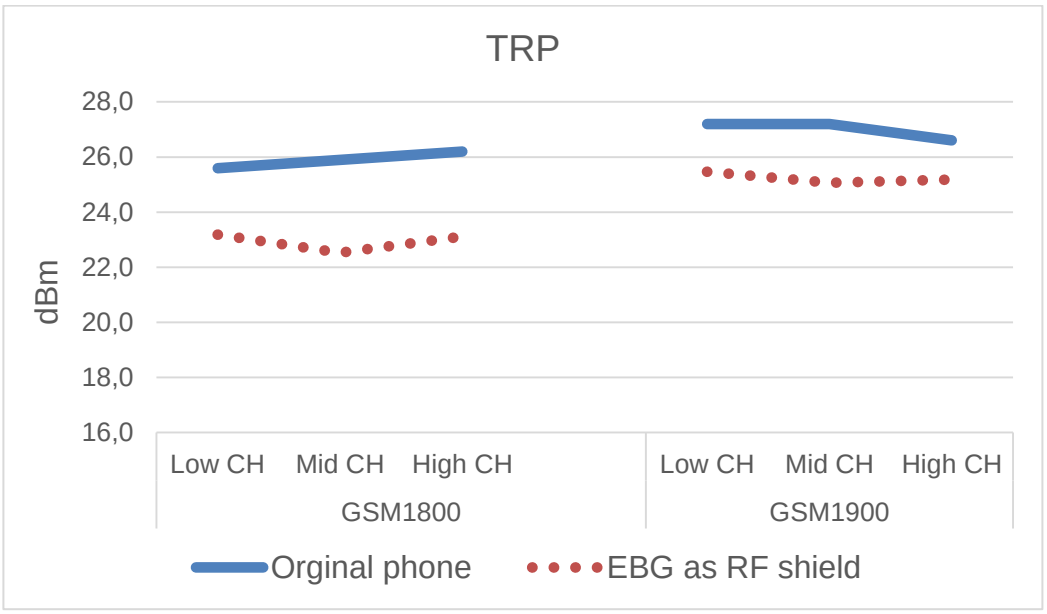

Figure 7-17 : TRP for commercial mobile phone with loop antenna at 30dBm Tx power and using the EBG as RF shield in free space (without phantom).

The TRP measurement is showing that the efficiency of the antenna is decreased in the out of phase frequency band (GSM1800) more than the in-phase EBG frequency band (GSM 1900). From the measurement, it is found that, by using EBG below the dual-loop antenna the maximum SAR value is decreased by about 74% with losses in the total radiation power in free space situation by 2.1 dB (around 37%) at 1.88 GHz.

However, from the TRP measurement, it is not possible to decide whether the losses in the antenna radiated power are due to the antenna's miss-match or the dissipation loss in the EBG.

From the results for the two antenna types, it can be concluded that the EBG (9×11 unit cells) can reduce SAR in the phantom considerably and it may be assumed that such improvement should be realizable with other antenna types also.

In the next section, a reduced size of the EBG structure with 2×6 unit cells ($5.1\times15\times45 mm^3$) is investigated with real mobile phone size and placed directly below the antenna.

7.4. Mobile Phone Antennas with integrated EBG structure:

In this section, a quarter-lambda monopole antenna is placed horizontally on the plastic carrier without metal ground underneath. Then, the stacked EBG (2×6 unit cells) of $5.1\times15\times45 mm^3$ is inserted below the antenna. The antenna performance and SAR were simulated and measured.

Figure 7-18 shows the proposed structure of a monopole antenna as high-band radiator mounted on a copper PCB 95×60 mm. The antenna length is tuned to work at the frequency band GSM1900.The distance between the radiator and the surface of the EBG is significantly reduced to 2 mm.

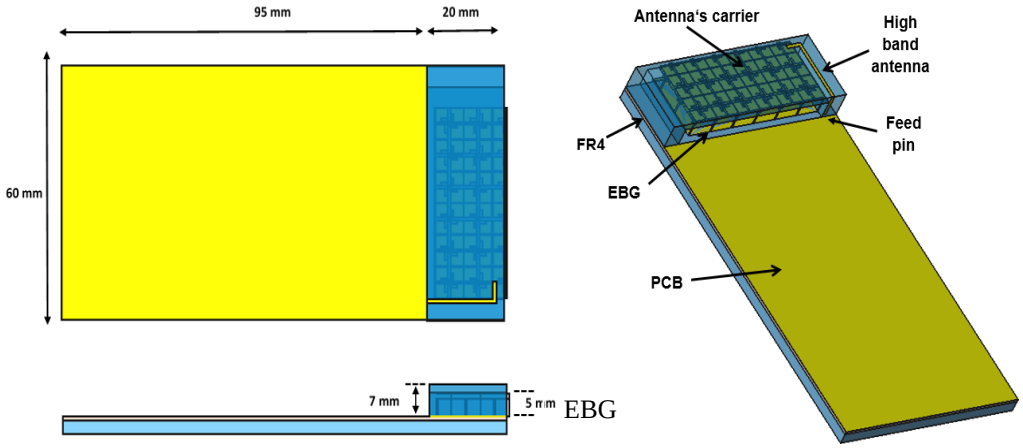

Figure 7-18 : Monopole antenna mounted on the top position of the PCB with plastic carrier, and EBG (2×6 unit cells). FR4 for the PCB with $\varepsilon_r = 4.9$, tanδ=0.025,antenna carrier (ε_r=3, tanδ=0.02).

The mobile phone in investigated for two conditions:

- Free space (without the head) or in "stand by" position: the results are represented in section 7.4.1.
- Beside the head "talking" position: the results are represented in section 7.4.2.

7.4.1. Antenna in free space:

The antenna performance is studied without the phantom head to disclose the influence of the EBG on the antenna performance in free space.

The distribution of surface current density on the PCB is shown in Figure 7-19. For the standard scenario (a) without EBG the surface current distribution is forming a half-wavelength chassis mode as shown before in chapter 5. The currents are spreading at the edges of the PCB and the maximum amplitude is close to the antenna feed point. With the EBG structure located below the antenna (b), due to the characteristics of the EBG structure a high surface impedance point is formed on the PCB close to the EBG that reshapes the current distribution on the PCB.

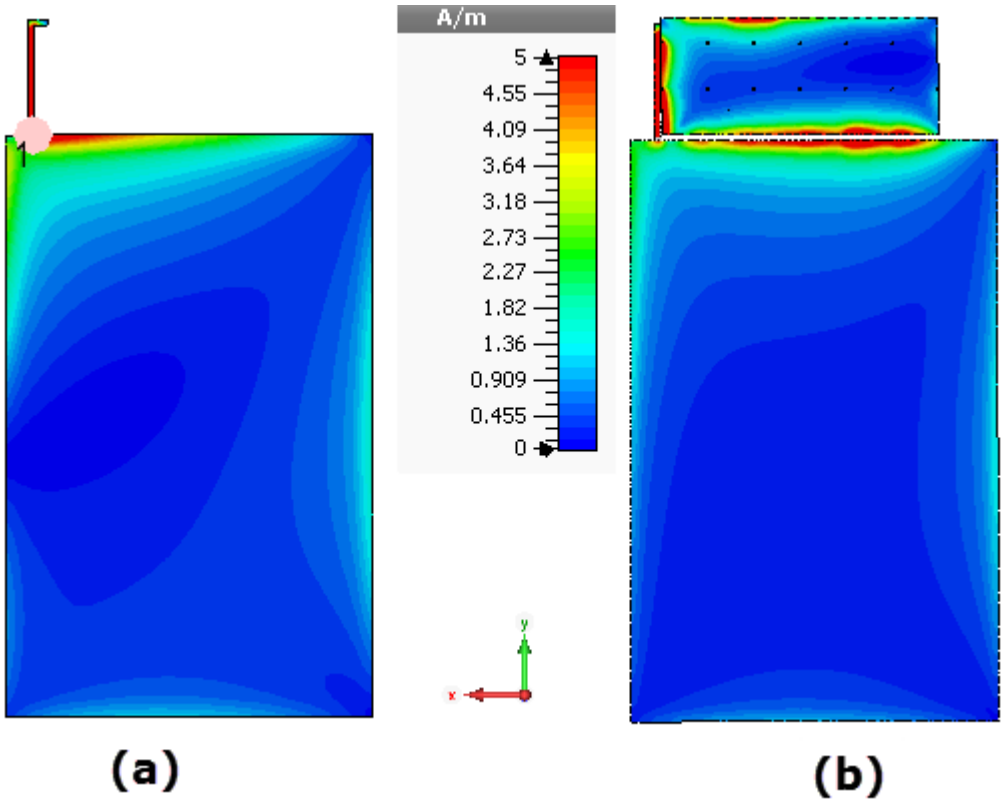

Figure 7-19: Surface current distribution on the back side of the PCB in free space at 1.9 GHz. (a) without shield,(b) with 2×6 unit cells EBG below the antenna, P_{inc}=1W.

The EBG reduces the operating bands width of the antenna when compared with the antenna not backed by EBG; Figure 7-20 shows the simulation of the radiation efficiency and reflection coefficient for both cases.

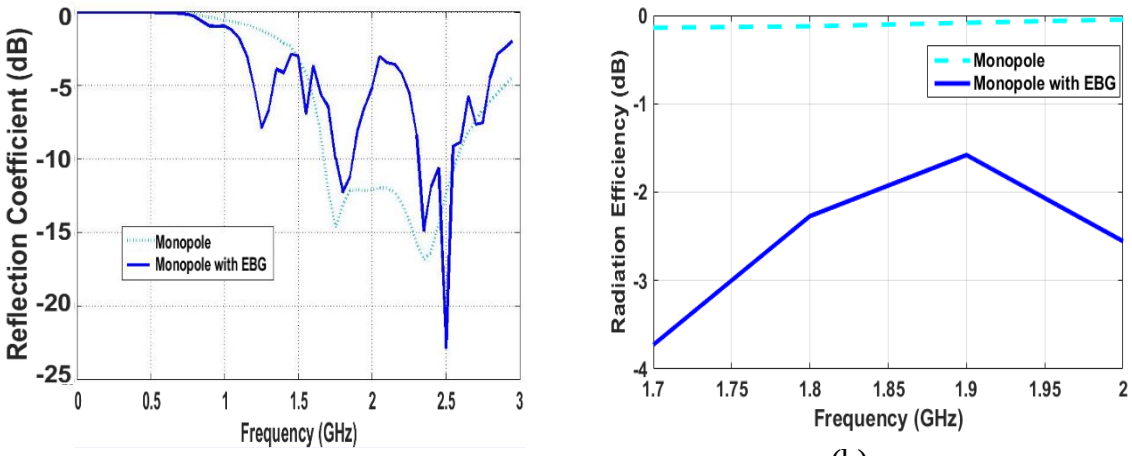

(a) (b)

Figure 7-20 : Monopole antenna performance in free space. (a) Reflection coefficient, (b) radiation efficiency.

The radiation efficiency by using the EBG in the free space is reduced by around 2 dB over the frequency band GSM 1900 (1.86-1.92 GHz) due to the losses inside the EBG.

As shown in [54], the EBG can be used to design high directivity resonator antennas. Figure 7-21 shows the directivity of the monopole antenna with the EBG (b), and without the EBG (a), at 1.9 GHz, we recognize a clear improvement of directivity of the monopole antenna into the upper hemisphere and a weakening into the back hemisphere where the user's head would be placed in actual operation.

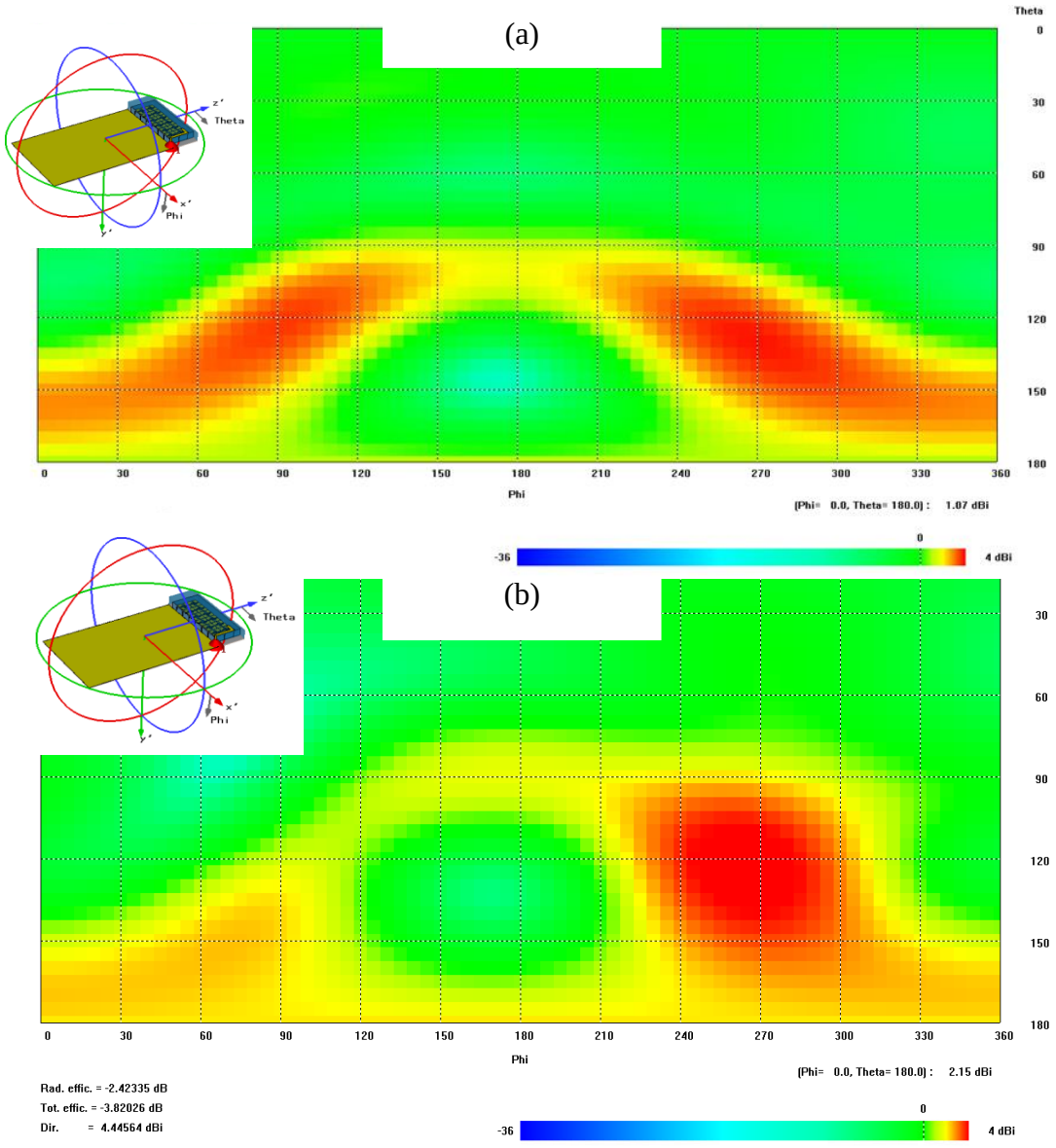

Figure 7-21 : Simulated directivity of the monopole antenna at 1.9 GHz in free space. (a) Without EBG, (b) with EBG as RF shield.

The radiation efficiency comparison shows about 1.8 dB to 2 dB losses by using the EBG. The reflection phase of the EBG structure is in the range of ±90°, which produces constructive superposition of incident and reflected signals. At Phi from 0° to 180 ° is the direction of the human head and as is shown in Figure 7-21,the electromagnetic wave is damped (the radiation pattern is reduced) at around Phi =90°, and increased around Phi=270°,which is away from the head.

For the measurement, the proposed monopole antenna is fabricated on a PCB with dielectric FR4 substrate. A 50-Ohm coaxial cable feeds the antenna, Figure 7-22. Ferrite core suppressor beads of 9.8 mm length are stacked on the cable to reduce the

EM coupling between the PCB with the coaxial cable via current flow on the outer conductor.

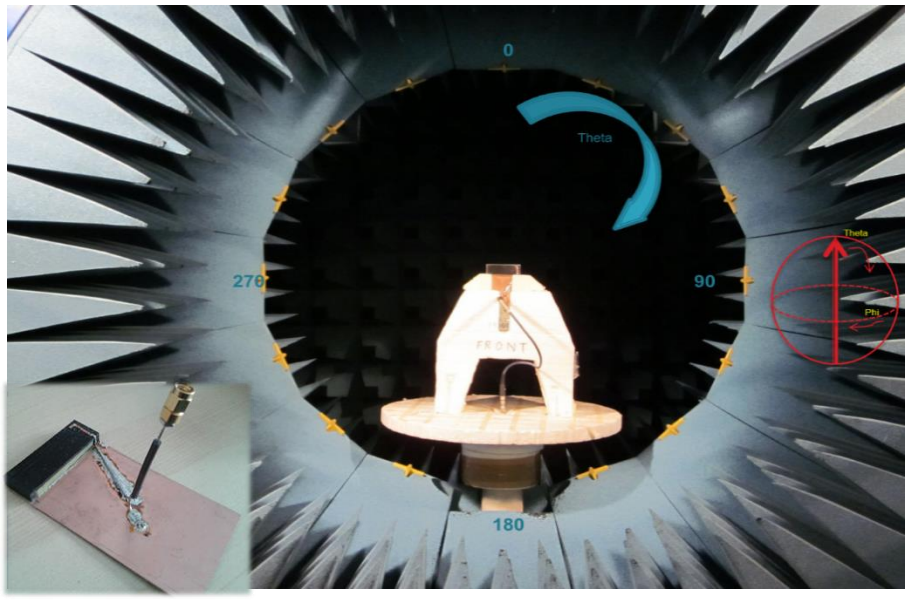

Figure 7-22: The proposed antenna structure in free space and passive antenna measurement tool with 15 Probes, (between two probes: 22.5°and rotation of the arch 11.25°), arranged at internal diameter of 0.9m.

Figure 7-23 shows the reflection coefficient of the proposed monopole antenna with EBG structure (2×6 unit cells), which is measured by the VNA. The frequency bandwidth at -6 dB of the monopole with the EBG covers the GSM1900 upload frequency band (1.86-1.92 GHz). Excellent matching of the reflection coefficient between the measurement and the FDTD simulation is seen.

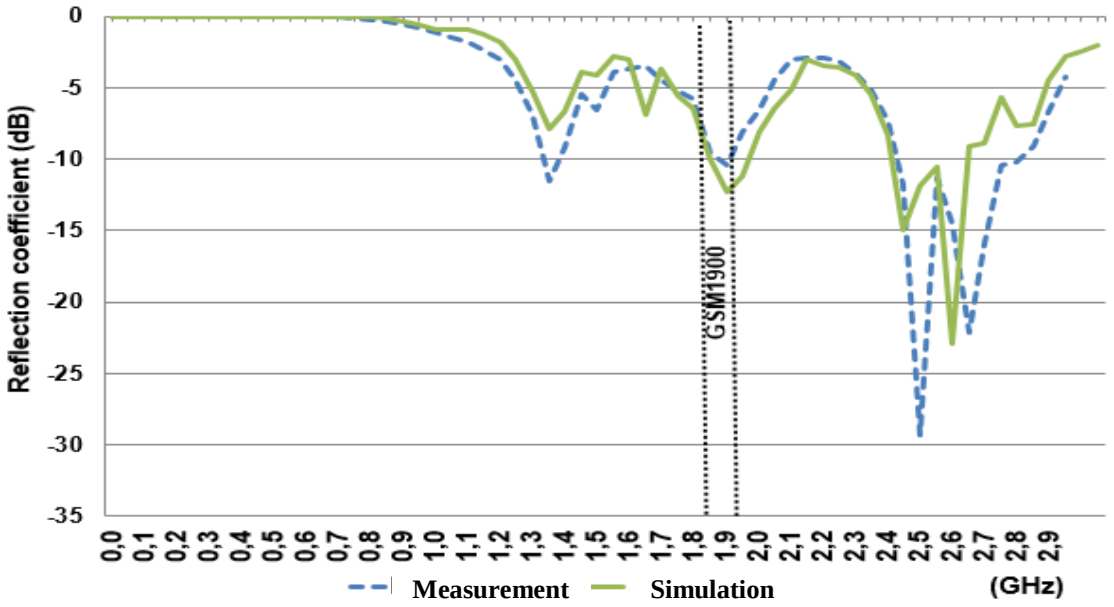

Figure 7-23 : Reflection coefficient of the proposed monopole antenna with EBG in free space.

The high impedance of the EBG surface reduces the diffraction effects since it is capable of suppressing the currents that are generated by the antenna and coupled to the backside of the ground plane of the PCB, as is shown in the radiation pattern measurement Figure 7-24 .Thus, the unwanted radiation of EM wave toward the head direction is reduced by 15 dB.

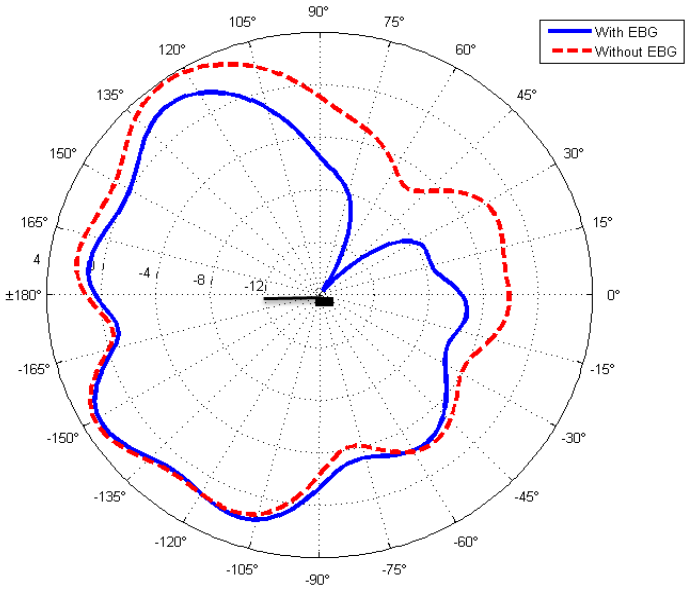

Figure 7-24: Radiation pattern of the proposed monopole antenna in free space.

Complementary results of measurements in free space using the setup of Figure 7-22 are shown in Figure 7-25. We see that, the radiation efficiency of the antenna has dropped after using the EBG by about 0.2dB at GSM 1900 and about 2dB in the rest of high-band 1.695-2.170 GHz, matching the simulation results of Figure 7-20.

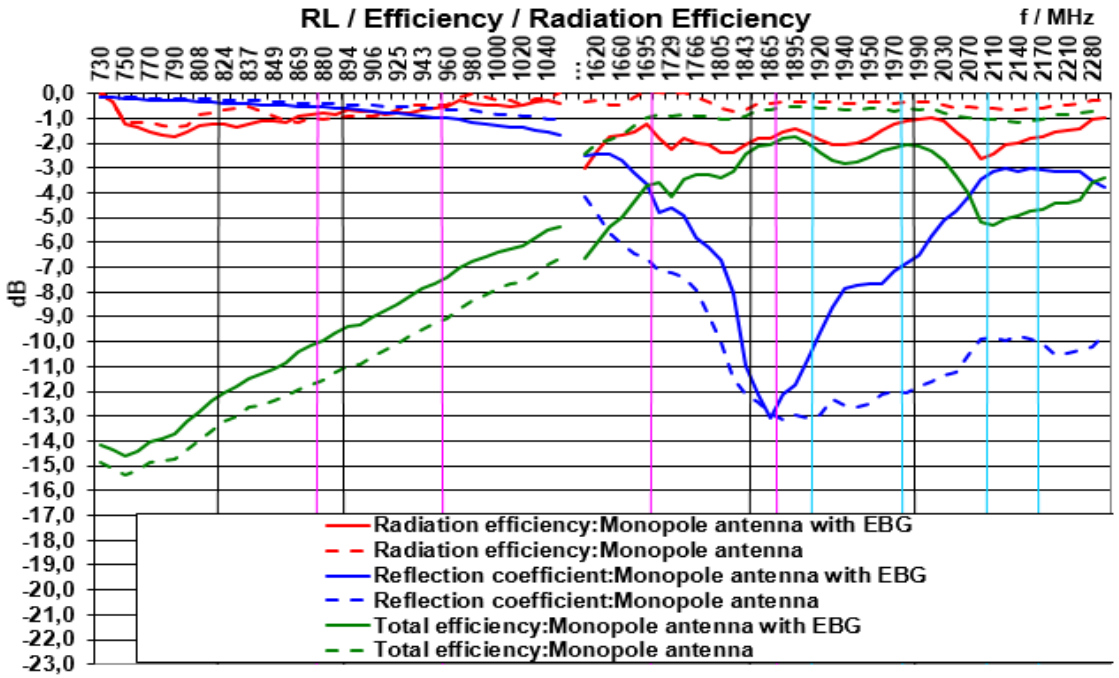

Figure 7-25 : Measurement results of monopole antenna with and without EBG.

7.4.2. Antenna beside the head:

The antenna performance with the phantom head is investigated to disclose the impact of the EBG on the antenna radiation efficiency and SAR value. In addition to the magnitude of SAR, it was seen interesting to study the location of the hotspots (Peak SAR) after applying the EBG structure. As seen in chapter 5, at the higher frequency around 1900 MHz, the main contributor should be expected to be the antenna.

Figure 7-26 shows the front view of the proposed structure placed above the phantom by 5 mm, with the space filled by low density rigid foam spacer for highly repeatable positioning of devices on the iSAR Flat. The spacer is precision-milled with a low dielectric loss tan δ =0.0008 and low permittivity $\varepsilon_r = 1.07$ [55]. The measurements in Figure 7-26 show SAR distributions at 4 mm below the surface of the phantom with and without EBG structure.

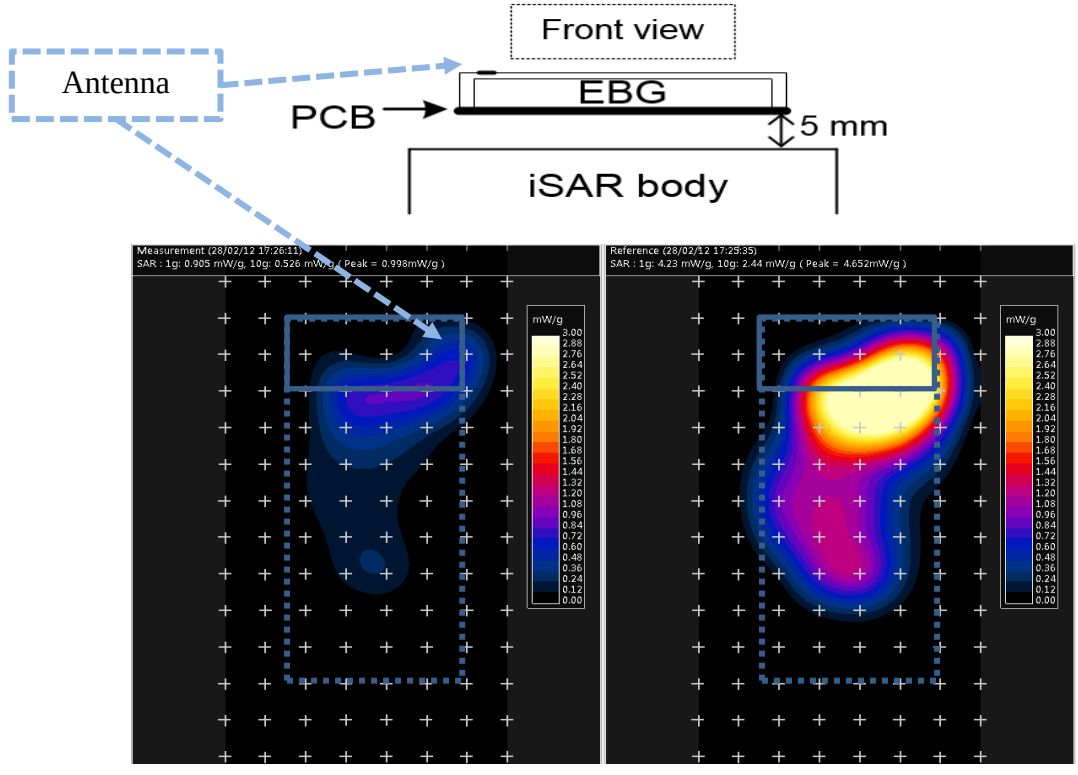

(a) (b)

Figure 7-26 : Measurement of SAR distributions of monopole antenna with EBG peak $\mathbf{SAR_{10g}}$=0.52 mW/g (a) and w/o EBG peak $\mathbf{SAR_{10g}}$=2.44 mW/g (b), P_{inc}=23dBm feed power at 1.88 GHz.

It seems that the SAR distributions have no significant change in the shape with integrated EBG ($15\times45mm^2$) compared to the case without EBG.

Most interestingly, it is found that peak SAR_{10g} can be reduced by 78% in case the EBG is used in the measurement. To complete the tests, the antenna efficiency and radiation pattern need to be investigated.

Figure 7-27 shows the measurement setup, consisting of the monopole antenna placed on the bottom side of the PCB and configured in the cheek position at the left side of the phantom's head. The PCB touches the earpiece of the phantom head on the top, and the phantom head is filled with fluid providing tissue equivalent electrical properties of human body. The tilted angle between the center line of the PCB and the vertical line of the phantom is 63°.

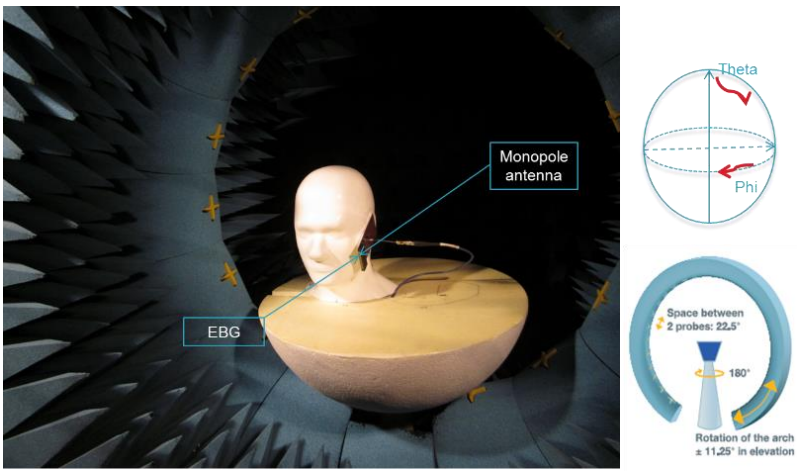

Figure 7-27: Measurement of the antenna pattern with head using the SATIMO tool.

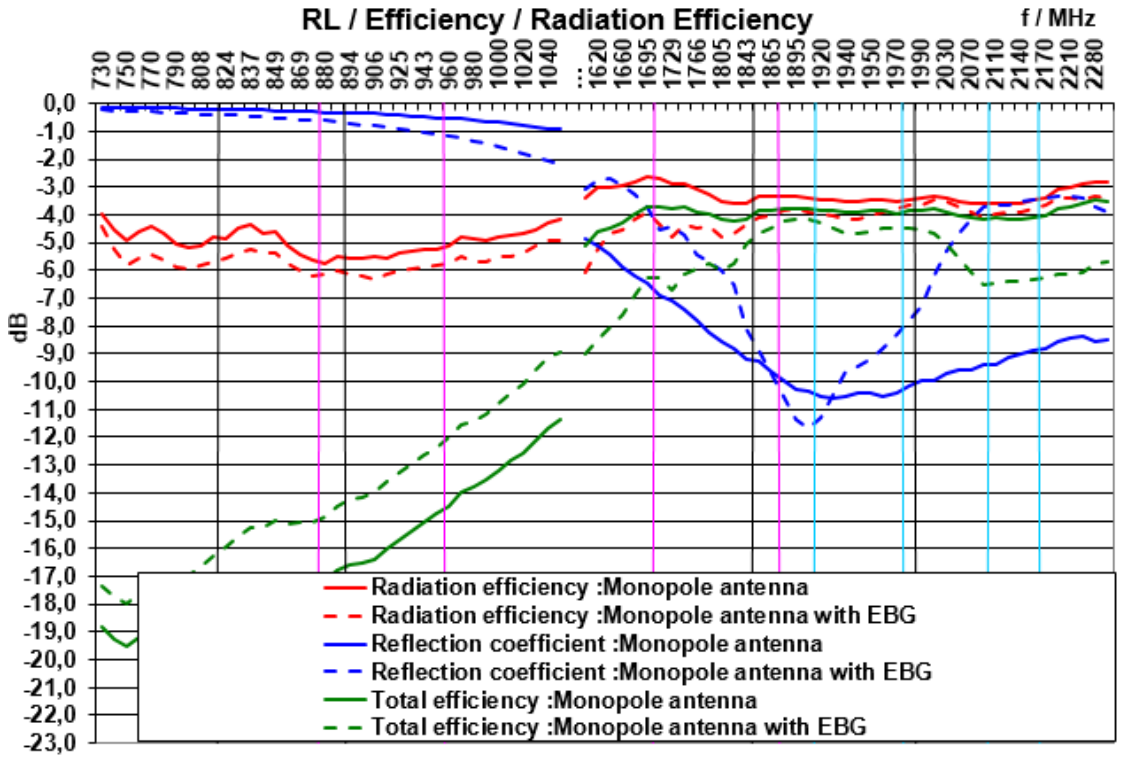

Figure 7-28: Monopole antenna parameters measured with/ without EBG in cheek position beside the head.

Figure 7-28 shows the antenna performance at the frequency band of interest (GSM 1900): From 1886 MHz to 1920 MHz the radiation efficiency drops from -3.3 dB without EBG to -3.8 dB (10%) when the antenna is backed by EBG; furthermore, the reflection coefficient is still under -6 dB such that there is no need to re-tune the antenna and the total efficiency is slightly degraded by the EBG.

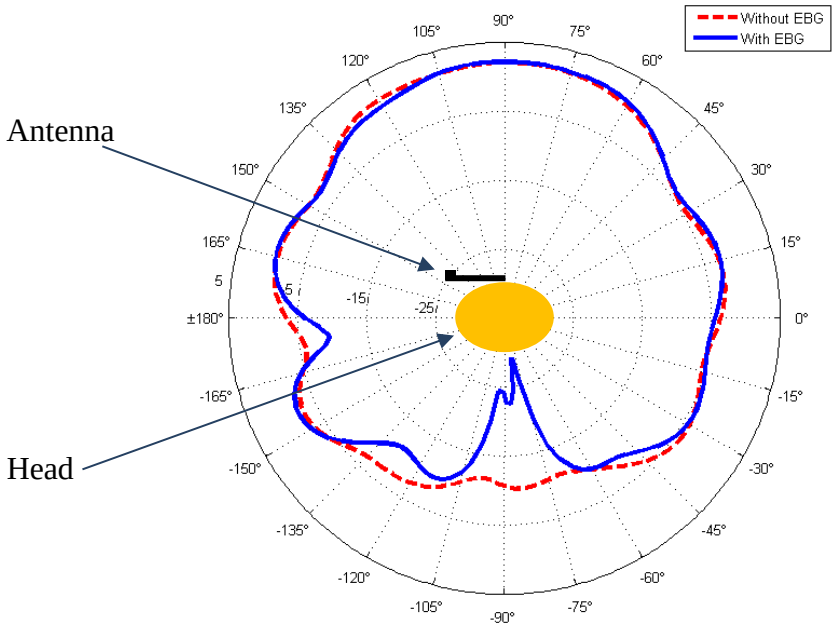

Figure 7-29 : Radiation pattern of the monopole antenna beside a phantom head in the horizontal plane, with and without EBG at 1.88 GHz.

The radiation pattern presented in Figure 7-29, is a conventional Omni-directional pattern of the normal monopole in the horizontal plane attenuated by dissipation loss in the head. Using the EBG, the induced fields inside the head are decreased because the radiation power is reduced in the direction of the human head, and therefore, the dissipation inside head is reduced. This reduction of dissipation loss is compensated by the dissipation inside the EBG: We see a slight drop in the antenna efficiency after implementing the EBG, as shown in Figure 7-28 and Figure 7-29. The EBG reduces the SAR inside the phantom head with very small effect at the radiation efficiency of the mobile's antenna in this position beside the head.

As is shown in chapter 2, the DASY 4 tool is used to measure the SAR_{10g} in the phantom head. Figure 7-30 shows the calibrated measurement system which consists of a 3D probe to measure the E-fields inside the phantom at 4mm from surface with mechanical surface detection. The scan area is $81\times141mm^2$ inside the head phantom which is filled with liquid (ε_r=38.8, σ=1.39 S/m) and has a shell (ε_r=4.5, tanδ = 0.05). The measurements were taken over a grid of d_X=10mm, and d_Y=10mm.

The mobile phone structure touches the phantom head, with bottom antenna position. Incident power P_{inc}= 24dBm, which is the standard power level of the RF transmitter at the frequency band GSM 1900.

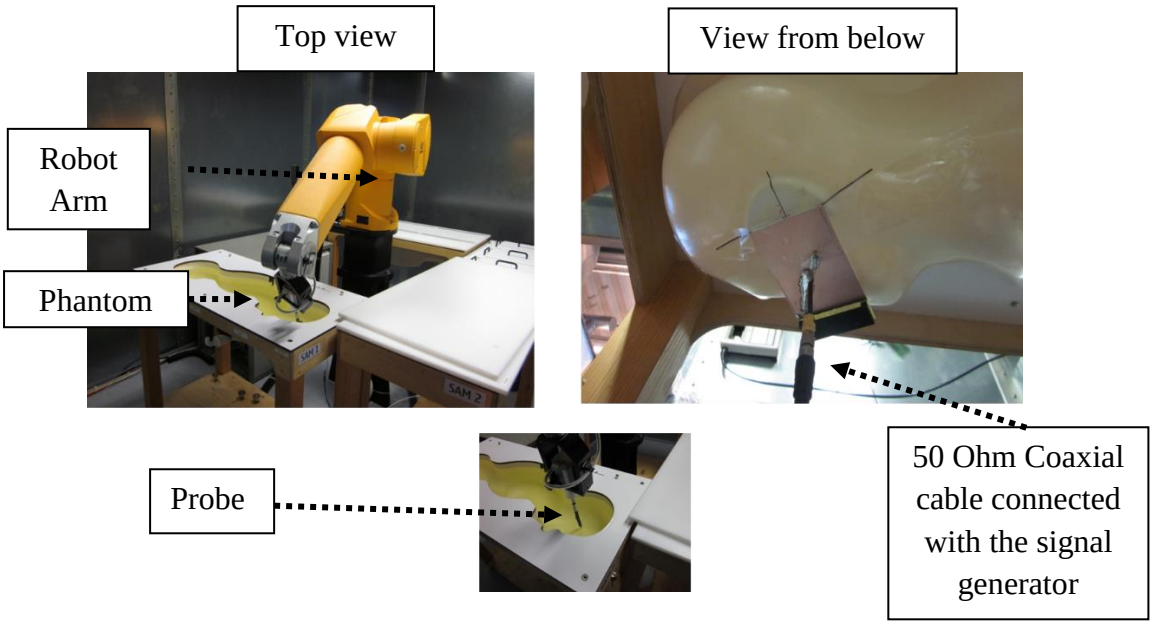

Figure 7-30: SAR antenna model measurement for head left section. Medium parameters at 1800 to 2170 MHz: σ=1.39 S/m; ε=38.8; ρ=1000 kg/$\boldsymbol{m^3}$. P_{inc}= 24 dBm

.

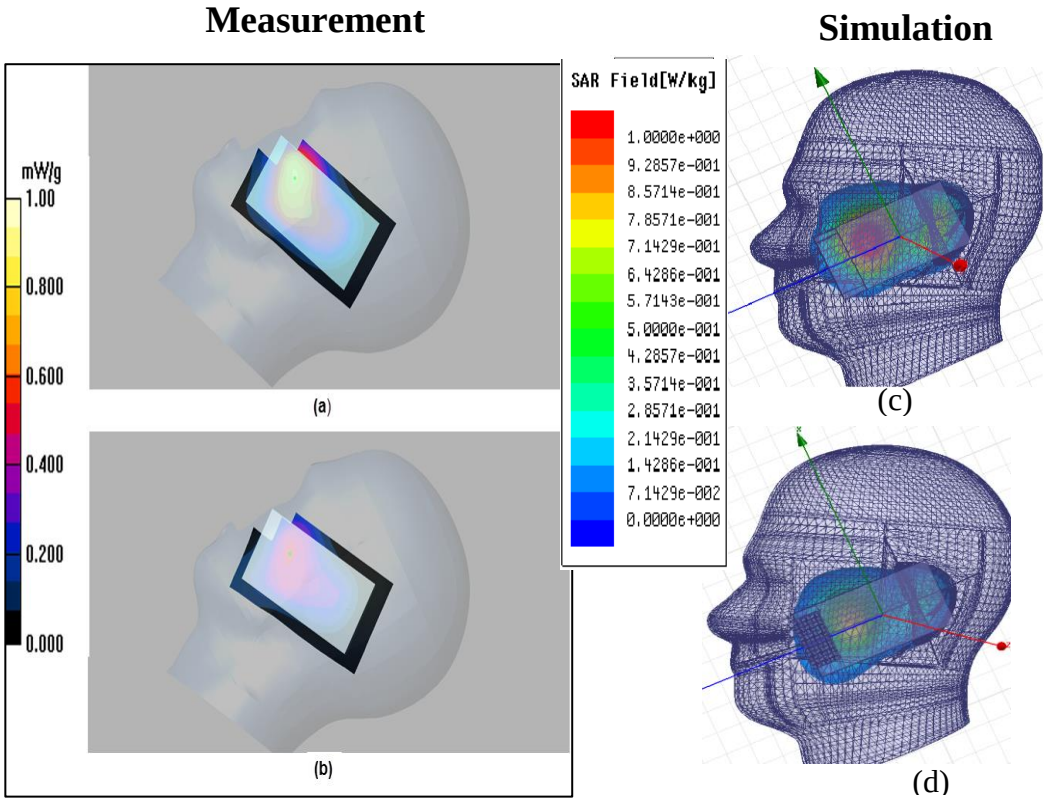

Figure 7-31: SAR_{10g} distribution map at 1.88 GHz; (a), (c) conventional monopole antenna and (b),(d) monopole antenna with EBG. Measurements (a),(b) and simulation (c),(d).

Figure 7-31 shows the SAR distributions inside the head from measurement (a),(b) and from simulation by HFSS (c),(d) . The peak SAR location and amplitude are exactly the same in simulation and measurement. The Table 7-1 shows the measured SAR values of the monopole antenna for 1g and 10 g: With the proposed EBG structure SAR is reduced by ~39 % at the center frequency of the GSM 1900.

SAR(mW/g) 1g/10g(Avg.)	**1852.4 MHz**	**1880 MHz**	**1907.6 MHz**
Monopole	0.748 / 0.47	0.753 / 0.465	0.867 / 0.532
Monopole with EBG	0.499 / 0.311	0.453 / 0.283	0.539 / 0.333
$\frac{\mathbf{SAR} - \mathbf{SAR(EBG)}}{\mathbf{SAR}} \times \mathbf{100}$	33.3 % / 33.8 %	39.8 % / 39.1 %	37.8 % / 37.4 %
	Low channel	**Middle channel**	**High channel**

Table 7-1: Comparison of measured SAR values with/without EBG at GSM 1900.

The results show that the SAR value inside the head is reduced by 39% at the cost of reduced radiation efficiency by 10% at the GSM1900 Band (Uplink frequency 1850-1910 MHz).However practically it would be possible to increase the generated power to recover the 10% loss in the antenna efficiency and still reduce the SAR level.

As conclusion, the EBG with high impedance surface properties in a specified frequency band is capable of suppressing surface currents on the PCB and thus reducing the radiation toward the head. Therefore it is found a good solution to reduce SAR in the user's head.

7.5. Impact of EBG on antenna performance at GSM 900:

At the frequency band GSM1900, the proposed EBG successfully suppresses surface currents and reflects incident electromagnetic waves without phase reversal, but for out-of-band frequencies the EBG behaves similar to conductive sheet with phase reversal, and that causes a reduction in total antenna efficiency as seen in section 6.3.2. Thus, if a low-band antenna or Bluetooth antenna is placed near a EBG it will also generate strong surface currents that propagate along the conductive EBG surface. Mobile phones incorporate multi antennas operating at different frequencies most importantly at GSM 900 frequencies. Therefore antenna efficiency is investigated for the case of a loop antenna for GSM 900 when it is backed by the proposed EBG.

The effect of the stacked EBG which is designed to work at around 1900 MHz on antenna performance at 900 MHz is investigated in this section.

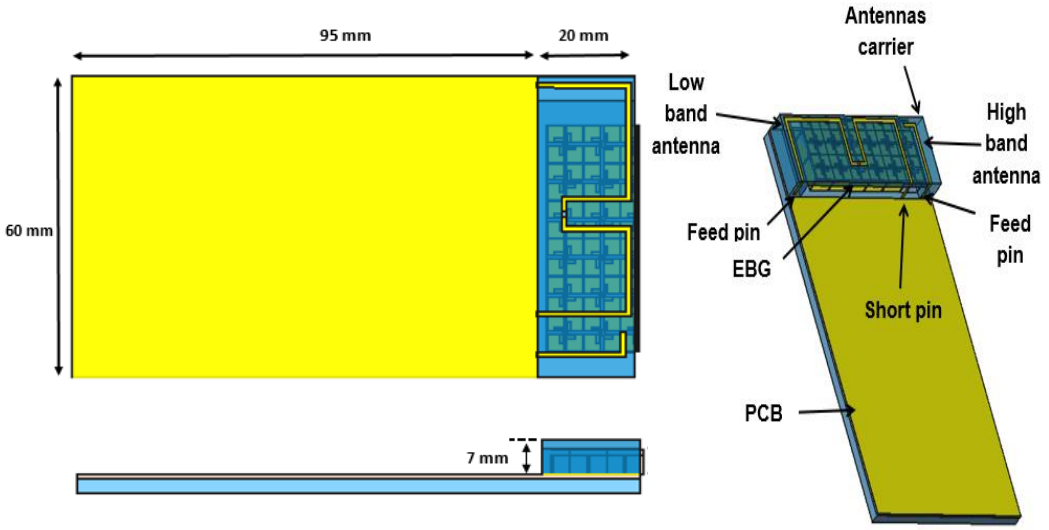

Figure 7-32 : Geometry of the two-antenna model. Monopole antenna for the 1900 MHz band and loop antenna for 900 MHz on a PCB with FR4 $\varepsilon_r = 4.9$, tanδ=0.025 and with a stacked EBG integrated. Antenna carrier (ε_r=3, tanδ=0.02).

Figure 7-32 shows the geometry of the proposed antenna model with the EBG structure below the antennas, a monopole antenna for high-band GSM1900 and a loop antenna for GSM 900.

The loop antenna with one feed pin and one short pin is located at 7mm above the PCB and tuned to have the first resonance at frequency 900 MHz by using one SMD (Surface Mounted Device) inductor in series, this inductor is used also to re-tune the loop antenna after inserting the EBG.

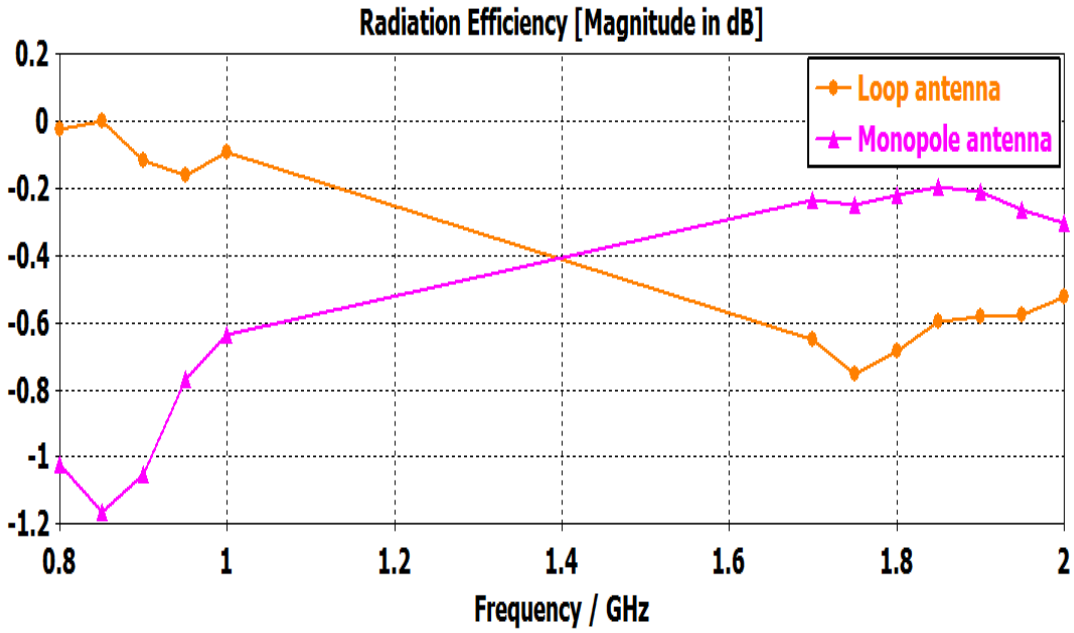

Figure 7-33: The measured radiation efficiency of the loop antenna and the monopole antenna for the low-and high-bands respectively in free space without EBG.

Figure 7-33 shows that the radiation efficiency for the loop antenna without EBG in free space is about -0.18 dB at the GSM 900 frequency band.

From the measurements, Figure 7-34, the reflection coefficient is seen to be less than -6dB at the GSM 900 frequency band and the radiation efficiency of the loop antenna with EBG has dropped about 2 dB in free space by integrating the EBG, but still is above the antenna efficiency limit for the standard mobile phone antenna design, which is -3 dB for the GSM 900 transmit band.

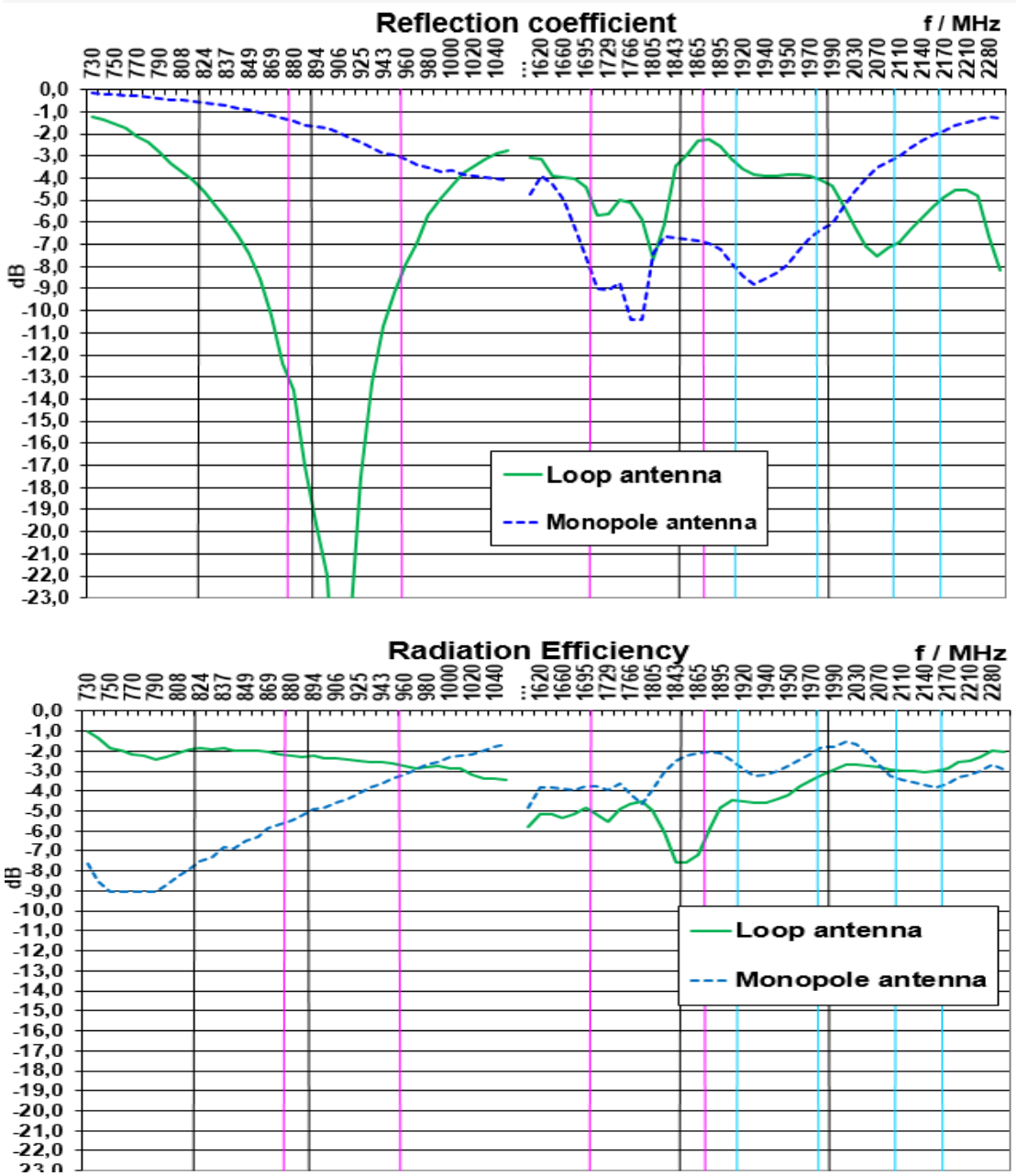

Figure 7-34: The reflection coefficient and the radiation efficiency of the loop antenna and the monopole antenna for the low-and high-bands respectively and with integrated EBG measured in free space.

Loop antenna beside the head:

This simulation assumes that the mobile phone structure touches the phantom head, with bottom antenna position and with accepted power P_{acc}= 24dBm at the frequency band GSM 900. Figure 7-35 shows the radiation efficiency of the loop antenna beside

the head dropped by 0.5 dB with the integrated EBG, obviously due to dissipated power inside and at the back of the EBG.

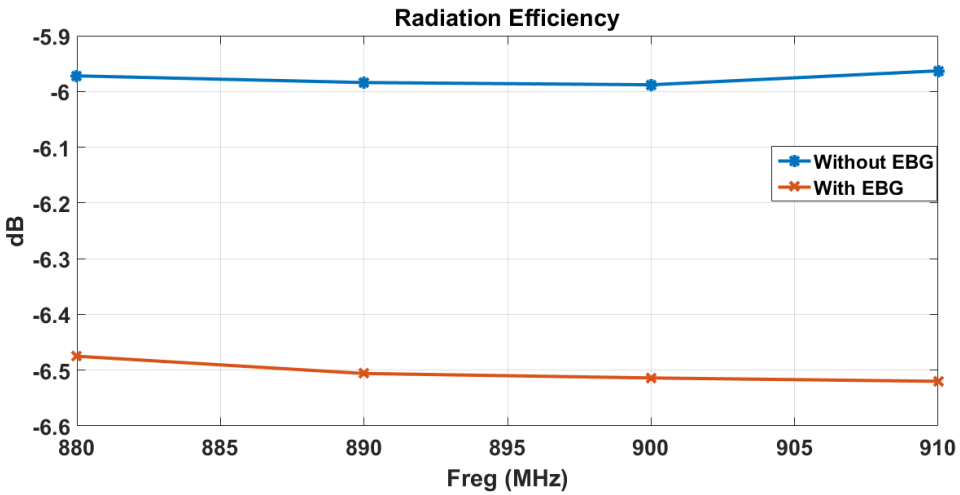

Figure 7-35: The radiation efficiency of the loop antenna for GSM 900 beside the head with and without integrated EBG.

Figure 7-36 shows the SAR distributions inside the head. The peak SAR is located close to the middle of the PCB and the SAR_{10g} distribution inside the head is practically equal for the two cases (with and without integrated EBG).

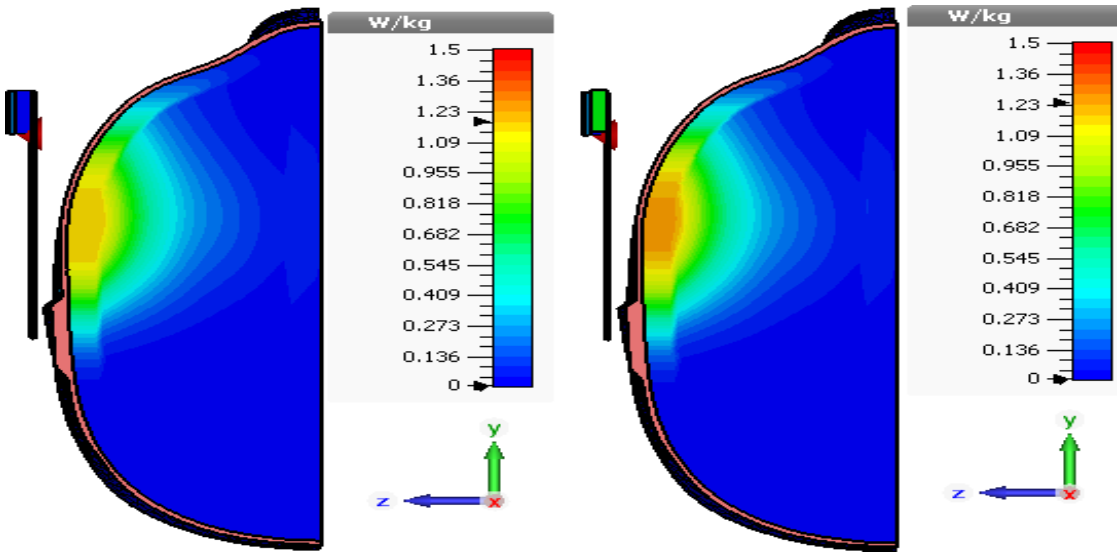

(a) (b)

Figure 7-36: SAR_{10g} distribution map at 900 MHz; (a) loop antenna without EBG and (b) loop antenna with integrated EBG. Peak $\mathbf{SAR_{10g}}$=1.23 mW/g with EBG, and w/o EBG peak $\mathbf{SAR_{10g}}$=1.18 mW/g. P_{acc}= 24 dBm.

7.6. Conclusion

The stacked EBG structure is found to be the best solution to reduce the specific absorption rate SAR value of the standard monopole antenna for GSM 1900.

The monopole backed by the proposed EBG structure demonstrates a significant SAR reduction by 78 % and radiation efficiency losses by only 10% compared to the case of the monopole antenna without EBG beside the head.

Deteriorating effects of the EBG on other antennas on the PCB can be assumed to be acceptably low.

In particular, in the most critical case of the GSM 900 antenna, the loop antenna efficiency of -2 dB still satisfies commercial mobile antenna transmit requirements and no considerable degradation in SAR performance is seen.

Chapter 8

8. Conclusions and Future Work

As we already see from the analysis of absorption mechanisms for mobile phones and behaviour of mobile terminal antennas near dielectric material, the currents of the chassis at the low cellular frequencies (GSM 900) and of the antenna element at the high cellular frequencies (GSM 1900) cause high peak specific absorption rate (SAR) values, which especially at the GSM 1900 band is quite often problematic.

Fundamental descriptions of the interaction between the user and the antenna are found to be the antenna efficiency and most importantly SAR; which are investigated using EM simulation and measurement technologies. It is found that the interaction between the human head and the antenna is located in near field region. Therefore the near field distributions which are excited from the assumed small antennas and which propagate inside the phantom and lead to absorption are investigated. It is found that at 1900 MHz the PCB resembles a full wavelength resonator such that the electric field has a strong area around the center of the PCB in addition to the open ends of the resonator, while the magnetic field peaks around areas in which the surface current on the resonator is high.

The EM interaction between the antenna and the human head has been discussed in this thesis with different SAR reduction methods, such as parasitic elements, wavetraps, directive control antenna, slotted ground plane, antenna type optimization, and RF shields (Ferrite, PEC, and PMC). These methods either cause reduction in the antenna efficiency in free space after reduction of SAR or they are hard to produce and integrated below the antenna and inside the mobile phone. Due to that, a stacked EBG structure has been investigated in this thesis as EM shield placed underneath the RF antenna tuned to reflect the field with zero phase reversal. At the mobile operating frequency band of GSM 1900 upload band (1860-1920 MHz) the propagation of surface waves is suppressed, and the EM fields against the human body are dispersed. The stop band gap property of the proposed EBG is shown to be in excellent agreement between the simulation and the measured results.

The stacked EBG structure is found to be the best solution to reduce SAR value of the standard monopole antenna for GSM 1900 with a slight drop of antenna radiation efficiency in free space and beside the head.

A commonly used antenna for the low frequency band GSM 900 , the loop antenna has been designed and fabricated, and the impact of the EBG on the loop antenna performance and SAR value at GSM 900 was investigated. It is found from measurements that the loop antenna efficiency with integrated EBG still satisfies commercial mobile antenna transmit requirements and no significant degradation in SAR performance is seen.

For the future, the antenna performance and SAR value should be investigated for new antenna designs such as the dual-loop (multi-band antenna) with integrated EBG structure .

References

[1] *3GPP TS 05.05 version 8.20.0 Release 1999.*

[2] D. Manteuffel, A. Bahr, D. Heberling and I. Wolff, "Design considerations for integrated mobile phone antennas," in *Antennas and Propagation, 2001. Eleventh International Conference*, Manchester, 2001.

[3] Satimo, "Satimo products," SATIMO, [Online]. Available: http://www.satimo.com/content/products/starlab. [Accessed 16 January 2015].

[4] Satimo, "Electromagnetic Field Measurements," SG64, [Online]. Available: http://www.satimo.com/content/products/sg-64. [Accessed 15 January 2015].

[5] "ICNIRP GUIDELINES FOR LIMITING EXPOSURE TO TIME-VARYING ELECTRIC, MAGNETIC AND ELECTROMAGNETIC FIELDS (UP TO 300 GHZ)," *HEALTH PHYSICS*, vol. 74, no. 4, pp. 494-522, April 1998.

[6] J. Jokela, D. Leszczynski, W. Paile, S. Salomaa, L. Puranen and P. Hyysalo, "Radiation safety of handheld mobile phones and base stations," Radiation and Nuclear Safety Authority, Helsinki, 1999.

[7] C. H. Durney, H. Massoudi and M. F. Iskander, Radiofrequency radiation dosimetry handbook, Brooks Air Force Base, May 2002.

[8] D. Conover, E. Moss, R. Edwards, C. Clinton, B. Grajewski, D. Werren and J. Smith, "Foot currents and ankle SARs induced by dielectric heaters," *Bioelectromagnetics*, vol. 13, no. 2, pp. 103-110, 1998.

[9] D. Hill, "The effect of frequency and grounding on whole-body absorption of humans in E-polarized radiofrequency fields," *Bioelectromagnetics,* vol. 5, pp. 131-146, 1984.

[10] "SPEAG," DASY5, [Online]. Available: http://www.speag.com/products/dasy/dasy-systems/. [Accessed 10 January 2015].

[11] I. S. 1528-2003, "IEEE Recommended Practice for Determining the Peak Spatial-Average Specific Absorption Rate (SAR) in the Human Head from Wireless Communications Devices: Measurement Techniques," pp. 1-120, 2003.

[12] A. Drossos, V. Santomaa and N. Kuster, "The dependence of electromagnetic energy absorption upon human head tissue composition in the frequency range of 300-3000 MHz," *Microwave Theory and Techniques, IEEE Transactions on,* vol. 48, no. 11, pp. 1988-1995, 2000.

[13] A. Faraone, D. O. McCoy, C. -K. Chou and Q. Balzano, "Characterization of miniaturized E-field probes for SAR measurements," in *Electromagnetic Compatibility, 2000. IEEE International Symposium on*, Washington, DC, IEEE, 2000, pp. 749-754 vol.2.

[14] "iSAR Flat," Speag AG, [Online]. Available: http://www.speag.com/products/isar2/isar2-systems/isar-flat/. [Accessed 15 January 2015].

[15] M. Y. Kanda, M. G. Douglas, E. D. Mendivil, M. Ballen, A. V. Gessner and K. Chung, "Faster determination of mass-averaged SAR from 2-D area scans," *Microwave Theory and Techniques, IEEE Transactions on*, vol. 52, no. 8, pp. 2013-2020, 2004.

[16] C. Balanis, Antenna Theory,Analysis and Design, New York: John Wiley and Sons, 2005.

[17] P. Vainikainen, J. Ollikainen, O. Kivekas and I. Kelander, "Resonator-based analysis of the combination of mobile handset antenna and chassis," *Antennas and Propagation, IEEE Transactions on,* vol. 50, no. 10, pp. 1433-1444, 2002.

[18] "WaveForm Global Pty Ltd - EME Solutions," [Online]. Available: http://waveformglobal.com.au/. [Accessed 10 01 2015].

[19] S. Gabriel, R. W. Lau and C. Gabriel, "The dielectric properties of biological tissues: III. Parametric models for the dielectric spectrum of tissues," *Physics in Medicine and Biology,* vol. 41, pp. 2271-2293, 1996.

[20] O. Kivekäs, T. Lehtiniemi and P. Vainikainen, "On the general energy absorption mechanism in the human tissue," *MICROWAVE AND OPTICAL TECHNOLOGY LETTERS,* vol. 43, no. 3, pp. 195-201, 2004.

[21] N. Kuster and Q. Balzano, "Energy absorption mechanism by biological bodies in the near field of dipole antennas above 300 MHz," *Vehicular Technology, IEEE Transactions on,* vol. 41, no. 1, pp. 17-23, 1992.

[22] H. -R. Chuang, "Numerical computation of fat layer effects on microwave near-field radiation to the abdomen of a full-scale human body model," *Microwave*

Theory and Techniques, IEEE Transactions on, vol. 45, no. 1, pp. 118-125, 1997.

[23] J. Holopainen, R. Valkonen, O. Kivekas, J. Ilvonen, L. Martinez, P. Vainikainen, J. Kelly and P. Hall, "Equivalent circuit model-based approach on the user body effect of a mobile terminal antenna," in *Antennas and Propagation Conference (LAPC)*, Loughborough, 2010.

[24] K. Yee, "Numerical solution of initial boundary value problems involving maxwell's equations in isotropic media," *Antennas and Propagation, IEEE Transactions on*, vol. 14, no. 5, pp. 302-307, 1966.

[25] F. Demming-Janssen and W. Koch, "3D Field simulation of sparse arrays using various solver techniques within CST MICROWAVE STUDIO," in *Radar Conference, 2006. EuRAD 2006. 3rd European*.

[26] IEEE, "IEEE Recommended Practice for Measurements and Computations of Radio Frequency Electromagnetic Fields With Respect to Human Exposure to Such Fields,100 kHz-300 GHz," *IEEE Std C95.3*, pp. i-126, 2002.

[27] C. T. Famdie, Schroeder, L. Werner and K. Solbach, "Numerical analysis of characteristic modes on the chassis of mobile phones," *Antennas and Propagation*, no. 11, pp. 1-6, 2006.

[28] J. Poutanen, J. Villanen, C. Icheln and P. Vainikainen, "Behaviour of Mobile Terminal Antennas near Human Tissue at a Wide Frequency Range," *Antenna Technology: Small Antennas and Novel Metamaterials*, vol. 4, no. 3, pp. 219-222, 2008.

[29] D. Manteuffel, A. Bahr, P. Waldow and I. Wolff, "Numerical analysis of absorption mechanisms for mobile phones with integrated multiband antennas," *Antennas and Propagation Society International Symposium,IEEE*, vol. 3, no. 7, pp. 82-85, 2001.

[30] M. Sager, M. Forcucci and T. Kristensen, "A novel technique to increase the realized efficiency of a mobile phone antenna placed beside a head-phantom," *Antennas and Propagation Society International Symposium, 2003. IEEE*, vol. 2, no. 6, pp. 1013-1016 , 2003.

[31] J. Holopainen, J. Ilvonen, O. Kivekas, R. Valkonen, C. Icheln and P. Vainikainen, "Near-Field Control of Handset Antennas Based on Inverted-Top Wavetraps: Focus on Hearing-Aid Compatibility," *Antennas and Wireless Propagation Letters,IEEE*, vol. 8, pp. 592,595, 2009.

[32] H. Haruki, Y. Koyanagi and K. Egawa, “Radiation Characteristics of an Antenna System with a Dividing Feed Circuit for a Handy Phone in the Talk Position,” *IEICE Technical Report,* p. 164, 2003.

[33] T. Nishikido, Y. Saito , M. Hasegawa, H. Haruki and Y. Koyanagi, “Multi-antenna system for a handy phone to reduce influence by user's hand,” in *Personal, Indoor and Mobile Radio Communications*, 14th IEEE Proceedings on, 2003, pp. 1898-1901.

[34] K. Wong, J. Kuo and T. Chiou, “Compact microstrip antennas with slots loaded in the ground plane,” in *Antennas and Propagation*, 2001.

[35] C. Picher, J. Anguera, A. Andujar, C. Puente and S. Kahng, “Analysis of the Human Head Interaction in Handset Antennas with Slotted Ground Planes,” *Antennas and Propagation Magazine, IEEE,* vol. 54, no. 4, pp. 36-56, 2012.

[36] A. Andujar, J. Anguera, C. Picher and C. Puente, “Ground plane booster antenna technology: Human head interaction: Functional and biological analysis,” in *Antennas and Propagation (EUCAP), 2012 6th European Conference on*, 2012.

[37] A. Ikram, C. Beckman and S. Irmscher, “Design and development of a multiband loop antenna for cellular mobile handsets,” in *Antenna Technology (iWAT)*, Hong Kong, IEEE, 2011, pp. 251-254.

[38] P. Hui, “Near fields of phased antennas for mobile phones,” in *Microwave Conference,APMC 2009.* , Singapore, IEEE, 2009, pp. 2718-2721.

[39] A. Arkko, J. Troelsen and R. So, “Apparatus for wireless communication comprising a loop like antenna”. US Patent 2012/0194404 A1, Aug 2012.

[40] K. Chan, K. Chow, L. Fung and S. Leung, “Effects of using conductive materials for SAR reduction in mobile phones,” *Microwave and Optical Technology Letters,* vol. 44, no. 2, pp. 140-144, 2005.

[41] A. Hirata, T. Adachi and T. Shiozawa, “Folded-loop antenna with a reflector for mobile handsets at 2.0 GHz,” *Microwave and Optical Technology Letters,* vol. 40, no. 4, pp. 272-275, 2004.

[42] J. Minseok and L. Bomson, “SAR reduction for mobile phones based on analysis of EM absorbing material characteristics,” in *Antennas and Propagation Society International Symposium*, IEEE, 2003, pp. 1017-1020.

[43] M. Islam, M. Faruque and N. Misran, "Design analysis of ferrite sheet attachment for sar reduction in human head," *Progress In Electromagnetics Research,* vol. 98, pp. 191-205, 2009.

[44] L. Fung, S. Leung and K. Chan, "Experimental study of SAR reduction on commercial products and shielding materials in mobile phone applications," *Microwave and Optical Technology Letters,* vol. 36, no. 6, pp. 419-422, 2003.

[45] M. Kitra, P. Mcevoy, J. Vardaxoglou and J. James, "A theoretical and experimental study of dielectrically loaded antennas and their contribution towards low-SAR," *Antennas and Propagation Society International Symposium,* vol. 4, no. 6 pp. 3593-3596, 2004.

[46] L. Ragha and M. Bhatia, "Evaluation of SAR Reduction in Implanted Spherical Head Model Using RF Shield," *India Conference (INDICON),* pp. 1-4, 2009.

[47] M. Kitra, C. Panagamuwa, P. McEvoy, J. Vardaxoglou and J. James, "Low SAR Ferrite Handset Antenna Design," *Antennas and Propagation, IEEE Transactions on,* vol. 55, no. 4, pp. 1155-1164, 2007.

[48] "NEC," Flex suppressor, [Online]. Available: http://www.nec-tokin.com/english/guide/flexsuppressor/pdf/flex_rfid_rm4a_e.pdf. [Accessed 20 March 2015].

[49] N. Hanafi, M. Islam, N. Misran and M. Faruque, "Numerical analysis of aluminium sheet for SAR reduction," in *Space Science and Communication (IconSpace),* IEEE International Conference on, 2011, pp. 281-285.

[50] L. Ragha and M. Bhatia, "Evaluation of SAR Reduction for Dipole Antenna Using RF Shield," in *Emerging Trends in Engineering and Technology (ICETET),* 2nd International Conference on, 2009, pp. 1075-1079.

[51] D. SIEVENPIPER, High-Impedance Electromagnetic Surfaces, Los Angeles,CA: University of California (UCLA) , 1999.

[52] F. Yang and Y. Rahmat Samii, Electromagnetic Band Gap Structures in Antenna Engineering, Cambridge: Cambridge University Press, 2008.

[53] S. i. Kwak, D.-U. Sim and J. H. Kwon, "SAR reduction on a mobile phone antenna using the EBG structures," in *Microwave Conference,EuMC 2008. 38th European*, Amsterdam, IEEE, 2008, pp. 1308-1311.

[54] A. Weily, L. Horvath, K. Esselle, B. Sanders and T. Bird, "A planar resonator antenna based on a woodpile EBG material," *Antennas and Propagation, IEEE Transactions on*, vol. 53, no. 1, pp. 216-223, 2005.

[55] Speag, "Spacers for iSAR Flat," Schmid & Partner Engineering AG, [Online]. Available: http://www.speag.com/products/isar2/isar2-accessories/isar2-spacers/. [Accessed 15 June 2015].

[56] B. A. Munk, Frequency Selective Surfaces: Theory and Design, John Wiley & Sons Inc., 2000.

[57] J. D. Joannopoulos, R. D. Meade and J. N. Winn, Photonic Crystals, Princeton University Press, 1995.

[58] E. Yablonovitch, "Inhibited spontaneous emission in solid-state physics and electronics," *Phys. Rev. Lett.*, vol. 58, pp. 2059-2063, 1987.